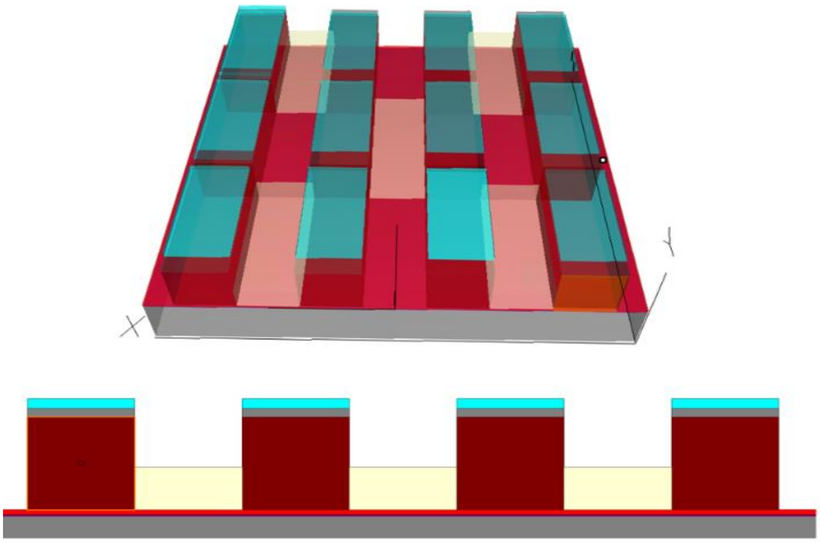

Design of a Programmable Photonic Integrated Circuit based on Carrier Depletion Phase Shifters.

ERNESTO LAZARO CHAVEZ VELÁZQUEZ
(Licenciado em Engenharia Electrónica e Telecomunicações)

Dissertação para obtenção do Grau de Mestre em Engenharia de Electrónica e
Telecomunicações, no Perfil de Telecomunicações

Orientadores:
Doutor Alessandro Fantoni
Doutor Paulo Lourenço

Júri:
Presidente: Doutora Paula Maria Garcia Louro
Vogais:
Doutor Alessandro Fantoni
Doutora Maria Manuela De Almeida Carvalho Vieira

Novembro de 2025

Design of a Programmable Photonic Integrated Circuit based on Carrier Depletion Phase Shifters.

ERNESTO LAZARO CHAVEZ VELÁZQUEZ
(Licenciado em Engenharia Electrónica e Telecomunicações)

Dissertação para obtenção do Grau de Mestre em Engenharia de Electrónica e Telecomunicações, no Perfil de Telecomunicações

Orientadores:
Doutor Alessandro Fantoni, Instituto Superior de Engenharia de Lisboa (ISEL), Instituto Politécnico de Lisboa (IPL), Portugal, Center of Technology and Systems (CTS), and Associated Lab of Intelligent Systems (LASI), Caparica, Portugal
Doutor Paulo Lourenço, Instituto Superior de Engenharia de Lisboa (ISEL), Instituto Politécnico de Lisboa (IPL), Portugal, Center of Technology and Systems (CTS), and Associated Lab of Intelligent Systems (LASI), Caparica, Portugal

Júri:
Presidente: Doutora Paula Maria Garcia Louro, Instituto Superior de Engenharia de Lisboa (ISEL), Instituto Politécnico de Lisboa (IPL), Universidade NOVA de Lisboa (UNINOVA), Center of Technology and Systems (CTS) and Associated Lab of Intelligent Systems (LASI), Caparica, Portugal
Vogais:
Doutor Alessandro Fantoni, Instituto Superior de Engenharia de Lisboa (ISEL), Instituto Politécnico de Lisboa (IPL), Portugal, Center of Technology and Systems (CTS), and Associated Lab of Intelligent Systems (LASI), Caparica, Portugal
Doutora Maria Manuela De Almeida Carvalho Vieira, Instituto Superior de Engenharia de Lisboa (ISEL), Instituto Politécnico de Lisboa (IPL), Universidade NOVA de Lisboa (UNINOVA), Center of Technology and Systems (CTS) and Associated Lab of Intelligent Systems (LASI), Caparica, Portugal

Novembro de 2025

Acknowledgments

This work stands for not only the conclusion of scientific research but also the culmination of a stage in my life that was marked by challenges, personal and academic growth. Dedication and resilience were essential to achieving this goal during these years of study and work. But no achievement is individual; behind every step I took, some hands supported me, and voices that encouraged me.

First, thank God. Thank you, mother, for being my pillar of unconditional support. Your sacrifices, wisdom, patience, and constant support have motivated me to continue. This achievement is as much yours as it is mine. My wife, thank you for your trust, love, patience, and sacrifice. To my family and friends, thank you for believing in me, encouraging me when my strength faltered, and constantly reminding me of the purpose of this journey.

I also thank the Instituto Superior de Engenharia de Lisboa (ISEL) for welcoming me as a foreign student and providing an excellent education. I thank all the teachers who went with me on this journey.

I would like to thank Dr. Alessandro Fantoni, supervisor of this dissertation, for his constant guidance, patience, and scientific rigor, and Dr. Paulo Lourenço for his availability, technical support, and valuable advice throughout this work.

This research was also made possible thanks to the institutional support of the following projects:

- IPL/IDI&CA2024/OPAPIC2D_ISEL
- ASER-META - Amorphous Silicon Optical Switch based on an Electrically Reconfigurable Metamaterial (2022.07694.PTDC)
- SYNOPSYS OSG University Donation Program

To all those who contributed in any way to the development of this project, my sincere thanks.

Statement of integrity

I declare that this dissertation is the result of my personal and independent research. Its content is original, and all sources listed in the bibliographic references were consulted and are duly mentioned in the text. I further declare that all scientific and technical references relevant to the development of the work are duly cited and included in the bibliographic references.

The author

Ernesto Velázquez

Lisbon, novembro 3, 2025

Design of a Programmable Photonic Integrated Circuit based on Carrier Depletion Phase Shifters.

Abstract

Photonic integrated circuits (PICs) have appeared in response to current technological challenges such as increased speed, demand for greater bandwidth and processing capacity, especially for applications that require extremely fast, high-performance data processing that Integrated Circuits (ICs) cannot satisfy. The range of applications for this technology includes ultra-fast data centers, optical communications, biosensors, sensors for vehicles, quantum processors, and Artificial Intelligence (AI). As this technology continues to advance, there is a growing academic and scientific need to contribute to technology, which in turn opens new market opportunities.

In this work, we will analyze the main optoelectronic properties of the materials used for PIC design and the latest advances in waveguide and coupler topologies, focusing on hydrogenated amorphous silicon (a-Si:H) as the main material and directional couplers as the main structure. An architecture will be proposed that looks to respond to problems in conventional directional couplers. It is also intended to use this new coupler design to create a programmable circuit that can be controlled by the Thermo-Optic Effect (TOE) and the Carrier Depletion Phenomenon (CDP). The methodology used integrates the most recent and classic studies of the mathematical and physical principles that govern these structures and materials, using analysis tools such as MATLAB and Python, with the aim of laying the theoretical foundations for the use of professional design tools. in our case, we will use Synopsys' Rsoft-CAD Layout, which implements advanced algorithms such as: Finite Difference Time Domain (FDTD), Beam Propagation Method (BPM), and Finite Element Method (FEM). In conclusion, a document will be presented that has the relevant theory of PICs and their control methods, as well as two functional solutions and their applications.

Keywords: photonic integrated circuits, thermo-optic effect, charge depletion phenomenon, finite difference time domain algorithm, beam propagation method, finite element method, programmable circuit, directional coupler.

Desenho de um circuito fotónico integrado programável com modulação de fase por depleção de portadores.

Resumo

Os circuitos integrados fotónicos (PICs) surgem em resposta aos desafios tecnológicos atuais, como o aumento da velocidade, a procura por maior largura de banda e capacidade de processamento, especialmente para aplicações que exigem processamento de dados extremamente rápido e de alto desempenho que os circuitos integrados (ICs) não conseguem satisfazer. A gama de aplicações para esta tecnologia inclui centros de dados ultrarrápidos, comunicações óticas, biossensores, sensores para veículos, processadores quânticos e inteligência artificial (AI). À medida que esta tecnologia continua a avançar, há uma necessidade académica e científica crescente de contribuir para a tecnologia, o que, por sua vez, abre novas oportunidades de mercado.

Neste trabalho, analisaremos as principais propriedades optoeletrónicas dos materiais utilizados para o design de PIC e os últimos avanços em topologias de guias de onda e acopladores, com foco no silício amorfo hidrogenado (a-Si:H) como principal material e nos acopladores direcionais como estruturas principais. Será proposta uma arquitetura que procura responder aos problemas dos acopladores direcionais convencionais. Pretende-se também utilizar este novo design de acoplador para criar um circuito programável que possa ser controlado pelo efeito termo-óptico (TOE) e pelo fenómeno de depleção de carga (CDP). A metodologia utilizada integra o estudo mais recente e clássico dos princípios matemáticos e físicos que regem estas estruturas e materiais, utilizando ferramentas de análise como MATLAB e Python, com o objetivo de estabelecer as bases teóricas para a utilização de ferramentas de design profissionais. No nosso caso, utilizaremos o Rsoft-CAD Layout da Synopsys, que implementa algoritmos avançados como: Finite Difference Time Domain (FDTD), Beam Propagation Method (BPM) e Finite Element Method (FEM). Em conclusão, será apresentado um documento com a teoria relevante dos PICs e seus métodos de controlo, bem como duas soluções funcionais e suas aplicações.

Palavras-chave: circuitos fotónicos integrados, efeito termo-óptico, fenómeno de esgotamento de carga, domínio do tempo de diferença finita, método de propagação de feixe, método dos elementos finitos, circuito programável, acoplador direcional.

List Acronyms

AI	Artificial Intelligence
ANNs	Artificial Neural Networks
AR	Anti-Reflective
ASIC	Application-Specific Integrated Circuit
ASPICs	Application-Specific Photonic Integrated Circuits
AWG	Arrayed Waveguide Grating
BPM	Beam Propagation Method
CAD	Computer Aided Design
CAP	Carrier Accumulation Phenomenon
CDP	Carrier Depletion Phenomenon
CIP	Carrier Injection Phenomenon
CLB	Configurable Logic Blocks
CMT	Coupled Mode Theory
CPM	Cross-Phase Modulation
DC	Direct Current
DFT	Discrete Fourier Transform
DWDM	Dense Wavelength Division Multiplexing
EMP	Electromagnetic Phenomena
EOE	Electro-Optic Effect
EOMs	Electro-Optic Modulators
ER	Extinction Ratio
FBG	Fiber Bragg Grating
FCPDE	Free-Carrier Plasma Dispersion Effect
FDTD	Finite Difference Time Domain
FEM	Finite Element Method
FFT	Fast Fourier Transform
FOM	Figure Of Merit
FPGA	Field Programmable Gate Array
FPPGA	Field Programmable Photonic Gate Arrays
FSR	Free Spectral Range
HSDC	Horn-Slab Directional Coupler
HWCVD	Hot-Wire Chemical Vapor Deposition
ICs	Integrated Circuits
IL	Insertion Loss
IoT	Internet Of Things
LiDAR	Light Detection And Ranging
MMI	Multi-Mode Interferometer
MMRs	Micro-Ring Resonators
MOS	Metal–Oxide–Semiconductor

MZI	Mach–Zehnder Interferometer
NoC	Network-On-Chip
PASPICs	Programmable Application-Specific Photonic Integrated Circuits
PECVD	Plasma-Enhanced Chemical Vapor Deposition
PICs	Photonic Integrated Circuits
PL	Propagation Loss
PPAB	Programmable Photonic Analog Blocks
PPICs	Programmable Photonic Integrated Circuits
QAM	Quadrature Modulation
QPSK	Quadrature Phase Shift Keying
RASPICs	Reconfigurable Application-Specific Photonic Integrated Circuits
RF	Radio Frequency
RPI	Reconfigurable Photonic Interconnections
SISCAP	Silicon Insulator Silicon Capacitor
SPM	Self-Phase Modulation
TE	Transverse Electric
TM	Transverse Magnetic
TOE	Thermo-Optic Effect
TOPS	Thermo-Optic Phase Shifters
VFB	Flat Band Voltage
VHF PECVD	Very High Frequency Plasma-Enhanced Chemical Vapor Deposition
VS Code	Visual Studio Code
WDM	Wavelength Division Multiplexing

List of Materials

Ag^+	Silver Ion
Al	Aluminum
a-Si:H	Hydrogenated Amorphous Silicon
Au	Gold
BCB	Benzocyclobutene
β-BaB_2O_4	Beta-Barium Borate
CMOS	Complementary Metal Oxide Semiconductors
CNTs	Carbon Nanotubes
Cu	Copper
GaAS	Gallium Arsenide
H	Hydrogen
H_2	Molecular Hydrogen
InP	Indium Phosphide
KD_2PO_4	Potassium Di-Deuterium Phosphate
$LiNbO_3$	Lithium Niobate
Na^+	Sodium Ion
poly-S	Polysilicon
Si	Silicon
Si_3N_4	Silicon Nitride
SiCOH	Silicon Carbon-Doped Silicon Dioxide
SiH_4	Silane
SiO_2	Silicon Dioxide
SiO_xN_Y	Silicon Oxynitride
SOI	Silicon On Insulator
Ti	Titanium
W	Tungsten
Zn	Zinc

List of symbols and units

Latin letters (A–Z)

A	Cross-sectional area	μm^2
B	Magnetic flux density	T
C	Heat capacity per unit volume	J/(m^3·K)
$C_{d_{ox}}$	Oxide layer capacitance (per area)	F/m^2
C_t	Thermal capacity	J/K
c	Speed of light in a vacuum	m/s
D	Electrical displacement	C/m^2
E	Electric field	V/ m
e	Electron charge	C
G_t	Thermal conductance	W/K
H	Magnetic fields	A/m
I	Optical intensity	W/m^2
K	Kerr constant (electro-optics)	m/V^2
k	Thermal conductivity	W/(m·K)
m	Mass	kg
m_e	Mass of the electron	kg
m_{ce}^*	Conductivity effective masses of electrons	kg
m_{ch}^*	Conductivity effective masses of holes	kg
M	Magnetization	A/m
n	Refractive index (real part)	-
n'	Complex refractive index	-
N_A	Acceptor concentration	cm^{-3}
P	Power consumed	W
P_π	Power required to induce a phase shift of π	mW
q	Heat flow	W/m^2
Q_{dep}	Depletion charge	C/m^2
Q_s	Charge per unit area	C/m^2
R	Reflectance (intensity)	-
R	Electric resistance	Ω
R_t	Thermal resistance	K/W
S	Cross-sectional area	μm^2
T	Temperature	K
V	Volume of material	μm^3

v_m	Speed of light in the medium	m/s
v_s	Velocity of sound	m/s
W_m	Width of the surface depletion region	μm

Greek letters (Romanized order)

α	Absorption coefficient	m^{-1}
β	Propagation constant	rad/μm
γ	Collision frequency	s^{-1}
Δ	variation	-
ε	Permittivity	F/m
ε_0	Vacuum permittivity	F/m
ε_r	Relative permittivity	-
η	Tuning efficiency	-
κ	Extinction coefficient	-
κ	Coupling coefficient	1/μm
λ	Wavelength	μm
Λ_{eff}	Free path of the phonons	μm
μ	Permeability	H/m
μ_0	Vacuum permeability	H/m
μ_r	Relative permeability	-
μ_e	Electron mobility	$cm^2/(V\cdot s)$
μ_h	Holes mobilities	$cm^2/(V\cdot s)$
ρ	Material density	kg/m^3
ρ_e	Electrical resistivity	Ω·m
τ	Time constant	s
ϕ	Phase	rad
ϕ_s	Surface potential	V
χ	Electrical susceptibility (tensor)	-
$\chi^{(1)}$	First-order susceptibility (linear)	-
$\chi^{(2)}$	Second-order susceptibility (quadratic)	-
ω_p	Angular plasma frequency	rad/s

Contents

List of figures

List of tables

1 Introduction

Electronic integrated circuits (ICs), developed after the transistor's discovery (Bardeen, Brattain, and Shockley, 1947) [1], drove miniaturization and cost per function. Freeman accurately predicted that the cost of transistors would steadily decrease over time due to Moore's Law, which says that transistor density doubles every two years [2]. However, as data rates and integration grow, electrical interconnects become the bottleneck, as processing capacity and bandwidth are limited, heat dissipation, power consumption, latency, and crosstalk penalize long and fast links.

Currently, the demand for technology driven by increased bandwidth consumption continues to grow, with the expansion of 5G data networks and advances in 6G, artificial intelligence (AI), cloud platforms, data centers, autonomous vehicles, robotics, the Internet of Things (IoT), and more efficient industrial processes cannot be met sustainably with electronic microchip technology alone [3]. In this context, photonic integrated circuits (PICs) have appeared as the technological evolution of integrated circuits (ICs), applying the same principles of planar integration and mass processing to miniaturize and densify optical functions. A basic PIC can consist of two or more optoelectronic elements, depending on the desired application or functionality, which can be classified as passive or active components. Passive components include waveguides, directional couplers, Y-branches, Bragg grating filters, micro-ring resonators (MMRs), and interferometers such as Mach–Zehnder (MZI), Michelson, or Sagnac. Active components include lasers, modulators, and detectors (sensors). These components can be easily integrated into a single chip, resulting in a compact and efficient device. Just as integrated circuits integrate transistors, PICs integrate "photonic blocks" connected by guides, such as "optical wiring," on the substrate. Lithography provides alignment and stability. Manufacturing them in batches results in compact, robust systems with scalable costs.

As shown in Figure 1.1, market studies show forecast growth in the industry of fifty-four trillion in USD by 2035, which translates into high growth, driven by applications such as Optical Communication, AI, Sensing, Bio-photonics, Optical Signal Processing, and Quantum Computing, among others. Among the industries with the highest demand are Data Centers, Telecommunications, Consumer Electronics, Defense & Aerospace, Industry, Automotive, among others, with North America, Europe, and Asia Pacific being the main regions of development for this industry [4, 5].

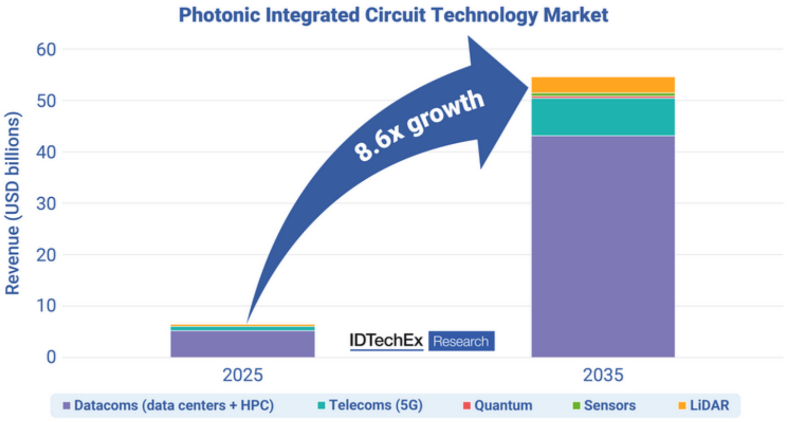

Figure 1.1 – PIC market forecast. (Source: [4]).

Among the materials used for the manufacture and development of PIC devices, whether in monolithic or hybrid solutions, three platforms have been standardized, as can be seen in Figure 1.2: Indium Phosphide (InP), Silicon on Insulator (SOI), and Silicon Nitride (Si_3N_4-SiO_2) [6]. When choosing the substrate, the required functionality must be considered, as well as the compatibility between materials and manufacturing processes, given that some are more complex than others. For example, SOI solutions share the same manufacturing processes as Complementary Metal Oxide Semiconductors (CMOS). In contrast, in the case of InP, the process is specific in that it offers direct laser integration.

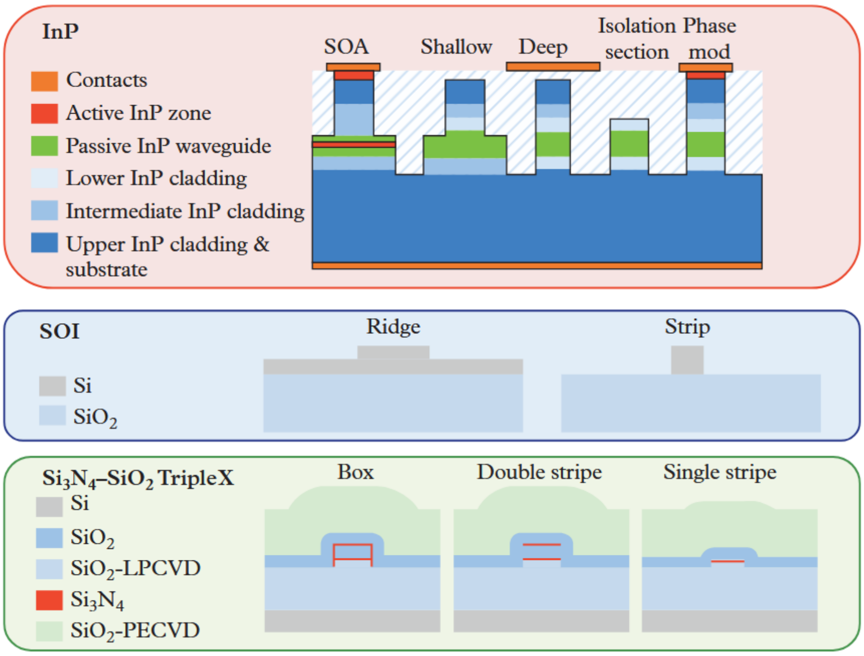

Figure 1.2 – Platforms and materials used in PIC, InP (upper row), SOI (intermediate row), and Si_3N_4-SiO_2 (lower row). (Source: [6]).

ICs exploit the strong interaction of electrons to achieve nonlinear switching (transistors), while PICs exploit the weak interaction of photons to enable high-bandwidth guidance, modulation, and detection on a chip [7]. The design of these devices focuses on how to propagate light (losses, evanescent coupling, dispersion, absorption) in dielectric waveguides, and optoelectronic control techniques are used to implement routing and optical signal processing, often taking advantage of wavelength division multiplexing (WDM) [8].

PICs adopted the successful techniques achieved by ICs, which implement a planar process, batch manufacturing, and hierarchical design. ICs are classified into two types depending on their functionality: Application-Specific Integrated Circuit (ASIC), which is designed and built for a specific application or purpose without the possibility of modifying or reprogramming its functions, and Field Programmable Gate Array (FPGA), which is determined by its general use based on the use of Configurable Logic Blocks (CLB) and programmable connections, making it possible to reprogram its functionalities depending on its resources.

For their part, PICs developed the analogue of ASICs, implementing Application-Specific Photonic Integrated Circuits (ASPICs) integrating just the blocks necessary for a specific function, such as a WDM transceiver with filters, rings/modulators, and photodetectors. In the FPGA model of ICs in their photonic version, Field Programmable Photonic Gate Arrays (FPPGA) [6] were developed, in which the photonic version called Programmable

Photonic Analog Blocks (PPAB) are used in an analogous way to CLBs. Through Reconfigurable Photonic Interconnections (RPI), these form a programmable photonic chip capable of simultaneously implementing one or more photonic circuits and multiport linear transformations [6, 9].

The concept of Programmable Photonic Integrated Circuits (PPICs) was extended in the case of ASPICs, giving rise to Reconfigurable ASPICs (RASPICs) [6] or also referred to as Programmable ASPICs (PASPICs) [10], allowing the reconfiguration of operating parameters such as phase, optical path, bandwidths, or switching states, offering functional elasticity to adapt to channels.

In PPICs, light routing is achieved by interconnecting waveguides, resulting in optical paths that, in turn, give rise to a mesh structure, using interconnection blocks between the optical paths [11]. The basic blocks are created mainly from three elements, as shown in Figure 1.3: a) directional coupler, b) multi-mode interferometer (MMI) directional coupler [12, 13], and c) micro-ring resonator directional coupler (MRRs) [14, 15], with directional couplers (a) being one of the most implemented options. All three configurations are typically used in dense networks, resulting in FPPGAs solutions.

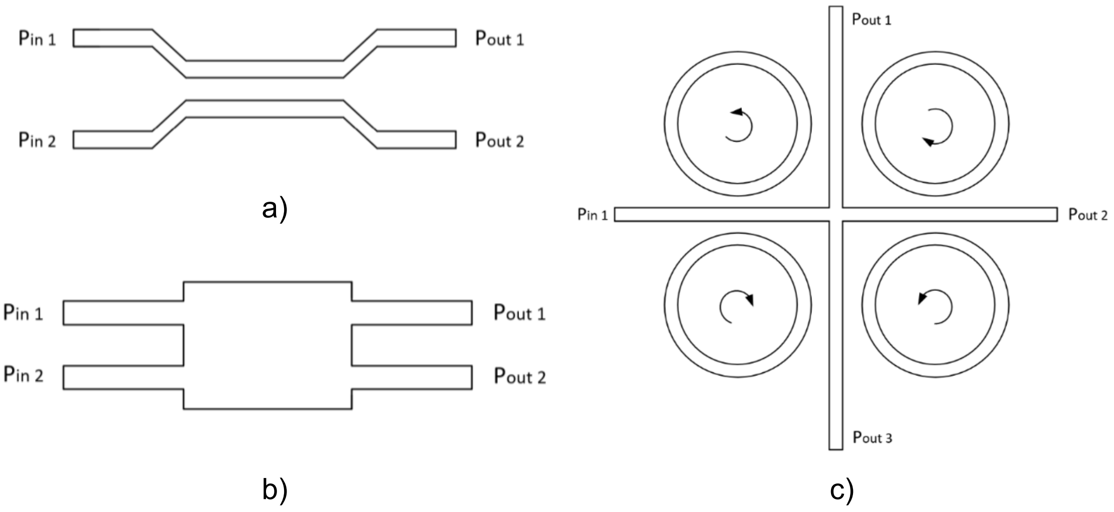

Figure 1.3 – Elemental building blocks of programmable photonics, a) directional coupler, b) MMI directional couplers, and c) micro-ring resonator directional coupler.

As mentioned above, using directional couplers as the main element quickly became immensely popular. Using this element, in 2015, Zhuang proposed a square mesh topology, adding feedback (loops) within the circuit [16], as can be seen in Figure 1.4. Then, in 2016, Capmany proposed triangular/hexagonal meshes [17], using the same concepts.

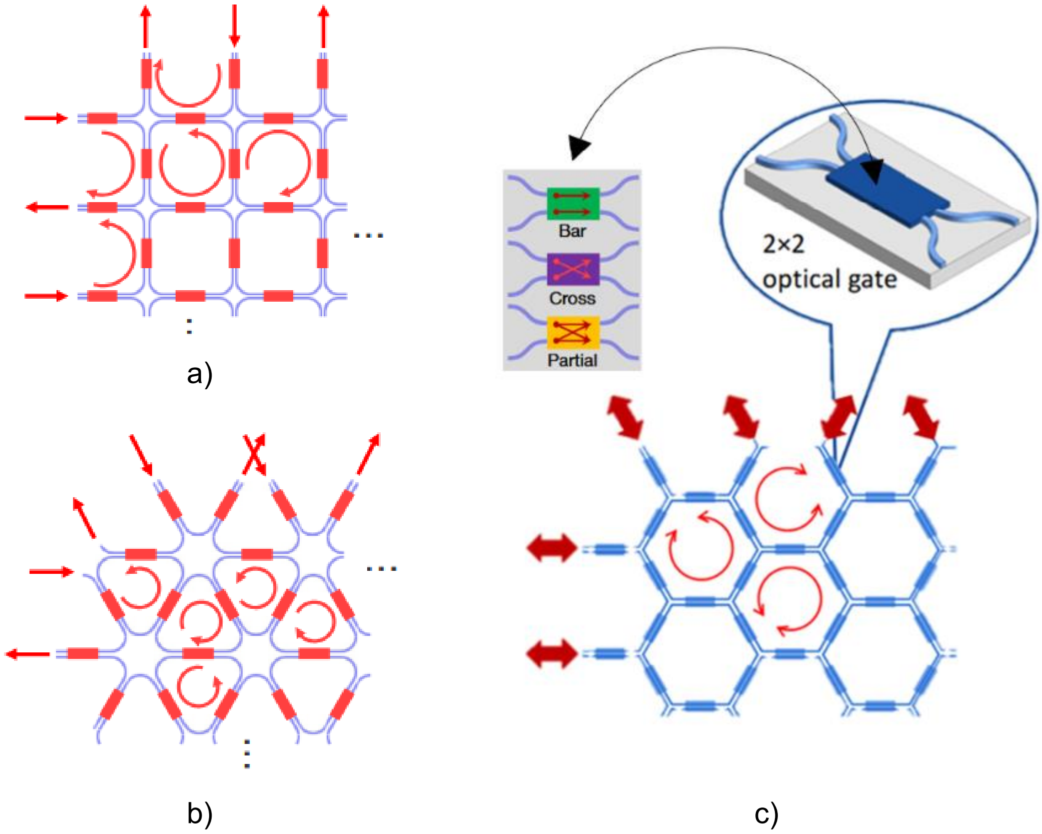

Figure 1.4 – Waveguide meshes with recirculation topology based on directional couplers: a) square cell, b) triangular cells, c) hexagonal cells. (Source [18]).

These blocks are passive blocks that, depending on their design, redirect, distribute/combine according to their geometry (coupling length and separation), and are incapable of dynamically selecting the direction of the optical signal. Optoelectronic configurations based on physical phenomena that interact with the material, changing its optical properties, are used to have dynamic routing capability. Among these techniques, the use of configurations with thermo-optic heaters, depletion/injection in pn, pin, or Metal–Oxide–Semiconductor (MOS) junctions, the Pockels effect in $LiNbO_3$, the Kerr effect, or electro-absorption in III–V compound semiconductors (e.g., indium phosphide (InP) and gallium arsenide (GaAs)), among other used mechanisms [19].

1.1 Context and motivation

Integrated photonics has become a short and long-term solution for communications, sensing, computing, and, increasingly, for quantum and artificial intelligence (AI) applications. This rapid technological growth is accompanied by strong market growth, creating opportunities in academia and in the professional world to learn and master the fundamental concepts of PICs. In this context, Europe, as one of the main markets and centers of technological development, places Portugal in a position to develop and contribute to this advance in the face of this new challenge.

When searching the current literature for more information on control processes or techniques, in many cases, these methods are not detailed, making it difficult for readers with basic knowledge of the subject. Although we assume that the authors believe that readers have knowledge of these aspects, and that the publications have a results-oriented approach, it is still essential in some instances to know the methods and physical bases that make up the solution. For example, recent publications mention the thermo-optic effect (TOE) as a control element [11, 20, 21], with the other methods not being as detailed as mentioned above. Based on this, there is a need to analyze other forms of control, which can be found in specialized literature and are sometimes not easy to understand, given the complexity or different mathematical notations used for analysis. This is why there is a need to create a document that, while not definitive, provides the reader with the basic knowledge to understand control mechanisms and technical details.

This work focuses on studying and analyzing the main principles of PICs and addressing design techniques that provide a starting point for designing programmable photonic components and circuits, with a special focus on directional couplers as the main element. This work, therefore, has dual motivation: (i) to analytically understand the physical phenomena and optical properties on which PICs are based, and (ii) to propose configurations and design guidelines that can be transferred to platforms compatible with CMOS/SOI processes.

1.2 Research questions

The directional coupler as the main element, is implemented using S-bends to bring two parallel rectangular segments closer together or further apart, as shown in Figures 1.3 a) and 1.4 c). Therefore, the coupler has a dimension that forms the area of interest (coupling zone) and the length of the S-bend at each port. This in itself poses a problem, given that in dense solutions where space must be optimized due to the absorption/attenuation phenomena present in the materials, the following issues associated with the geometry and design of the s-bends may arise: (i) extra losses associated with curvature (bend loss), (ii) modal mismatch, (iii) “parasitic” coupling in the curved areas produced in the approaches/departures, (iv) extra phase increase, and (v) possible imbalances compromised by symmetry. At the manufacturing level, there are problems associated with manufacturing sensitivity, since slight variations in gap/width in the curves compromise both the propagation constant and the coupling coefficient κ. Analyzing the above raises the following question:

1. Is it possible to optimize the design of the directional coupler to eliminate or minimize the problems mentioned above by using amorphous silicon as the main material?

The effective coupling of modes is described by Coupled Mode Theory (CMT) [22], which establishes that coupling depends mainly on the separation between guides s, which directly influences κ; For a given L, there is always a critical separation s at which the guides do not couple. The values of s for guides with $L \leq 1\text{mm}$ are normally $s \approx 0.25\ \mu m$, and for values greater than $s \approx 0.65\ \mu m$, there is no coupling between the guides. For example, with coupling for $s \approx 0.25\ \mu m$, at this proximity between guides, the manufacturing technology must be more precise and therefore more expensive. In university laboratories, it is possible to create an amorphous silicon layout for a minimum distance of $s \geq 1\ \mu m$. The analysis of the above raises the following sub-question related to the earlier question.

   1.1. Is it possible to optimize the design of the directional coupler to achieve coupling at $s \geq 1\ \mu m$?

In thermal control applications using heaters, thermal crosstalk occurs because of a reduced distance. If increasing the distance between the guides can minimize this, a sub-question arises related to the question asked above.

      1.1.1. Once the design has been optimized to achieve coupling at $s \approx 1\ \mu m$, does this design mitigate thermal crosstalk, and if so, to what extent?

Once the above analysis has been conducted, two solutions based on directional couplers with RASPIC functionality will be proposed. The first is to create a 4x4 matrix using TOE, and the second is to create a 4x4 matrix using Carrier Depletion Phenomenon (CDP).

Once the design of both devices has been completed, the following questions arise.

1.2. Between TOE and CDP, which is more energy efficient, which has lower Insertion Loss (IL) at the input, and which delivers higher optical power at the output (lower propagation loss (PL)) in a 4×4 array of directional couplers?

1.3 Methodology

First, a general review and in-depth analysis of the current literature will be conducted, including various reviews of articles from renowned scientific journals, as well as relevant content. Older articles that are referenced in more recent studies will also be reviewed. The review will include books, encyclopedias, various analyses of laboratory tests and published results, and consultation of databases of electro-optical materials of interest.

This work aims to lay theoretical foundations, limiting the analysis to waveguides, directional couplers, and the main control effects. This synthesis provides us with an analysis model based on fundamental principles and their scope of validity, as well as a set of parameters that allow us to design and optimize PIC solutions, such as thicknesses, doping levels, and material selection.

Within this framework, we will derive first-order analytical models, such as the temperature estimation, the potential needed to obtain a phase change or control the direction of a directional coupler, interferometric responses, the estimation of the doping level, and absorption. We will implement this step-by-step analysis in MATLAB/Python scripts to explore these models and their principles analytically.

After creating the theoretical foundations, we will use more advanced tools/methods, such as RSoft CAD software, which implements more specialized algorithms, with which we will confirm the theory analyzed above and better understand how it is implemented in a professional environment.

Finally, we will merge everything into a document that aims to integrate the fundamental concepts so that the reader can move from theory to a manufacturable design with clear criteria.

1.4 Scope and organization of the thesis

This work is organized into five chapters, comprehensively covering the basic principles and main control theories of programmable PICs, laying the theoretical foundations in a single document that the current bibliography does not detail in a single structure. The chapters are structured as analyses with a bibliographic review component, which includes papers, books, encyclopedias, and experimental databases, together with an analytical review of the mathematical and physical formulations and expressions in the present, with as many images as possible for better reading and understanding of the content.

The work did not address topics such as lithography and manufacturing processes, given the length of the document and its objectives. However, current references were provided where the reader can investigate and analyze. Among the content that was not addressed and is relevant at a more complex level of knowledge are modal analysis, analysis of nonlinear effects, passive devices such as Y-branches, Bragg grating filters, ring resonators (MMRs), and interferometers (Mach–Zehnder), and active devices such as lasers, modulators, and detectors.

Chapter 1 introduces the reader to current technology and its importance. It also covers the main research questions on which the work is based, the methodology implemented, and the final results of the thesis.

Chapter 2 addresses the main optoelectronic properties and effects on which the design of PICs is based. In addition to presenting the theory behind them, this chapter analyzes the main architectures of phase modulators based on different control techniques (optoelectronic effects). It provides an analytical demonstration of various methods and optical properties.

Chapter 3 analyzes waveguides and directional couplers as passive elements. As an effective refractive method, we analyze the Marcatili method, one of the techniques used for 2D analysis, and briefly introduce the simulation tools and methods used during the work.

Chapter 4 proposes the Horn-Slab Directional Coupler as the main control element, which is then used to implement two solutions: i) one using the thermo-optic effect as a control technique and ii) using the Carrier Depletion Phenomenon as a control technique. All solutions are characterized, and the results obtained are detailed, serving as a guide for the design of photonic devices, whether in ASPIC, RASPIC, or FPPGA solutions.

Chapter 5 presents the conclusions of this project, prepared in response to the objectives proposed in Chapter 1. This chapter also includes objective considerations about the project carried out and perspectives for future work.

Finally, at the end of this document, all the bibliographic references consulted are described, and references in which the reader can delve deeper into those contents that were not addressed as mentioned initially, including the analysis scripts for each chapter.

1.5 Scientific Output

Several studies were conducted on the main topics proposed in this paper during the course of this work. These investigations resulted in several scientific publications, which can be accessed at:

- "Design of a 2×2 Programmable Matrix of Silicon Photonic Switches Based on Mach-Zehnder Interferometer Structures Using the Thermo-Optic Effect," *2025 9th International Young Engineers Forum on Electrical and Computer Engineering (YEF-ECE)*, Caparica / Lisbon, Portugal, 2025, pp. 157-162, https://doi.org/10.1109/YEF-ECE66503.2025.11117252

- Computer simulation of a 2D optical phased array in end-fire configuration. In *Physics and Simulation of Optoelectronic Devices XXXIII* (Vol. 13360, pp. 98-105). SPIE. https://doi.org/10.1117/12.3042447

- A Reconfigurable 1x2 Photonic Digital Switch Controlled by an Externally Induced Metasurface." *Photonics*. Vol. 12. No. 3. MDPI AG, 2025. https://doi.org/10.3390/photonics12030263

Among the works pending publication are the following, which are works that are intended to be published before the end of the current year 2025. These works are titled:

- Horn-Slab Directional Coupler and Applications. *(Under Submission in Journal Photonics from MDPI).*

- Main optoelectronic control techniques applied to programmable photonic circuits: state-of-the-art and a review.

- Design of a 4×4 programmable photonic array based on amorphous silicon controlled by the carrier depletion phenomenon.

2 Fundamental optical properties and main optoelectronic effects

There are a variety of materials used for PIC fabrication, including indium phosphide (InP) [23, 24], used in active laser generation, amplification, control, and detection, ideal for communication and sensing applications. Lithium niobate ($LiNbO_3$) [25, 26, 27], as a low-loss modulator. Gallium arsenide (GaAS) [28, 29], its high electron mobility is advantageous as a driver of analog integrated circuits for lasers and high-speed modulators. In terms of electronic integration, silicon is the most widely used material in optoelectronics, the second most abundant element in the Earth's crust after oxygen. Thanks to its low manufacturing cost and optical properties, it can be easily doped as n-type and p-type semiconductors. Moreover, deposition techniques can obtain it in its amorphous form (a-Si:H). This last is particularly prevalent in photovoltaic applications and has garnered considerable interest in optoelectronic applications in recent decades. In terms of technological compatibility and performance, this material offers several benefits, thus making it an excellent candidate for selecting materials for a specific application. The manufacturing infrastructure has been exploited due to breakthroughs in the mass production of electrical circuits, such as processors and electronic integrated circuits. This compatibility eases the integration of photonic and electronic devices on the same chip in Complementary Metal-Oxide-Semiconductor (CMOS) technology, thereby reducing costs and enhancing efficiency. In this chapter, we present the main optical properties of materials in general and their main optoelectronic effects. These concepts form the theoretical basis for the choice of materials and the design of photonic circuits.

2.1 Fundamental optical properties

The study of light and its interaction with various materials have been thoroughly explored and researched in classical physics and photonics. Given the current importance of optical devices in technology, understanding the optical properties of materials is essential. The variations that light undergoes when interacting with a particular substance or material are known as the optical properties of the element. These properties are studied in isolated elements for greater precision in their determination.

The optical properties of materials are influenced by a combination of macroscopic and microscopic characteristics, as well as the nature of their surface and electronic structure. There are different optical properties, the most well-known of which are reflection, refraction, transmission, and absorption. Many of these properties are associated with key optical constants, including the refractive index and the extinction coefficient.

It is well known that the refractive index of a material (n), is represented as the ratio between the speed of light in a vacuum (c) and the speed of light in that medium (v) defined as,

$$n = \frac{c}{v} \ , \tag{2.1}$$

using Maxwell's equations, which describe the behavior of electric and magnetic fields in material media, we can derive the relationship for the refractive index from the electromagnetic wave equation [8]. The electromagnetic wave equation in a medium with permittivity (ε) and permeability (μ) is expressed as,

$$\nabla^2 \vec{E} = \mu\varepsilon \frac{\partial^2 \vec{E}}{\partial t^2} \ , \tag{2.2}$$

from which we obtain the well-known formula for the refractive index of a material as,

$$n = \sqrt{\varepsilon_r \mu_r} \ , \tag{2.3}$$

where ε_r is the relative permittivity (dielectric constant) and μ_r is the relative magnetic permeability. It can be proved that, for non-magnetic substances, $\mu_r = 1$. Consequently, $n = \sqrt{\varepsilon_r}$, holds a meaningful relationship when relating the dielectric properties of a material to its optical properties at any given frequency. Since ε_r depends on the wavelength of the light, the refractive index depends on it as well, which is known as dispersion [9]. The complex permittivity is defined as,

$$\varepsilon_r = \varepsilon_1 + i\varepsilon_2 \ , \qquad 2.4$$

$$\varepsilon_1 = \ n^2 - \kappa^2, \quad \varepsilon_2 = \ 2n\kappa \, , \qquad 2.5$$

where ε_1 represent the real part and $i\varepsilon_2$ the imaginary, κ represent the extinction coefficient indicates the amount of absorption loss when the electromagnetic wave propagates through the material, n and k are dependent on the wavelength and the medium. For values where $k \ > 0$, light undergoes absorption and so less propagation.

There are various methods for finding the optical constants of thin films, and these values are obtained experimentally. The optical constants n and k are determined by measuring the reflectance of a material's surface as a function of polarization and angle of incidence for a given wavelength, making it possible to calculate the absorption coefficient [30]. A study published in [31] analyzes how these values are obtained using a conventional spectrophotometer or a monitoring device in the evaporation chamber, employing a more straightforward method with results comparable to those of more elaborate techniques.

The complex index is used to describe both propagation and absorption in a material; this is expressed as the ratio between the refractive index n (real) and the extinction coefficient κ (imaginary) as,

$$n' = n + i\kappa \ , \qquad 2.6$$

from the relationship in equation 2.5, we have that,

$$n' = \left[\frac{(\varepsilon_1^2 + \ \varepsilon_2^2\ )^{1/2} + \ \varepsilon_1}{2}\right]^{1/2} , \qquad 2.7$$

$$k = \left[\frac{(\varepsilon_1^2 + \ \varepsilon_2^2\ )^{1/2} - \ \varepsilon_1}{2}\right]^{1/2} . \qquad 2.8$$

As is known from Fresnel's laws [32], reflectivity (r) is an optical property of materials that determines the ratio between the reflected and incident fields in its complex form. This reflection is not random, but depends on the texture of the material's surface, its refractive index, the angle of incidence of the light source, and polarization, for normal incidence, r is obtained as,

$$r = \frac{1 - n'}{1 + n'} \ . \qquad 2.9$$

Reflectance (R) is the measure we use to quantify reflectivity. It is the ratio of reflected/incident power (or intensity). It takes values between 0 and 1 and can be spectral $R(\lambda)$, directional, hemispheric, etc. [33], and is represented as,

$$R = |r|^2 = \frac{(n-1)^2 + \kappa^2}{(n+1)^2 + \kappa^2} \; . \tag{2.10}$$

These equations allow us to predict the behavior of light as it passes from one material to another, based on the refractive index of each medium. The reflection and transmission coefficients are calculated for analytical approximations based on the use of a refractive index, that is, ignoring losses. This means that, to simplify calculations, we consider any absorption or scattering effects to be negligible. This approximation is useful when the losses are insignificant or when approximate values are simply wished for.

The absorption coefficient (α) is one of the most important parameters when analyzing optoelectronics materials, as it decides the extent to which light of a particular wavelength can penetrate the material before being absorbed. The absorption coefficient depends on the material as well as the wavelength of the light being absorbed, through its relationship with the extinction coefficient, and is defined as,

$$\alpha = \frac{4\pi}{\lambda}\kappa \; , \tag{2.11}$$

from this relationship, in a complex index medium, when κ increases, the attenuation for a given wavelength (λ) also increases, so that the incident (non-reflected) light is attenuated at a small penetration depth. At the same time, the reflectance at the interface approaches 1 (i.e., all the light is reflected). These conditions cause the parameters n, λ, and R defined in equation 2.10 to depend directly on the wavelength (spectral), considering the angle of incidence and polarization.

In semiconductors, the refractive index is influenced by factors such as the material's crystal structure, composition, and band gap. Since semiconductors have a high electron density, light interacts with these electrons, resulting in a refractive index significantly higher than in dielectric materials [34]. Additionally, in semiconductors, the refractive index is dispersive, meaning it depends on the wavelength of light and is also sensitive to temperature variations.

2.2 Silicon and Amorphous Silicon

In the first part of this chapter, we mentioned the benefits and advantages of silicon as a material for optoelectronic applications. In our work, we will develop two solutions using amorphous silicon as the main material, so at this point, we will talk about the main differences between these materials, as well as the different methods for obtaining them. Although it is not the aim of this work to delve into these methods, as well as the lithography methods for the creation of photonic devices, it is advisable to review the references for each case.

The Si and the a-Si:H as materials show differences due to their structural disparities, electronic properties, and composition [34]. In the case of Si, it has a highly ordered and consistent crystal lattice; on the other hand, a-Si:H shows a random atomic structure, lacking long-range periodicity. This disordered structure induces differences in the density of electronic states and in the optical response, for example, to heat, which affects thermal dispersion and the sensitivity of the refractive index to temperature. In its natural state, Amorphous silicon shows a high absorption coefficient in the C band. To mitigate this phenomenon, hydrogen is added, resulting in the local modification of bonds and, so, the generation of a more complex optoelectronic response [35, 36].

Let us take the crystal lattice of both materials as a starting point. We can see in the Figure 2.1 (a), the representations of crystalline silicon has a cubic diamond-like structure, with each Si atom tetrahedrally coordinated with four neighbors, whereas in the case of amorphous silicon show in (b), the atoms are randomly distributed, hydrogen atoms (H) are added to the asymmetric bonds, and these defects are passivated when stable Si-H bonds are formed, saturating the levels of randomness and restoring the semiconductor properties of the material.

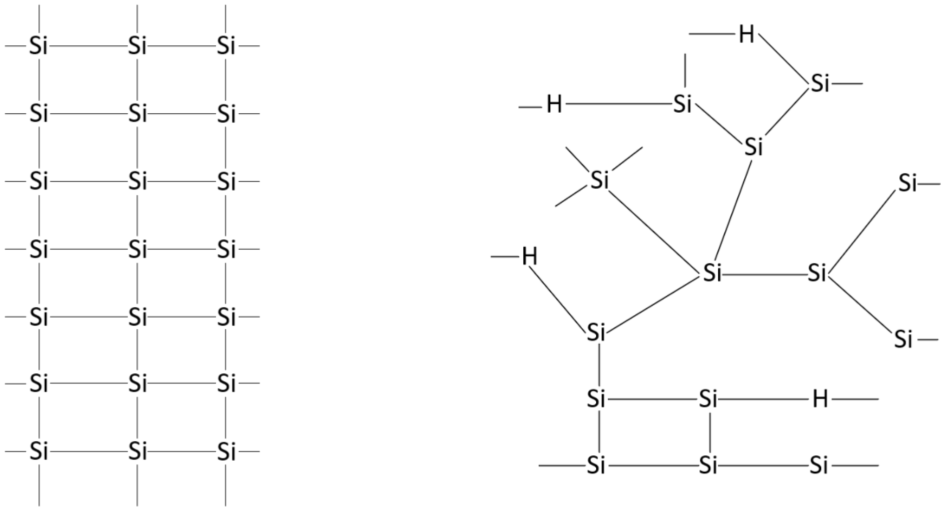

a) b)

Figure 2.1– Representation of the crystal lattice, a) silicon, b) amorphous silicon

Many broken bonds can make the material electrically inactive. Large numbers of hydrogen (or fluorine) atoms are incorporated into the film in the a-Si growth process to prevent these broken bonds from making the material useless in its application to optoelectronic components. The presence of these H atoms makes these broken bonds disappear, improving the properties of a-Si:H.

A major difference between amorphous and crystalline materials is the macroscopic symmetry of the material. In the case of Si, it has anisotropic symmetry (its properties depend on direction), while in the case of amorphous materials such as a-Si:H, they do not have a long-range ordered structure, since their macroscopic properties are generally isotropic (they do not depend on direction).

The anisotropy of crystals is characterized by the existence of planes along which it is easy to divide the crystal, due to the existence of a periodic order and well-defined crystallographic directions. In silicon, the crystal structure has a diamond (cubic) structure. In this structure, each atom is held together in the solid by four covalent bonds in a tetrahedral geometry (109.5°) with its four nearest neighbors. In this structure, each atom shares one of its outer electrons with each of its four neighbors.

Several deposition techniques, both physical and chemical, are used to produce a-Si:H. Among the most used in industry are Hot-Wire Chemical Vapor Deposition (HWCVD) [37, 38], Plasma-Enhanced Chemical Vapor Deposition (PECVD) [39, 40], and, more recently, Very High Frequency Plasma-Enhanced Chemical Vapor Deposition (VHF PECVD) [41]. In a-Si:H, short-range coordination is preserved (each atom supports its immediate tetrahedral neighborhood), but the long-range atomic network lacks periodicity and is described by the random network model, which, in principle, holds no regions of crystalline order.

The ease of manufacturing a-Si:H using the techniques mentioned above allows it to be integrated with Complementary Metal-Oxide-Semiconductor (CMOS) technology at temperatures between $T \approx ((293.15 - 673.15)K,$ (20 - 400) °C, well below the thermal budget of CMOS metallization in finished circuits, given that copper interconnections deteriorate above $T \geq 673.15K$ [42]. This advantage allows it to be easily incorporated into chip manufacturing processes [43]. The use of high-quality SOI wafers is not a prerequisite for the deposition of a-Si:H but can be achieved by direct deposition on standard 200/300 mm wafers.

Another advantage is the slightly higher refractive index of a-Si:H than Si (λ = 1.55 µm). This makes it possible to achieve greater optical confinement, which is a crucial factor in the design of structures with a small radius of curvature. This results in more compact devices that are relevant in scalable environments, such as dense photonic networks. The absence of crystalline orientation in a-Si:H results in isotropic optical properties and internal stress. The hydrogen fraction can be used to control these stresses, which helps design curved guides. In PECVD a-Si:H, the intrinsic film stress (tensile ↔ compressive) is controlled by the SiH_4/H_2 ratio, RF power, and pressure. Low-temperature anneals can relax the stress towards zero, which prevents bowing and cracking and preserves the geometry of tight-radius bends. This reduces bend loss and improves layout density [44].

Furthermore, the incorporation of dopant levels during the manufacturing process results in a material with these characteristics, expanding its applications in Metal-Oxide-Semiconductor (MOS) technologies [45]. These characteristics make hydrogenated amorphous silicon a low-cost, high-density photonic platform that is fully compatible with CMOS manufacturing, ideal for next-generation programmable circuits.

As part of the analysis, graphs of complex refractive index vs wavelength λ (µm) have been created in Figure 2.2 for Si and Figure 2.3 for a-Si:H using Python. This script collects values from works published on the database website created by Mikhail Polyanskiy, available at [46], carried out for both materials by Daniel Franta, available at [47], which can be viewed and downloaded at [48].

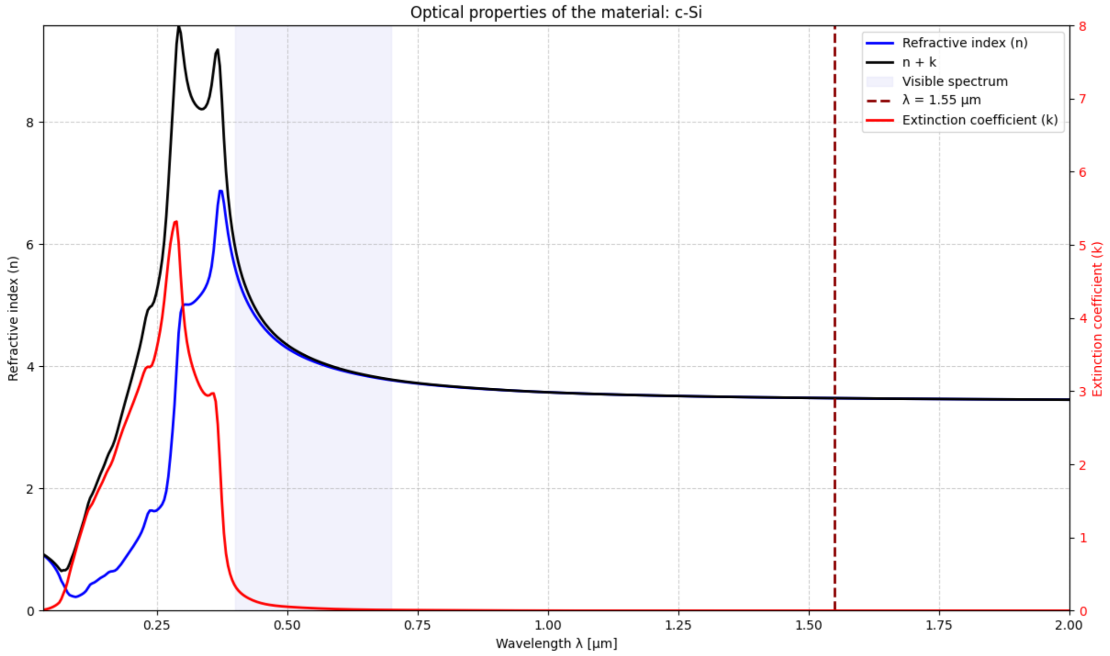

Figure 2.2 – Complex refractive index for Si vs wavelength λ (µm).

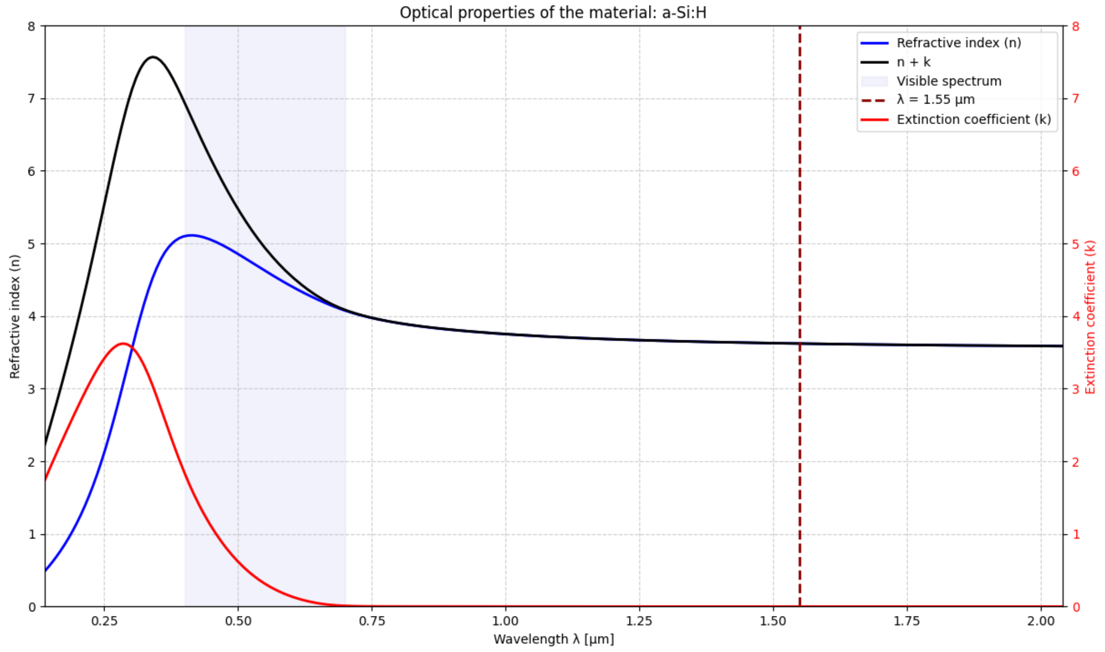

Figure 2.3– Complex refractive index for a-Si:H vs wavelength λ (µm).

These results from Franta's work will be used in our materials library, given that the RSoft CAD Layout allows materials to be created within the library. This way, we will have real parameters from more recent studies for our simulation. In our case for a-Si:H, it was identified as a-Si:H_Franta, as shown in Figure 2.4

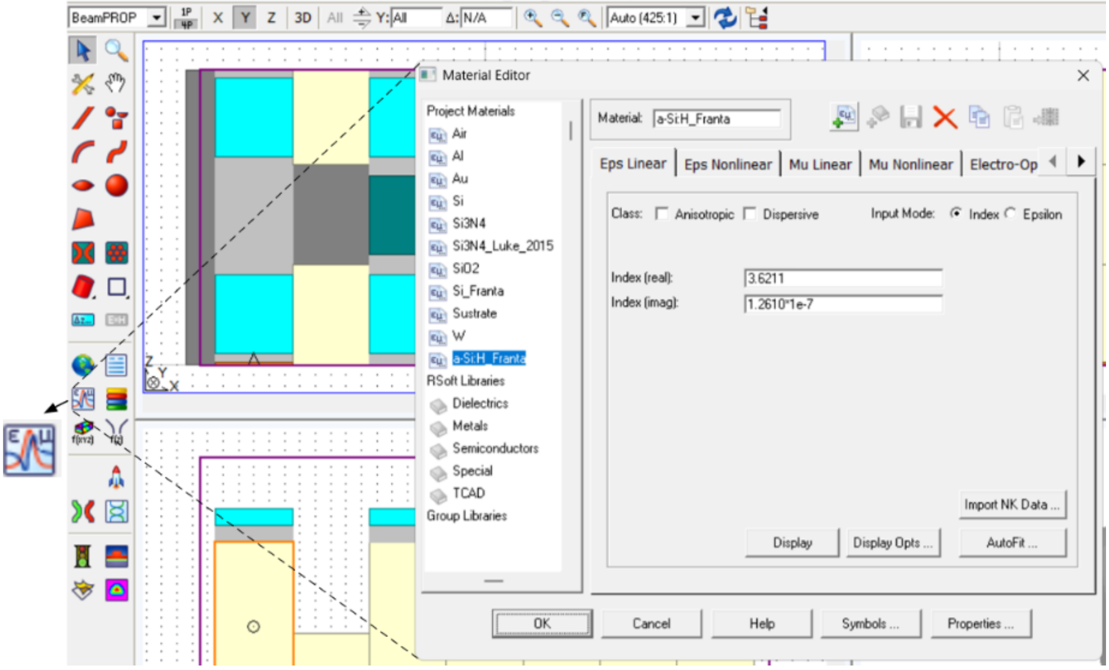

Material: a-Si:H_Franta

Class: ☐ Anisotropic ☐ Dispersive

Input Mode: ● Index ○ Epsilon

Index (real): 3.6211

Index (imag): 1.2610*1e-7

Figure 2.4 – Material editor in RSoft CAD environment

2.3 Principles of the Thermo-Optic Effect

The thermo-optical effect figures out the interaction of optical properties concerning temperature variation. These parameters depend on the material in question and its physical properties; one of its applications and uses of most significant interest in photonic devices is the behavior of the refractive index of a material when a temperature change occurs. This effect has been widely used in optoelectronics as well as in sensor technology for the realization of a variety of devices, primarily based on interferometric principles, such as optical switches, tunable filters, lasers, and fiber optic sensors [49].

To arrive at this principle in a general way, we will start with a brief analysis of classical thermodynamics, where these variations are caused by temperature as a system is observed. A thermal system has internal energy. This is also called thermal energy. It is the total energy of the molecules inside the system. The internal energy of a system is directly proportional to its absolute temperature. In case of two objects of differing temperatures being in contact with one another, energy is transferred from the object with a higher temperature to the object with a lower temperature until the bodies reach thermal equilibrium, i.e., until they are at the same temperature. Neither object does any work because there is no force acting across the distance [32].

It is known that there are fundamentally three types of heat transfer [50]:

- **Conduction**: Physical contact transfers heat through solid materials or a non-moving fluid.
- **Convection**: Heat transfer in liquids or gases by the macroscopic movement of fluid.
- **Radiation**: Heat transfer produced by the emission or absorption of microwaves, infrared radiation, visible light, or other forms of electromagnetic radiation.

Conduction heat transfer is the most common method used in PIC design, so we will briefly analyze its principles. In the manufacturing process, Silicon on Insulator (SOI) is the standard wafer for PICs, where the optical lithography (Photolithography) technique is implemented [51, 52, 53].

For a more precise analysis, we can use Figure 2.5, where two elements with different temperatures, Th (hot), and Tc (cold), are joined by a segment of length L and area A, for $\mathrm{Th}>\mathrm{Tc}$. This situation can be analyzed using Fourier's law of heat conduction, which states that heat transfer velocity through a material is proportional to the temperature gradient, i.e., the heat vectors flow from the hottest to the coldest, as mentioned above. This is in terms of energy, that the kinetic energy in a body with a hot temperature T_h is greater than the kinetic energy in a colder body Tc, upon contact, energy transfer occurs from $\mathrm{Th} \rightarrow \mathrm{Tc}$, the cumulative effect of these collisions is determined as the heat flux from $\mathrm{Th} \rightarrow \mathrm{Tc}$, and the rate of temperature transfer is determined as the difference between the media $\Delta\mathrm{T} = \mathrm{Th} - \mathrm{Tc}$.

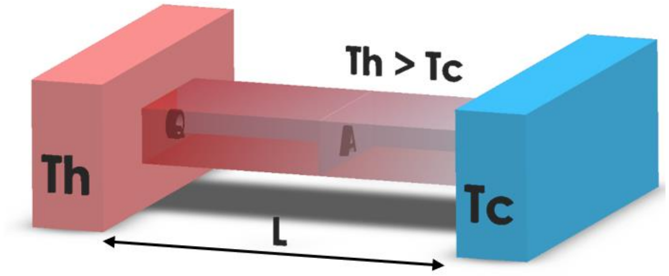

Figure 2.5 – Representation of heat transfer between two elements for Th>Tc

It can be postulated that if the concept of heat flow is considered a vectorial magnitude in all directions in a plane (x, y, z), expressing the Fourier conduction law for an arbitrary point, we have that,

$$\vec{q} = -\mathrm{k}\nabla T \,, \tag{2.12}$$

were k is the thermal conductivity of the material. In a rectangular coordinate system, the flow in (x, y, z) coordinated are,

$$q_x = -\mathrm{k}\frac{\partial T}{\partial x}, \quad q_y = -\mathrm{k}\frac{\partial T}{\partial y}, \quad q_z = -\mathrm{k}\frac{\partial T}{\partial z}, \qquad 2.13$$

for the components in (x, y, z), the general heat flow equation can be represented as:

$$\nabla \cdot \vec{q} = -\mathrm{k}\left(\frac{\partial^2 T}{\partial x^2} + \frac{\partial^2 T}{\partial y^2} + \frac{\partial^2 T}{\partial z^2}\right). \qquad 2.14$$

The thermo-optic effect in waveguides changes the refractive index in the guide with temperature, introducing a phase change. Since metals commonly used as heaters have a higher refractive index and high losses, they are unsuitable for direct implementation on the waveguide. For this reason, material with low losses and a lower index than the waveguide is used to ensure confinement at the edges and low attenuation, such as silicon dioxide (SiO_2). Therefore, as a design criterion, we can say that the temperature generated in the heater is transmitted by conduction through an intermediate material to the waveguide.

The effective thermo-optic coefficient of the guided mode is defined as $\partial n_{eff}/\partial T$ also known as the thermal coefficient, for temperature variations ΔT, the effective index change is expressed as,

$$\Delta n_{eff} = \left(\frac{\partial n_{eff}}{\partial T}\right)\Delta T. \qquad 2.15$$

The phase accumulated by the mode along a section of length L_{eff}, is $\phi = \beta L = (2\pi/\lambda)\, n_{eff} L$, therefore, the phase variation is [54],

$$\Delta\phi = \frac{2\pi}{\lambda}\Delta n_{eff} \cdot L_{eff}, \qquad 2.16$$

where λ (µm) is the wavelength, L_{eff} is the effective heater length. As shown in equation 2.16, the phase variation depends on the waveguide length and the variation of the refractive index with the temperature, so we have two variables to obtain a value of $\Delta\phi$, the effective length and the effective index change with temperature.

2.3.1 Basic configurations

As the temperature increases, one effect, as we have seen above, is an increase in the refractive index, but at the same time, the phase of the signal changes. In applications such as modulators, these temperature-controlled devices are also known as thermo-optic phase shifters (TOPS).

When implementing the TOE as a control or modulation element, we can use different configurations, each of which responds to a need depending on the design implemented, seeking simplicity in some cases and more efficient control in others. These basic configurations can be seen in Figure 2.6. The idea is to place the heater as close as possible to the guide to heat it as efficiently as possible. It can also be seen that in some cases, one of the solutions results from combinations of other techniques, such as in Figure 2.6 e).

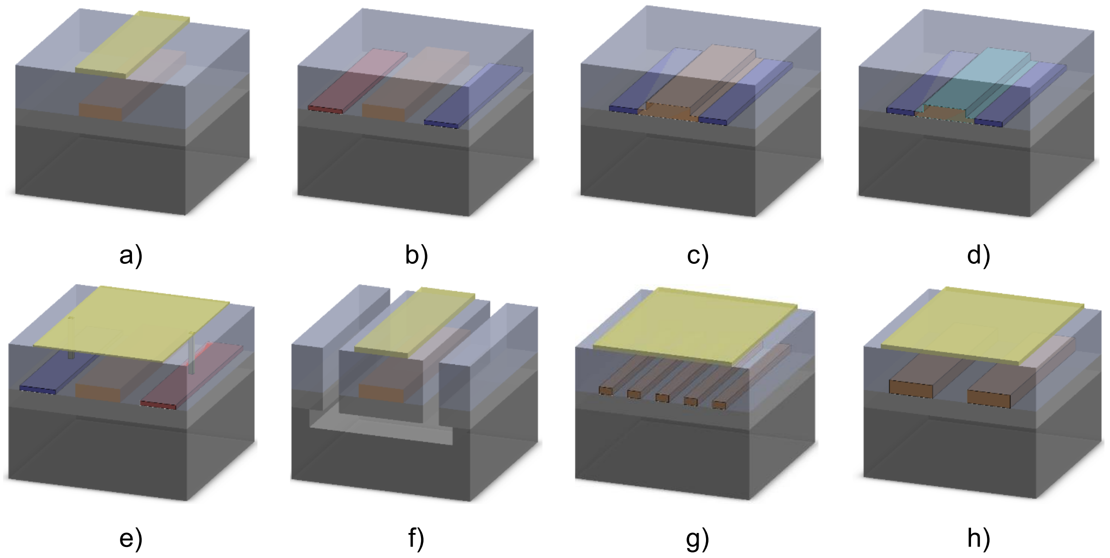

Figure 2.6 – Representations of different basic TOPS configurations: a) waveguide and metal heater on the top. b) waveguide with doped silicon heaters on both sides at symmetrical distance s. c) rib waveguide with doped silicon heaters on both sides. d) rib waveguide doped with and integrated doped silicon as heater. e) hybrid solution of a) and b). f) waveguide and metal heater on the top with trench for air gap and substrate undercutting. g) multiple separate waveguides with a metal heater on the top. h) based on multi-pass waveguides with a metal heater on the top. (Adapted from [21]).

Given that it is a popular and easy method to implement in the research community, new ways to improve the performance and applications of TOPS are being sought [54]. Several methods have been proposed and proven within this research, including air gaps or post-processing of silicon substrate undercutting, to maximize thermal insulation in folded waveguides and multi-pass waveguides. In addition, research continues into the relationship between energy consumption and thermal efficiency, one of the challenges of this technique, as well as the transition times between thermal variations [21, 55].

2.3.2 Resistive Heaters

We have analyzed the use of TOE/TOPS based solely on heat generation by an element external to the guide, but when we design our circuits, the analysis starts with a calculated temperature for our solution, and then we analyze how we generate the heat. At this point, heat generation can be reached by applying a voltage to its terminals; this voltage, together with the thermal resistance of the material, produces heat in the material by the Joule effect [50]. In these terms, our heater is a resistive heater as shown in Figure 2.7, and at this point we will perform this analysis, including a brief analysis of the materials used.

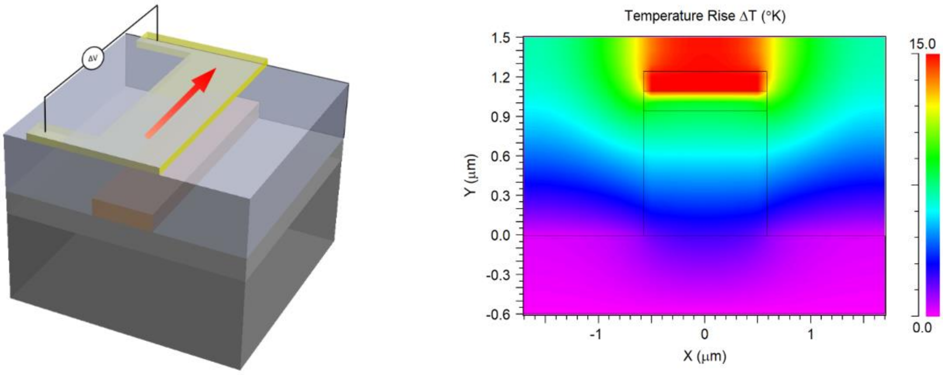

Figure 2.7 – Representation of a resistive heater and its thermal profile.

In thin metal and semiconductor films with thicknesses on the order of micrometers (~1–10 μm), heat is carried by the dominant energy carriers. In metals, this is produced by conduction electrons, and in semiconductors and dielectrics, it is produced by lattice vibrations (phonons). When the thickness of the film (*d*) is comparable to the mean free path (λ) of these carriers, they collide with the top surface and the film-substrate interface before travelling long distances, which reduces the effective thermal conductivity [56].

It is understood that phonons in a solid exhibit behavior analogous to that of particles in a gas with respect to energy transport [50]. Consequently, the thermal conductivity in solids is characterized as the heat flow resulting from the motions and interactions of phonons. Using this relationship, thermal conductivity can be calculated using the kinetic theory of gases in semiconductors, such as silicon, by the following expression [57],

$$\mathrm{k} = \frac{1}{3} C v \Lambda_{eff} \qquad 2.17$$

where k the thermal conductivity of the material is, C represents the heat capacity per unit volume, v describe the velocity of sound and Λ_{eff} is the free path of the phonons, k of the film is usually lower than that of the bulk material.

The thermal resistance of a plane wall is calculated using the following expression [58],

$$R_t = \frac{L}{\mathrm{k}A} \ , \qquad 2.18$$

were, A is the cross-sectional area to heat flow, and L is the thickness of the layer; to define the thermal conductance we have the following expression,

$$G_t = \frac{1}{R_t} \ . \qquad 2.19$$

Another important concept to analyze is the thermal capacity C_t, also called specific heat, is how much heat a material can hold. It is important in heat transfer processes because it determines how long it takes to reach the same final temperature. In other words, the more thermal capacity, the longer it takes to reach the same final temperature. The thermal capacity defined by [59],

$$C_t = \rho c_p V = m c_p \ , \qquad 2.20$$

were ρ define the material density, V is the volume of material, m their mass and c_p the specific heat at constant pressure.

In a first-order thermal RC model, the thermal time constant τ can be defined as [60],

$$\tau = \frac{C_t}{G_t}, \qquad 2.21$$

where the heat capacity of the heated segment including the area A traversed by the heat flux, that is, the cross-section of the waveguide perpendicular to the heat flux, τ denotes the switching time, and the electric resistance is given by [21],

$$R = \rho_e \frac{L}{A} \ , \tag{2.22}$$

where ρ_e represents the electrical resistivity of the material.

The temperature variations ΔT caused by the resistive heater can be expressed as two regimens [21]:

i. **Short transition** (adiabatic): where the heating occurs through as,

$$\Delta T = \frac{\eta P}{C_p \rho V} \ , \tag{2.23}$$

where P is the power consumed by the resistive heater (dissipated electrical power), η is the utilization tuning efficiency of drive power, representing the fraction of the electrical power dissipated by the resistive heater (power that really raises the temperature), usually between 0.2 and 0.8. $V = L_{eff}S$ is the volume effectively heated, for the cross-sectional area of the waveguide S and their effective length L_{eff}, ρ is the material density of the waveguide, C_p is the heat capacity of the waveguide. For a pulse of duration τ we can write equation 2.23 as,

$$\Delta T_{st} = \frac{\eta P}{C_p \rho V} \tau \ , \tag{2.24}$$

ii. **Steady state**: when the system reaches thermal equilibrium, the temperature variation is defined as,

$$\Delta T_{ss} = PR \ . \tag{2.25}$$

Joule heating stipulates that an increase in temperature is directly proportional to the power consumed by the microheater, denoted as $\Delta T \propto P$. Accordingly, the power consumption of the TOPSs, specifically the power required to induce a phase shift of π, is denoted as P_π can be formulated using the following equation [54],

$$P_\pi = \frac{\lambda}{2L} \left(\frac{\partial n_{eff}}{\partial P_{elec}} \right)^{-1} \ . \tag{2.26}$$

In the context of microheater operation, the variation of the effective refractive index with the electrical power applied to the microheater is represented by $(\partial n_{eff})/(\partial P_{elec})$. In the case of TOPS where the direction of propagation is invariable outside the heated segment, the variation is proportional to the active effective length of the heater; the necessary power can be expressed in terms of the P_π , as the ratio between the temperature variation, the thermal conductance per cross-sectional area to heat flow as,

$$P_\pi = \Delta T_\pi G_t A \,. \qquad 2.27$$

This means that it is possible to use smaller, more powerful heaters in the waveguide segment instead of a heater of length L, but as a trade-off, a higher temperature is required, translating into higher potential and longer times between states. One of the current solutions to minimize this phenomenon is the implementation of transparent heaters, such as graphene and carbon nanotubes (CNTs) [54]. These techniques remain to be analyzed and studied in future work.

To evaluate the performance of TOPS, the following Figure Of Merit (FOM) is commonly used and is defined as [54],

$$FOM = P_\pi \tau = \Delta T_\pi C_t \ . \qquad 2.28$$

This represents the minimum thermal energy that must be stored in the heated region to induce a phase change of π; therefore, the lower the FOM, the better for greater efficiency.

Based on the above definitions, it is possible to apply Ohm's law to electrical circuits in their power form. In this way, it is possible to estimate the voltage value necessary to achieve a variation in π, which is defined by [61],

$$V_\pi = \sqrt{P_\pi R} \ . \qquad 2.29$$

2.3.3 TOE/TOPS in Silicon and Amorphous Silicon

As we have seen previously, the foundations have been laid for analyzing the thermo-optic effect and its analytical model as a phase shifter. Although we mentioned that the work is based on amorphous silicon, at this point, given the importance of silicon, we will perform the above analysis on these two materials based on the mathematical models presented in the previous study, together with a brief analysis of the metals most commonly used for these applications.

In the case of Si, the thermal coefficients used for the analysis were obtained based on the cross-reference published in [21], over the temperature range (300 - 600)K as,

$$\frac{\partial n_{(Si)}}{\partial T} = 9.45 \times 10^{-5} + 3.47 \times 10^{-7} \times T - 1.49 \times 10^{-10} \times T^2 \ , \tag{2.30}$$

and with interest in our work on amorphous silicon obtained in [62], at temperatures ranging from (300 - 473.15)K as,

$$\frac{\partial n_{(aSi:H)}}{\partial T} = -7.36 \times 10^{-5} + 1.43 \times 10^{-6} \times T - 1.44 \times 10^{-9} \times T^2 \, . \tag{2.31}$$

For this analysis, a script was created in MATLAB, which is available at [63]. Based on the above equations, it analyzes the temperature variation in semiconductors Si and a-Si:H. These graphs can be seen in Figure 2.8, and the BP Mode Solve tool simulations for the TOE can be seen in Figure 2.9.

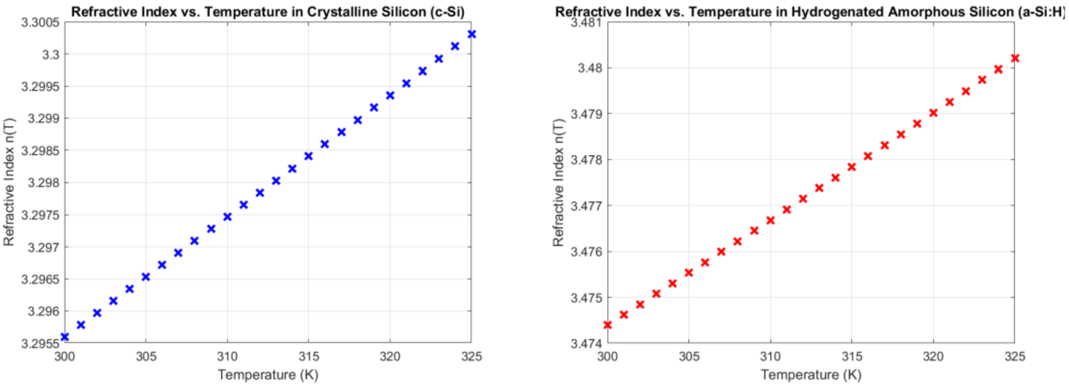

a) b)

Figure 2.8 – Analytical result of the refractive index variation vs. temperature variation in: a) Si, b) a-Si:H.

Although equations 2.30 and 2.31 model the thermo-optic coefficient dn/dT as a quadratic function of temperature, its variation is modest, as can be seen in Figure 2.8. Therefore, it can be said that the value of N_{eff} increases almost linearly with T.

The graphs obtained in Figure 2.9 were simulated for the following parameters: $L=L_{eff}=500\ \mu m$, $\lambda=1.55\ \mu m$, for a value of $\Delta T=15K$. The values of n_{eff} for both materials were obtained by simulation using the FemSIM tool for $n_{eff_{(Si)}} = 3.2956$ and $n_{eff_{(aSi:H)}} = 3.474395$. These values can be obtained analytically using Marcatili's approximation, an analysis we will perform in the next chapter.

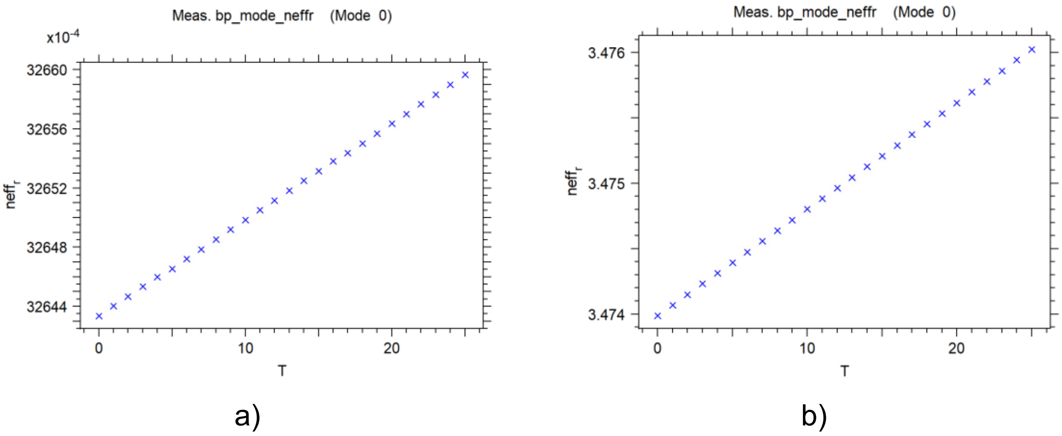

a) b)

Figure 2.9 – Simulated result in BP Mode Solver of the refractive index variation vs. temperature in: a) Si, b) a-Si:H.

In the case of simulations obtained using the BeamPROP method, the parameters were the same as those simulated previously. Both results are quite close, given that BeamPROP performs the estimate by calculating the point-to-point propagation at ΔT for each point. The analytical method is valid for approximation with a margin of error of 0.02 with respect to the values analyzed in the professional simulation. The next chapter will discuss how the BeamPROP method works. In the same script, we have the analytical calculations for the temperature required for specific phase shifts (multiples of π), referred to in equation 2.16. Table 2.1 shows the values obtained for Si, and Table 2.2 for a-Si:H, the same parameters of wavelength λ and longitude assuming $L = L_{eff}$.

Table 2.1 – Temperatures needed for specific phase shifts for Silicon.

$\Delta\phi\ (\pi)$	$T(K)$	$\Delta T(K)$
$\pi/2$	305	5
π	309	9
$3\pi/2$	313	13
2π	317	17

Since a resistive heater is used to transfer heat to the guide, it is first necessary to know the thermal and electrical properties of each material to calculate the voltage needed to obtain the previously calculated temperature. Table 2.3 shows the main materials currently used as heaters. This data and other information were compiled and can be consulted in [64, 65]. Among the most popular options consulted in the bibliography [66, 67, 68], which takes into account manufacturing costs, ease of implementation, and available technology, are gold, tungsten, titanium, and doped silicon. For our analysis, gold was selected as the electrode.

Table 2.2 – Temperatures needed for specific phase shifts for Amorphous Silicon.

$\Delta\phi$ (π)	$T(K)$	$\Delta T(K)$
$^{\pi}/_{2}$	304	4
π	307	7
$^{3\pi}/_{2}$	311	11
2π	314	14

Table 2.3 – Various materials used as resistive heaters**.**

Materials	Electrical Resistivity (Ω·m)	Thermal Conductivity (W/m·K)	Thermal Diffusivity (mm^2/s)	Specific Heat Capacity (J/Kg·K)	Thermal Effusivity ($\sqrt{Ws}/m^2$·K)
Gold (Au)	2.44e-8	317.98	129	128	28027
Aluminum (Al)	2.65e-8	225.94	91	921	23688
Copper (Cu)	1.68e-8	397.48	116	385	36983
Tungsten W)	5.28e-8	196.65	76.1	134	22543
Titanium (Ti)	4.20e-7	20.92	8.89	523	7017

Using the equations referred to in Appendix 2.3.2, we can analytically deduce the potential values necessary to reach the temperatures already calculated in Table 2.2 for a-Si:H, which is the material of interest to us. This analysis can be found in the script identified as "*TOE-TOPS_Resisitive_analysis*" available at [63], and the results are shown in Table 2.4, for a height of 0.1 um, and calculated for a short pulse of 1 ms, given as a result, $\tau = 3.152\mathrm{e}^{-06} s$ and $FOM_\pi = 5.709\mathrm{e}^{-09} J$.

Table 2.4– Calculated power and voltage parameters for the gold resistive heater.

$\Delta\phi$ (π)	$\Delta T(K)$	Power [mW]	Potential [V]
$^{\pi}/_{2}$	4	0.005437	0.025907
π	7	0.009514	0.034272
$^{3\pi}/_{2}$	11	0.014951	0.042962
2π	14	0.019028	0.048467

It is important to mention that metal is not everything, given that heat transfer occurs through conduction, P_π is often decided by the thermal insulator. For example, it is common on SOI platforms to use SiO_2 or Si_3N_4, although it is possible to use other oxides and materials as silicon carbon-doped silicon dioxide (SiCOH) [69], polymers as benzocyclobutene (BCB) [70] and graphene [21], to mention just a few examples. A better insulator improves G_t (reduces R_t), lowers P and therefore V, which is a ratio of electrical/thermal efficiency. This is another analysis that is still pending for further work.

2.4 Principles of Electro-Optic Effect

It has been known that certain materials can undergo a change in their optical properties when subjected to an electric field. This phenomenon can be attributed to the presence of forces that result in the distortion of the positions, orientations or shapes of the molecules that make up the material. The Electro-optic effect (EOE) is a second order non-linear optical effect in which the presence of a low frequency electric field can induce a change in the refractive index of a material [71]. Given these elements, we can define the electro-optical effect as the change in the refractive index of a material induced by the presence of a static (or low frequency) electric field, this representation can be seen in Figure 2.10, where the electric field generated by the source and its terminals induces the effects that we will analyze below.

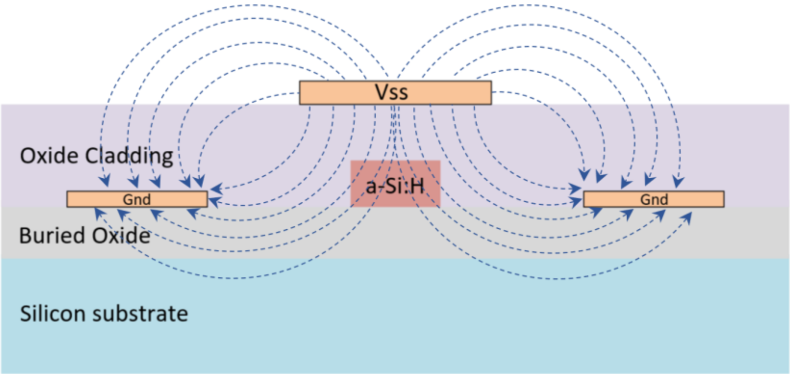

Figure 2.10 – Representation of the electro-optic effect in a-Si:H waveguide.

In some materials, due to their crystalline orientation and properties, the change in refractive index shows a linear variation with respect to the intensity of the applied electric field [72]. An electric field applied to a material with an anisotropic electro-optical response (its physical properties, such as resistance, conductivity, or rigidity, are not the same in all directions) change its refractive indices and therefore generates an effect on polarized light. The dependence of the refractive index on the applied electric field takes one of two forms [7]:

- The refractive index changes in proportion to the applied electric field, in which case the effect is known as the **linear electro-optic effect** or the **Pockels effect**.

- The refractive index changes in proportion to the square of the applied electric field, in which case the effect is known as the **quadratic electro-optic effect** or the **Kerr effect**.

In most cases, the change in refractive index is negligible; however, its effect on an optical wave propagating a distance much greater than a wavelength of light in each medium can be significant. Materials whose refractive index can be changed by an applied electric field are of use in the production of electrically controllable optical devices like the following examples [7]:

- A lens made of a material whose refractive index can be varied is a lens of controllable focal length.
- A controllable prism can be used as an optical scanning device due to its beam-bending ability.
- As a controllable optical phase modulator, when light is transmitted through a transparent plate, a controllable variation in its refractive index occurs, generating a phase change proportional to the external electric field.
- An anisotropic crystal whose refractive indices can be changed serves as a wave retarder of controllable retardation; it may be used to change the polarization properties of light.
- A wave retarder placed between two crossed polarizers results in transmitted light whose intensity is dependent on the phase retardation. The transmittance of such a device is therefore electrically controllable so that it can be used as an optical intensity modulator or an optical switch.

A representation of the electro-optic effect is shown in Figure 2.11.

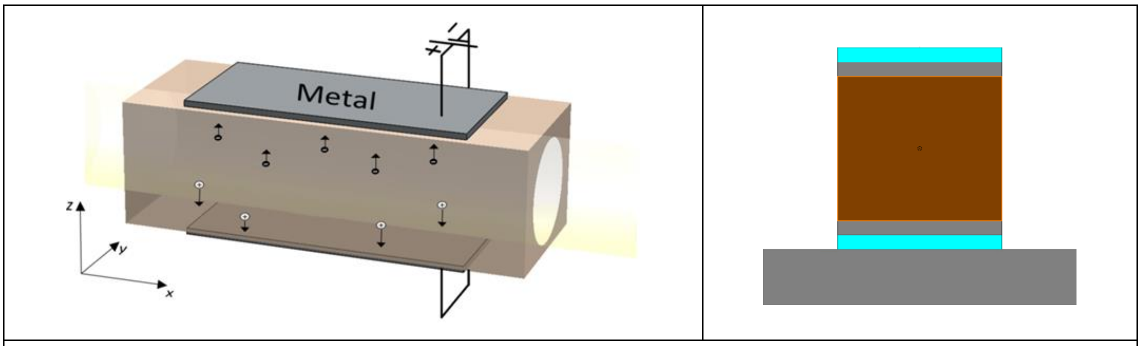

Figure 2.11 – Electric field applied to an electro-optic waveguide.

In the case of a rectangular electro-optic guide where applying a constant electric field to a guide induces a variation in its refractive index, simultaneously modify the optical parameters of the light passing through said field.

As a result of a simulation with parameters recreated to better visualize the effect for an electro-optic material, based on Figure 2.11 and shown in Figure 2.12, when the applied electric field $\Delta E = 5V$ and the effect of the field on the refractive index of the material.

Control by EOE is especially useful in optical signal processing applications as well as in fiber optic communications. Alternatively, it is possible to use the electric field to change the optical properties of a material through absorption. Since a semiconductor material is optically transparent to light if the wavelength being analyzed is greater than the wavelength of the band gap. However, by applying an electric field, it is possible to reduce the band gap of the material, thus easing absorption and converting the material from transparent to opaque [73]. This phenomenon, called electro-absorption, has found important applications in the field of optical modulators and switches [74].

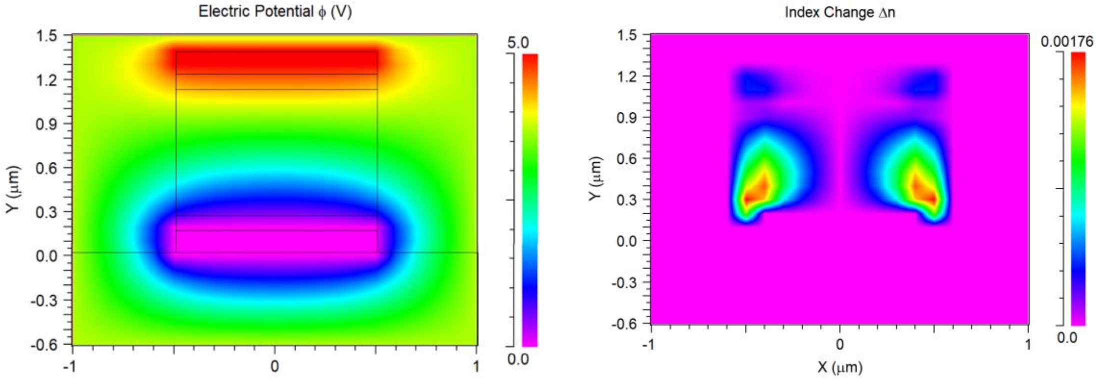

a) b)

Figure 2.12 – Representation of the electro-optic effect, a) application of an electric field, b) variation of the refractive index due to the applied potential.

From the above, we can determine that the electro-optical effect can be divided according to its effects into:

Changes in absorption:

- **Franz-Keldysh effect** is defined as a change in optical absorption by a semiconductor when an electric field is applied [75]. The Franz-Keldysh effect manifests as the smearing of the absorption edge in semiconductors under conditions of high electric fields. While Franz and Keldysh's study focused on a specific instance of an externally applied uniform electric field, it is noteworthy that similar effects can be produced by built-in electric fields present at semiconductor surfaces and interfaces [76].

- **Quantum confinement Stark effect**: is a modification of the absorption process of quantum wells in certain semiconductors. When semiconductors are fabricated in very thin layers, the optical absorption spectrum changes radically because of the quantum confinement of carriers in the resulting one-dimensional potential wells [77].

Changes in refractive indices and permittivity:

- **Free carrier effects** are widely used to change the refractive index and absorption coefficient in Si-based optical modulators.
- **Pockels effect** (or linear electro-optical effect): change in refractive index linearly proportional to electric field.
- **Kerr effect** (or quadratic electro-optical effect): change in refractive index proportional to the square of the electric field or the intensity.

While mentioning some effects produced by interaction with an electric field, we will focus on analyzing the effects based on the change in refractive index. The effects of free carriers are deeply involved in the study of semiconductors so that they will be analyzed separately due to their particularities and importance.

2.4.1 Pockels Effect

The Pockels effect, first published in 1906 by German physicist Friedrich Pockels [78], is known as the linear electro-optic effect. It is characterized by the fact that the refractive index of a medium changes in proportion to the intensity of the electric field applied linearly. This effect has the peculiarity that it can only occur in non-centrosymmetric materials, as shown in Figure 2.13.

The most important materials of this type are crystal materials such as lithium niobate ($LiNbO_3$), lithium tantalate ($LiTaO_3$) [79], potassium di-deuterium phosphate (KD_2PO_4) [80], beta-barium borate (β-BaB_2O_4) [81], and compound semiconductors such as gallium arsenide (GaAs) and indium phosphide (InP), [82]. These crystals that work on the Pockels effect are called Pockels cells [83] for their use in different applications related to this effect. These materials are characterized by their transparency and high electro-optic coefficient, which results in a substantial change in refractive index when subjected to an electric field.

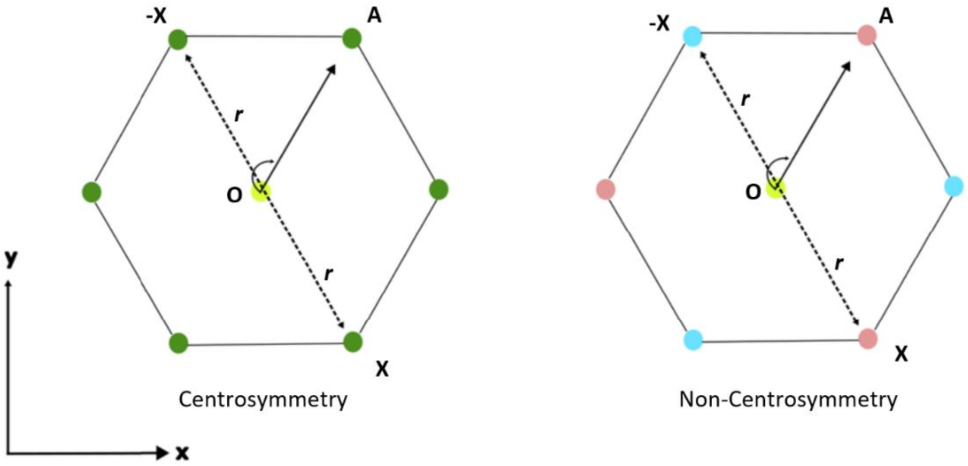

a) b)

Figure 2.13 – Crystal structure in 2D, a) centrosymmetric, b) non-centrosymmetric.

In this subsection, we will analyze the basis of this effect and its usefulness, starting from its principles, given that it is an extensive analysis that starts from Maxwell's equations [84] and their development in nonlinear optics, recommended reading [72, 85]. In this subsection, we aim to provide a general overview of the basics that will allow us to understand this phenomenon, so only the fundamental equations will be mentioned (all are important, but we will focus on those we will use for the mathematical development), starting from the relationship between the electric and magnetic fields, expressed in their vector field form as [86],

$$\vec{D} = \varepsilon_0 \vec{E} + \vec{P} \ , \tag{2.32}$$

$$\vec{B} = \mu_0 \left(\vec{H} + \vec{M} \right) \ , \tag{2.33}$$

$$\vec{P} = \varepsilon_0 \chi \, \vec{E} \ , \tag{2.34}$$

where equation 2.32 summarizes how a material responds to an electric field: the electric displacement $\vec{D}$ satisfies Gauss's law for free charge, ε_0 is the permittivity of free space, $\vec{E}$ is the applied electric field, $\vec{P}$ is the polarization of the medium (electric dipole moment per unit volume) that arises because the bound charges of the atoms/molecules shift slightly, creating dipoles, in a vacuum $\vec{P} = 0$, in this case the equations 2.32 can be define as $\vec{D} = \varepsilon_0 \vec{E}$. Equation 2.33 can be described as the magnetic analogue of equation 2.32 in dielectric materials. This equation decides the magnetic flux density $\vec{B}$ as the sum of the magnetic fields generated by both free sources $\vec{H}$ and the fields generated by the induced or permanent magnetic dipoles of the material $\vec{M}$, both conditioned by the vacuum permeability constant μ_0.

Equation 2.34 stands for the relations by which an electric field causes polarization (orientation of the electric dipole), guided by χ which is the electric susceptibility tensor, also known as linear susceptibility. This quantity is dimensionless and quantifies how easily a material polarizes in response to an applied electric field for each component of E in a plane. This is the linear constitutive law of a dielectric, applicable when the response is proportional to the field. This is typical of moderate optical fields and linear, homogeneous, and isotropic media. This is the linear constitutive law of a dielectric, valid when the response is proportional to the field. This law is typical in moderate optical fields and in linear, homogeneous, and isotropic media [87].

Relating equations 2.32 and 2.34, we have that [19],

$$\vec{D} = \varepsilon_0\left(1 + \chi^{(1)}\right)\vec{E} = \varepsilon_0\varepsilon_r\vec{E} \ , \qquad 2.35$$

were by definition,

$$\varepsilon_r = 1 + \chi^{(1)} \ , \qquad 2.36$$

by its relation to n in equation 2.3, we can write n as,

$$n = (1 + \chi\,)^{1/2} \ . \qquad 2.37$$

Considering that in anisotropic media χ is analyzed as linear susceptibility, when analyzing dispersive media, the frequency response must be considered for this $\chi = \chi(\omega)$, as it can be complex $\Re\{\chi\}$) sets the change in phase (index) and $\Im\{\chi\}$ determines the absorption. For our analysis and for ease, we will address isotropic media.

The effective susceptibility can be written as a series in the applied quasi-static field, of the form $\chi\,(E) = \chi + \chi^{(1)}(E) + \chi^{(2)}(E^2) + \chi^{(3)}(E^3) + \cdot\cdot\cdot$, in the limit of the linear regime, the comprehensive response is analyzed in a series of powers represented by,

$$P = \varepsilon_0\left[\chi^{(1)}\vec{E} + \chi^{(2)}\vec{E}^2 + \chi^{(3)}\vec{E}^3 + \chi^{(n)}\vec{E}^n + \cdots\right] , \qquad 2.38$$

where $\chi^{(1)}$ is the first-order (linear) polarizability as a second-order tensor this determines the index of refraction; the quadratic term $\chi^{(2)}$ is the second-order polarizability as a third-order tensor, which has appreciable value only in piezo-electric crystals; the cubic term $\chi^{(3)}$ is the third-order polarizability as a fourth-order tensor, describes the tripling of the light frequency [88]. This relationship explains the nonlinear phenomena related by the dependence of the refractive index as shown in Figure 2.14. Although it is not the aim of this study, it is important to be aware of these phenomena.

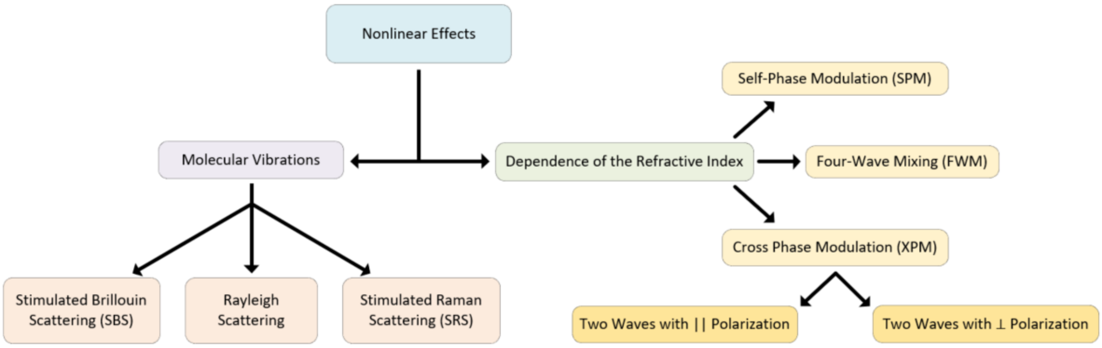

Figure 2.14 – Nonlinear effects and their main categories. (Adapted from [85]).

Using the expansion in series of E for each term of χ as shown in the equations 2.38, and substituting this relationship into equation 2.37, we can express the refractive index dependent on the electric field using the following relationship,

$$n(E) = (1+\chi(E))^{1/2} = (1+\chi+\chi^{(1)}(E)+\chi^{(2)}(E^2)+\cdots)^{1/2} \qquad 2.39$$

after expanding the first term in Taylor series, we have that [7, 79],

$$n(E) \approx n - \frac{1}{2}\mathrm{r}n^3E - \frac{1}{2}sn^3E^2 - \cdots , \qquad 2.40$$

were r, s are known as electro-optic coefficients, r represents the **linear electro-optic tensor** (Pockels coefficients), and s corresponds to the **quadratic electro-optic tensor** (Kerr coefficients) corresponding to the chosen geometry and polarization, commonly using the tensor notation expressed in equation 2.41 [19].

$$n_{ij}(E_0) = n_{ij} + \Delta n_{ij}(E_0) = n_{ij} + \sum_k r_{ijk}E_{0k} + \sum_{k,l} s_{ijkl}E_{0l} + \cdots \ . \qquad 2.41$$

However, equation 2.41 provides a more complete analysis based on the index variation model using an elliptical surface (see for more details) [94, 79]. It can be simplified using equation 2.40, given that the coefficients are already known, where, for materials with this effect, we can isolate the terms that vary linearly as $n_P(E) \approx n - \frac{1}{2}\mathrm{r}n^3E$.

Table 2.5 shows some commonly used materials that employ the Pockels effect, along with their most relevant electro-optic coefficients.

Table 2.5 – Materials and their electro-optical coefficients (Pockel).

Material	Pockel coefficient $\boldsymbol{r}$ [pm/V]	Refractive Index $\boldsymbol{n}$	Reference
$\mathrm{LiNbO_3}$	$\mathrm{r_{33}} \approx 30.9, \mathrm{r_{13}} \approx 9.6$	2.2	[89, 79]
$\mathrm{LiTaO_3}$	$\mathrm{r_{33}} \approx 30.5$	2.123	[90, 79]
$\mathrm{BaTiO_3}$	$\mathrm{r_{33}} \approx 28, \mathrm{r_{51}} \approx 800$	2.383	[79, 91]
GaAs	$\mathrm{r_{42}} \approx 1.2$	3.6	[92]
InP	$\mathrm{r_{42}} \approx 1.5$	3.21	[93]
$\mathrm{PbTaO_3}$	$\mathrm{r_{33}} \approx 5.9$	2.67	[94]
$\mathrm{KNBO_3}$	$\mathrm{r_{33}} \approx 64, \mathrm{r_{13}} \approx 380$	2.10	[93, 94]

As example, for $\mathrm{LiNbO_3}$ in applications such as integrated modulators, the coefficient r_{33} is commonly used, as shown in the Figure 2.15.

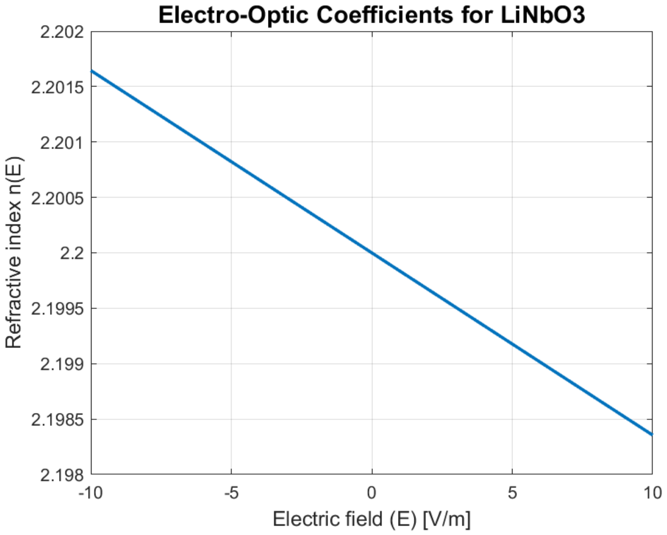

Figure 2.15 – Variation of the refractive index by applied Electric field in $\mathrm{LiNbO_3}$.

As can be seen in Figure 2.15, for the simulation using the parameters in Table 2.5 for lithium niobate, the index n decreases linearly with E. However, the magnitude and exact sign depend on the orientation of the field with respect to the optical axis, the value (and sign) of the electro-optic tensor r_{ij}, and the type of light polarization (TE/TM). In current modulators, this configuration is used, reducing n linearly with E for applications such as modulators [95].

2.4.2 Kerr Effect

The Kerr effect, initially documented in 1875 by the Scottish physicist John Kerr [96], is a nonlinear optical phenomenon that manifests when light propagates in crystals and glasses and in other media such as gases. It can be described as a change in refractive index caused by electric fields, and it is proportional to the square of the electric field strength [97], originated in the birefringence induced by the electric field [98]. The introduction of the laser in 1960 marked a significant advancement in optics, providing light sources with sufficient electric field strengths to induce the Kerr effect. This phenomenon, whereby a second laser replaces the applied voltage, is known as the optical Kerr effect. The effect caused by the application of electric fields is given in two ways, which will be discussed below.

Unlike the Pockels effect, which occurs in non-centrosymmetric materials, that is, in materials that lack an inversion center in their crystal structure, the Kerr effect can happen in a wide variety of materials, such as centrosymmetric and non-centrosymmetric crystals, as shown in Figure 2.13, and includes some semiconductors, liquids, and optical polymers. As we analyzed previously in equation 2.40, we can define for materials that respond to the Kerr effect, isolating the quadratic term, that we have, $n_K(E) \approx n - \frac{1}{2}sn^3E^2$, as mentioned above, the Kerr effect manifests itself through its quadratic variation (quadratic electro-optic), as we have discussed previously, or when applied in the optical case (nonlinear optics), a source of light intensity I . The relationship between the intensity of light (source) in a dielectric medium with a refractive index is expressed as [99],

$$I = \frac{1}{2} c\varepsilon_0 n E^2 \ . \qquad 2.42$$

This term describes the electro-optical Kerr effect, where the index changes due to light intensity, as in the use of a laser with high power. Arises from the optical-frequency Kerr effect (sometimes called the alternate current (AC) Kerr effect), and it is the origin of the intensity-dependent refractive index, a process in which a beam of light changes its own refractive index, which is determined by,

$$n_K(I) \ \approx n - \frac{sn^2}{c\varepsilon_0} I \ , \qquad 2.43$$

this effect produces a nonlinear response instantaneously; the incident light wave creates a nonlinear polarization wave that acts back on it by changing the refractive index.

As mentioned above, when spatial inversion is present, the Kerr effect is allowed in all materials, but occurs in centrosymmetric materials (gases, liquids, glasses). In the isotropic case for glasses and liquids, rotational symmetry reduces the s_{ijkl} tensor to a

few invariant combinations, since having symmetry $r_{ijk}(E) = r_{ijk}(-E)$ eliminates the odd terms in E (linear term).
With this reduction, the observable effect can be summarized as a single constant expressed in terms of the tensor for third-order nonlinear optics as $n_2^e = \left(3\chi^{(3)}/8n_0\right)$, where n_2^e is the electric Kerr coefficient (nonlinear refractive index) and the refractive index change as,

$$n = n_0 + n_2^e E^2 = n_0 + \Delta n_K(E)\,, \qquad 2.44$$

in some bibliographies, when we look for the parameters for the Kerr effect, they are given in terms of the tensor, while in others, they are given in terms of the constant K that appears in the induced birefringence, indicated as [100],

$$\Delta n_K(E) = \lambda K E^2. \qquad 2.45$$

Given the tensor values as constants, we can calculate analytically based on the expressions in both cases. For the case of intensity I, using the relationship defined in equation 2.42, the expression of the electric field is defined as $E^2 = 2I/c\varepsilon_0 n_0$, where, by substituting this equality into 2.44, we obtain the variation of the refractive index for intensity as [101],

$$n = n_0 + n_2 I \;, = n_0 + \Delta n_K(I)\,, \qquad 2.46$$

where n_2 is the optical Kerr coefficient defined as, $n_2 = 2n_2^e/c\varepsilon_0 n$, express in $[\mathrm{m^2W^{-1}}]$. Therefore, the refractive index varies linearly with intensity through its optical Kerr constant, and the phase shift of the light for both forms of the Kerr effect, for the propagation distance L (length of the phase shifter) is determined by [102, 7],

$$\Delta\phi = \frac{2\pi L}{\lambda}\Delta n = 2\pi L K E^2 = \frac{2\pi L}{\lambda} n_2 I = \frac{2\pi L}{\lambda S} n_2 P\,, \qquad 2.47$$

where using the power–intensity relation in a guided mode, $I = P/A_{eff}$, for P as the power of the incident light and A_{eff} as the effective modal area [102], expressing the phase shift in terms of power, which is a more practical approximation in waveguides.

Table 2.6 shows the values of the Kerr coefficients mentioned above for some commonly used materials.

Table 2.6 – Materials and their electro-optical coefficients (Kerr).

Material	n	$\chi^{(2)}$ [m²/V²]	n_2[m²/W⁻¹]	K[m/V⁻²]	Reference
Si	3.4	2.08e-18	2.7e-18		[103]
Ge	4	5.60e-19	9.9e-18		[103]
GaAs	3.47	1.40e-18	3.3e-17		[103]
GaP	3.047	3.01e-20			[92]
ITO	0.489	450e-20			[92]
C_6H_5NO2	1.524			3.0e-12	[100, p. 485]
PLZT	2.40			2.7e-19	[104]
Zn	1.04	6.3e-11			[105]
Al_2O_3	1.8	3.1e-22	2.9e-20		[106]
LiF	1.4	6.2e-23	9.0e-21		[106]

Consequently, as previously discussed, the change in phase of the light is proportional to its power, when light propagates through a nonlinear medium, the refractive index change modulates the phase of the optical wave, resulting in a phase shift of the pulse itself [19]. The phase change quantity is proportional to the refractive index change quantity. According to the different phase modulation methods, the optical Kerr effect can produce two phenomena known as Self-Phase Modulation (SPM) and Cross-Phase Modulation (CPM) [102]. In Figure 2.16, using the Si values obtained from Table 2.6, the values for the Kerr Electro-optic Effect (DC Kerr Effect) and the Optical Kerr Effect (AC Kerr Effect) were plotted. This analysis is available in the GitHub repository named "*Kerr-Effect,*" available on [107],

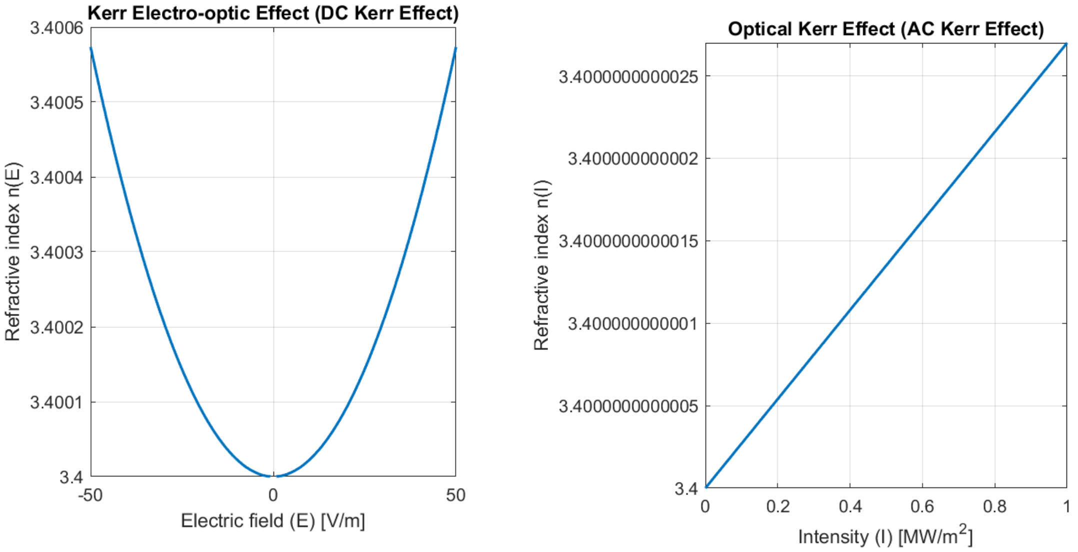

a) b)

Figure 2.16 – Representation of the electro-optic effect, a) Kerr Electro-optic Effect (DC Kerr Effect), b) Optical Kerr Effect (AC Kerr Effect).

If the electric field is obtained by applying a voltage V across two faces of the cell, separated by a distance d, then $E = V/d$, under these considerations, equation 2.46 can be expressed as,

$$\Delta\phi = \frac{2\pi L}{\lambda}\Delta n = 2\pi LKE^2 = 2\pi LK\,(V/d)^2\ , \qquad 2.48$$

for a phase shift in π, $\Delta\phi_\pi$, $V_\pi = V_{\lambda/2}$, and define as,

$$V_\pi = \frac{d}{\sqrt{2LK}}\ . \qquad 2.49$$

The Kerr electro-optic effect generally yields smaller index changes than the Pockels effect; the former scales with the square of the applied field, the latter with its first power. As one of its applications, the Kerr effect is used to implement fast optical modulators in birefringent optical fibers, in other words, the orthogonally polarized components of each wave propagate with different propagation constants due to a slight difference in their effective mode indices [108]. In cases of fiber optic applications, this effect makes it possible to change the polarization of an optical signal by inducing a change in the birefringence of the fiber core through an intense optical pumping pulse [109].

2.5 Principles of Free Carrier Effects

The free carrier effect, also known as the free carrier plasma dispersion effect, refers to the dependence of optical properties (both refraction and optical absorption) on the concentration of free carriers; this effect appears nominally in semiconductors and semimetals. Changes in the concentration of free carriers affect the optical absorption of the material, but also inevitably alter its dielectric properties, as dictated by the fundamental Kramers-Kronig relation [73]. By manipulating the carrier density in a medium by applying current through it, for example, in a p-n type structure, changes occur due to variations in the free carrier density (electrons and holes), which leads to control of the refractive index change. This technique has been widely implemented in all-optical modulators and switches [110], although increasing the free carrier density (n-p) increases absorption due to the plasma dispersion effect, which is related to the plasma frequency (ω_p) as described in the following equation [7],

$$\omega_p^2 = \frac{n_e e^2}{\epsilon_0 m_e}, \qquad 2.50$$

where ω_p represent the angular plasma frequency, indicating how conduction electrons respond to oscillating fields, n_e is the electron density (number of electrons per unit volume), e is the elemental charge (electron charge), ϵ_0 is the permittivity of vacuum, previously viewed and m_e is the mass of the electron.

The plasma frequency is directly dependent on the free carrier density n_e, and in turn, the complex dielectric permittivity is related to the plasma frequency by [111],

$$\varepsilon_r(\omega) = 1 - \frac{\omega_p^2}{(\omega^2 + i\omega\gamma)}, \qquad 2.51$$

were γ is the collision frequency, which is equal to the inverse of the relaxation time $\gamma = \tau^{-1}$. These relationships prove that any induced variation in free-carrier density n_e, modifies the complex refractive index $n' = n + i\kappa = \sqrt{\varepsilon_r}$, where the real part sets the phase velocity as $v_p = c/n$, and the imaginary part sets the absorption defined above in equation 2.11. Thus, based on the relationships defined above, it can be confirmed that the refractive index and absorption can be dynamically controlled by electrically modulating the free-carrier density n_e.

As an extension of the Drude model to a specific wavelength [112], we have the plasma dispersion effect and the absorption of free carriers. These are estimated by the concentrations of dopants in semiconductors using the following equations [113, 114, 115],

$$\Delta n = -\left(\frac{e^2\lambda^2}{8\pi^2 c^2 \varepsilon_0 n}\right)\left[\frac{\Delta \mathrm{N}_e}{m_{ce}^*} + \frac{\Delta \mathrm{N}_h}{m_{ch}^*}\right], \qquad 2.52$$

$$\Delta \alpha = \left(\frac{e^3\lambda^2}{4\pi^2 c^3 \varepsilon_0 n}\right)\left[\frac{\Delta \mathrm{N}_e}{{m_{ce}^*}^2 \mu_e} + \frac{\Delta \mathrm{N}_h}{{m_{ch}^*}^2 \mu_h}\right], \qquad 2.53$$

in the above equations, as a new representation of variables, we have that, m_{ce}^*, m_{ch}^* are the conductivity effective masses of electrons and holes, respectively. In addition, μ_e, μ_h have been defined as the mobilities of electrons and holes, respectively. $\Delta\mathrm{N}$ represents the variation in the levels of majority carriers e (electrons) and h (holes).

For crystalline silicon (Si) at a probe wavelength of 1.55 μm, Soref and Bennett [116] derived empirical formulas for the changes in the refractive index and absorption coefficient as functions of electron and hole concentrations, $\Delta\mathrm{N}_e$ (cm^3) and $\Delta\mathrm{N}_h$ (cm^3), respectively. These formulas were derived from experimental results [116, 117] and are presented in the following equations as,

$$\Delta n = -[8.8 \times 10^{-22} \times \Delta \mathrm{N}_e + 8.5 \times 10^{-18} \times (\Delta \mathrm{N}_h)^{0.8}] , \quad 2.54$$

$$\Delta \alpha = 8.5 \times 10^{-18} \times \Delta \mathrm{N}_e + 6.0 \times 10^{-18} \times \Delta \mathrm{N}_h . \quad 2.55$$

And under similar conditions for 1.3 µm, the following results were obtained [118],

$$\Delta n = -[6.2 \times 10^{-22} \times \Delta \mathrm{N}_e + 6.0 \times 10^{-18} \times (\Delta \mathrm{N}_h)^{0.8}] , \quad 2.56$$

$$\Delta \alpha = 6.0 \times 10^{-18} \times \Delta \mathrm{N}_e + 4.0 \times 10^{-18} \times \Delta \mathrm{N}_h . \quad 2.57$$

The Drude model describes the changes in the refractive index and absorption coefficient [112] that occur because of a change in the free carriers' plasma frequency, which depends not only on the number of free carriers but also on their effective conductivity masses. According to the model, the contribution of free carriers to the index is stronger the smaller their effective mass is therefore, materials or carrier types with lower masses offer greater index sensitivity [113]. Changes in absorption can have a strong effect on the refractive index for wavelengths close to the absorption limit, due to the Kramers-Kronig relation [119]; which imposes a coupling between the imaginary (absorption) and real (dispersion) parts of the optical response by causality, where it is explained that if the absorption varies near a spectral edge, the index will have a pronounced dispersive variation in that vicinity.

2.5.1 MOS Capacitor

We will briefly analyze the Metal-Oxide-Semiconductor (MOS) structure or also known as MOS capacitor, this is a device formed by a doped silicon substrate together with a thin layer of silicon dioxide SiO_2 and a metal (electrode) such as Au, W, Ti, among others, although in practice poly-S polysilicon is also widely used, which is also used as structural material for integrated sensor devices, such as pressure sensors, accelerometers and gyroscopes [120]. The structure is comparable to a classical parallel plate condenser, where one of these plates is replaced by the semiconducting Si layer of the substrate, as shown in Figure 2.17.

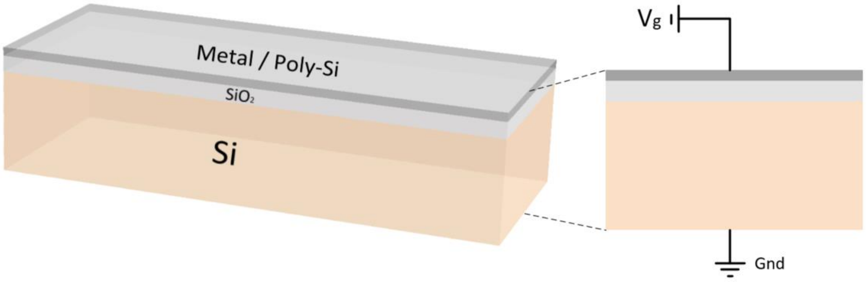

Figure 2.17 – Representation of Basic MOS structure base in Si.

To use the modulation effect of Free-Carrier Plasma Dispersion Effect (FCPDE) in a MOS structure, the Si substrate is usually doped in two ways, type-p creating a high concentration of holes (positive carriers) or type-n creating a high concentration of electrons (negative carriers), in this way when applying a voltage on the gate (V_g), the carriers are redistributed depending on the applied polarization and the type of doping that the substrate has. This movement of carriers is generated by the electric field Ex and its polarization generates inversion, depletion, and accumulation mode of operation. Figure 2.18 shows these three modes and the associated charge distributions.

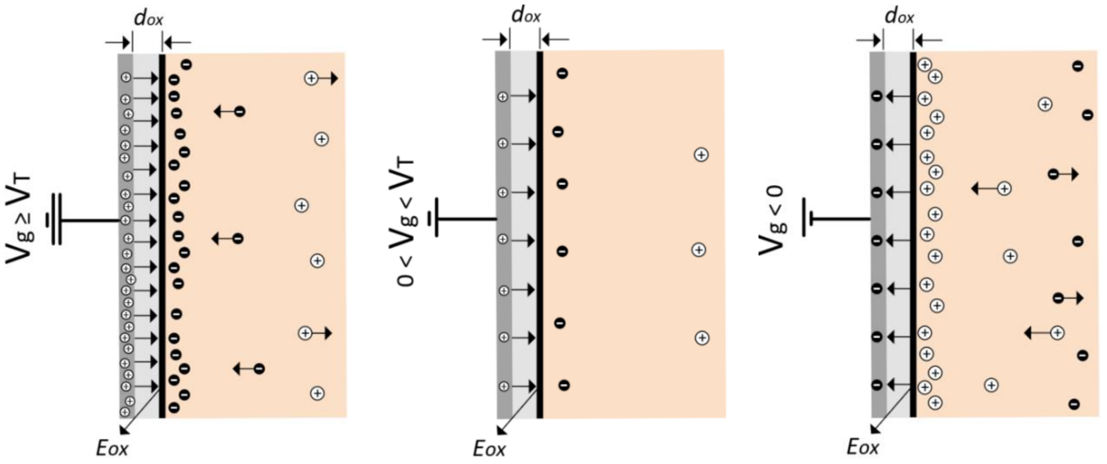

a) b) c)

Figure 2.18 – Charges on a MOS structure (p-type substrate) under a) inversion, b) depletion, and c) accumulation conditions.

In the inversion mode, as show in the Figure 2.18 a) the potential at the voltage threshold (V_T) is increased which generates an increase of the positive charge at the gate, the electric field increases in proportion, so another kind of negative charge arises at the oxide-semiconductor interface these electrons, generated by thermal excitation at a given time or injected from n regions, form a thin but dense inversion layer. At this point, the Fermi level approaches the conduction band E_c in [121],

$$\mathrm{n} = N_c e^{\frac{E_f - E_c}{kT}} \ , \qquad 2.58$$

where N_c are the effective densities of states in the conduction band. Under these conditions, the increase in V_T no longer significantly increases the width W of the depletion region, but rather increases the inversion layer density, as the electric field lines end at the new electrons rather than at more acceptors. Once a strong inversion occurs, the width of the surface depletion layer reaches a maximum. A minimal increase in the width of the depletion layer produces a significant increase in the charge Q_n in the inversion layer. Therefore, under strong inversion conditions, the charge per unit area Q_s in the semiconductor are represented by [122],

$$Q_s = Q_n - Q_{dep} = Q_n - qN_A W_m \ , \qquad 2.59$$

where Q_{dep} is the depletion charge, associated with the fixed negative charge of ionized acceptors A^{-} within the depletion region. Here N_A is the acceptor concentration and W_m is the maximum width of the surface depletion region.

In the depletion stage, as shown in Figure 2.18 b), by changing the gate voltage where $0 < V_g < V_T$, the positive and negative carriers begin to recombine in the doped semiconductor. When the gate is positively charged, holes are driven out of the channel under it, uncovering the fixed negative acceptors. Now the electric field points the other way and goes from the positive charge on the gate, ending at the negative acceptor charge inside the silicon, extending the electric field up to the semiconductor, the depletion field W can be calculated as [123],

$$W = \sqrt{\frac{2\varepsilon_s \cdot \phi_s}{qN_A}} \ , \qquad 2.60$$

where ϕ_s is the surface potential, N_A is the acceptor concentration, q is the elementary charge, and ε_s is the permittivity of silicon. As can be seen in Figure 2.19 b), in this mode the metal surface acquires a charge $Q_m > 0$, in turn inducing a negative charge $Qs < 0$ on the semiconductor that comes from the ionized acceptor ions as the holes are ejected from the interface, under these parameters the depletion region occurs, and the charge depends on the surface potential and doping level N_A of the semiconductor, this is determined by the following expression,

$$Q_s = -qN_AW \ , \qquad 2.61$$

In the band diagram, a downward curvature of E_C, E_i, E_V is seen, increasing the energy $q\psi_B$ of the $E_i - E_F$ difference, which reduces the gap density. The total charge stored in the semiconductor depends on Vg, but the system does not conduct lateral current. In this mode, a region without mobile carriers appears, with only fixed negative charges near the substrate.

In the accumulation stage as referred in Figure 2.18.c), the substrate is doped with positive carriers, which makes that when we apply a negative gate potential $V_g < 0$, the holes will be attracted by the negative charge applied towards the substrate surface, it is known that the hole density is exponentially proportional to how close the Fermi level is to the valence band edge E_v [123]. In the Figure 2.19 c) we can see the energy band diagrams and charge distributions, as mentioned above when applying a potential $V_g < 0$, a negative charge is generated on the metal surface $Q_m < 0$, in turn inducing a positive charge $Q_s > 0$ on the semiconductor. This carrier distribution is reflected in the increasing splitting of the energy band of the intrinsic Fermi level E_i above the Fermi level E_F, in this mode increases the probability of occupation of the positive charge state given by [121],

$$p = N_v e^{\frac{E_v - E_f}{kT}} \ , \qquad 2.62$$

where N_v are the effective densities of states in the valence band. They represent in a sense the number of useful states, at temperature T, in their respective energy band.

Consequently, the mobile carrier density increases, increasing the surface conductivity, the accumulated charge is related to the applied voltage through the capacitance generated in $\mathrm{SiO_2}$ as,

$$Q_s = C_{d_{ox}} \cdot Vg \ . \qquad 2.63$$

At this stage, the charges are stored on the substrate at the $\mathrm{SiO_2}$ interface, so an increase in voids is seen near this boundary.

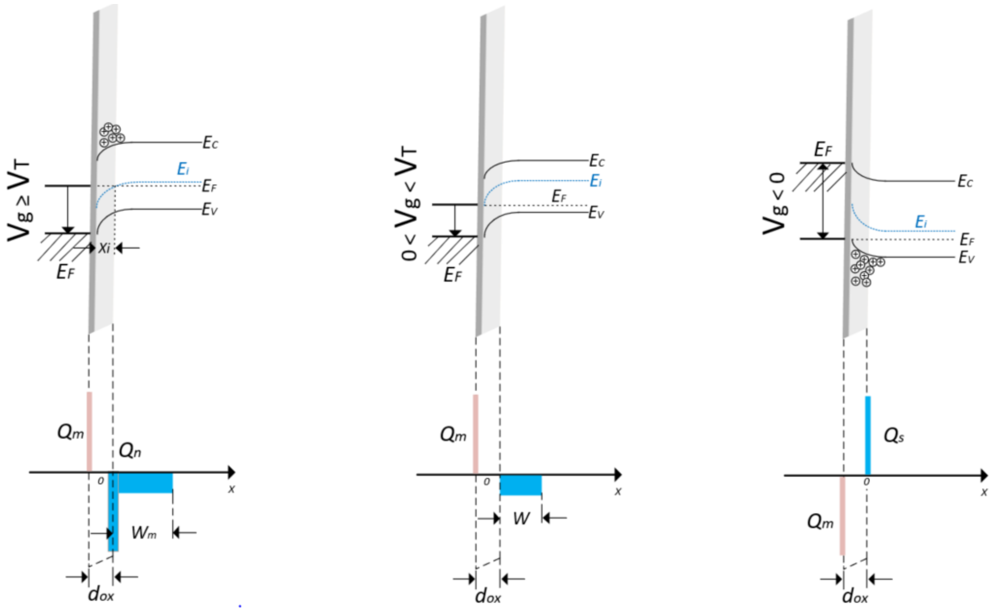

a) b) c)

Figure 2.19 – Energy band diagrams and charge distributions of an idea MOS structure (p-type substrate) under a) inversion, b) depletion and c) accumulation conditions.

As shows in the Figure 2.20 the diagram of a sketch of the C-V curves of an ideal MOS capacitor, with p-type substrate, the voltage determines the modes of operation as seen above, also seen in the Figure two voltages that delimit the three regimes are (a) the Flat Band Voltage (VFB), which separates the accumulation regime from the depletion regimes and (b) the threshold voltage (V_T), which separates the depletion regime from the depletion regime [124].

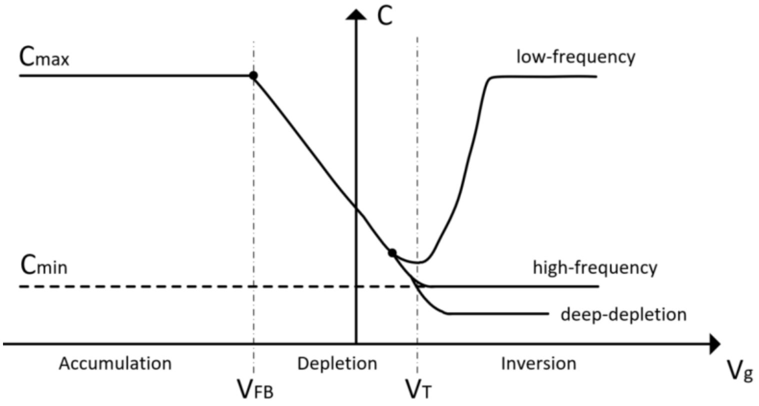

Figure 2.20 – Sketch of a C-V curve of an ideal MOS capacitor with a p-type substrate.

2.5.2 Basic Architecture of Silicon Modulators Based on Free-Carrier Plasma Dispersion Effect (FCPDE)

Using the concepts analyzed above for a basic MOS structure in silicon for p-type doping, we observed how varying the gate voltage (V_g) allows us to control the three fundamental modes of operation (inversion, depletion, and accumulation) by controlling the potential applied to the gate. The level of doping and the control of free carrier movement have key applications in photonics, mainly in silicon photonics on SOI/CMOS substrates. This free carrier movement is analyzed within the Free-Carrier Plasma Dispersion Effect (FCPDE), referred to above in equations 2.51 and 2.52. Within the family of mechanisms that make up the FCPDE, we have (i) Carrier Injection Phenomenon (CIP), (ii) Carrier Depletion Phenomenon (CDP), (iii) Carrier Accumulation Phenomenon (CAP). Together, each of these mechanisms changes the local carrier density along with the guided mode, changing the effective index and absorption. The MOS model defines the electrical configuration based in semiconductor models, while the FCPDE defines the optical response that we will use for our applications.

The implementation of MOS structures in waveguides allows the creation of more complex structures directly on SOI as photonic modulators [125, 126, 127], switching devices [115], memory devices [128, 129], sensing applications [130, 131, 132], tuning of optical devices and integration with photonic devices. Beyond their traditional uses, MOS-capacitor structures are the basis of many silicon electro-optic modulators: a gate bias changes the local refractive index, enabling modulation of optical signals [133].

MOS-capacitor structures underpin many silicon electro-optic modulators, often in Mach–Zehnder interferometers (MZI) [126] where an applied gate bias tunes the local refractive index and, with it, the optical signal. These Electro-Optic Modulators (EOMs) are foundational in high-speed fiber-optic links and on-chip interconnects, enabling multi-tens-of-gigabit data rates [134]. They are also used in active sensing platforms in Light Detection and Ranging (LiDAR) [134] in autonomous vehicles and robotics, where fast and precise phase or amplitude control is required.

In biomedical imaging, enhancing the resolution and sensitivity of optical microscopy for early disease detection and diagnosis is significant. Optical sensing [134] enabling the detection of light intensity changes for environmental monitoring, chemical sensing, and industrial process control is also useful. Finally, in the realms of quantum computing and quantum networking, such devices have the potential to accelerate integrated quantum-technology platforms and protocols [134, 135].

In Silicon MOS-based platforms, for analyzing the efficiency of devices mainly in applications such as modulators, the Figure of merit (FOM) is widely used, which is the ratio of the applied voltage to obtain a phase shift π, this is universally identified as V_π. After an extensive review focused on optical modulators, several approaches to this relationship are seen, among them, in a general way, it is established that $V_\pi \cdot L_\pi$. In the case of Si, MOS modulators, when subjected to a bias voltage (V_g), the product $V_\pi \cdot L_\pi$ varies non-linearly due to the non-linear change in the refractive index of silicon [136], in this case the efficiency is given by,

$$\Delta\phi_\pi = V_\pi \cdot L_\pi = \frac{\lambda}{2S_p} \qquad 2.64$$

where L_π is the length of the electrode and S_p is the modulation sensitivity, defined as the effective mode index change versus applied voltage, defined as, $S_p = \partial n_{eff}/\partial V_g$ [136, 137]. In practical terms, a more complete and simple way of formulating efficiency is to consider the losses, we have that [138, 137],

$$\Delta\phi_\pi = V_\pi \cdot L_\pi \cdot \alpha \qquad 2.65$$

where α is the loss per unit length (in dB/mm), this equation simultaneously considers the voltage, the length of the electrode and the optical losses, allowing an objective comparison between different modulation technologies.

2.5.2.1 Silicon Modulators Based on Carrier Injection Phenomenon (CIP)

In the earlier section, an analysis was made of the main characteristics of the MOS capacitor and its modes of operation, including inversion, depletion, and accumulation. At this point it is possible to provide a direct analogy with the mechanisms used in silicon-based optical modulators. The three modulation schemes used are based on the principle of the free-carrier effect and are known as carrier injection, carrier depletion and carrier accumulation. [139]. These configurations are also known as Silicon Insulator Silicon CAPacitor (SISCAP), which is nothing more than silicon photonic modulators based on a MOS capacitor structure.

One of the most widely implemented approaches in silicon-integrated photonics is the use of modulators based on carrier injections in an MZI. This architecture consists of the active introduction of electrons and holes into an intrinsic region by means of p–n or p–i–n junctions, as shown in Figure 2.21 [118, 125]. When applying a forward bias through the electrodes connected to the most highly doped regions p++ and n++, a movement of majority carriers (holes from the p-region and electrons from the n-region) towards the intrinsic region into the path of the propagating light or waveguide is generated, this stimulated movement of free carriers is known as injection. Then, the recombination of these carriers and their accumulated effect change the refractive index and the absorption coefficient using the same principles analyzed above.

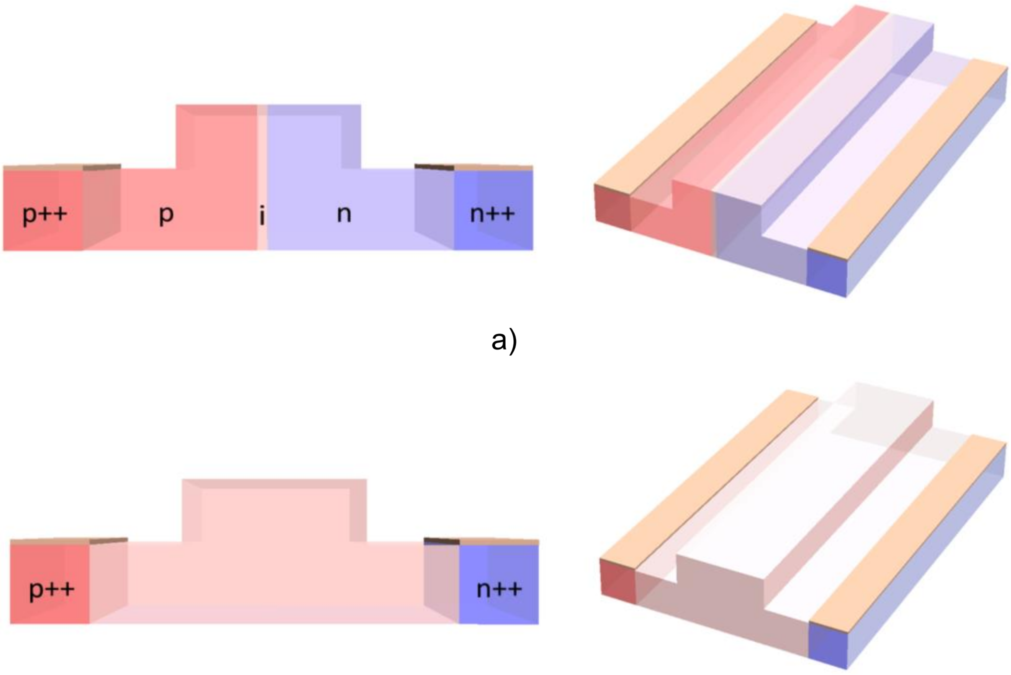

a)

b)

Figure 2.21 – Carrier injection-based Si modulators, a) the structure has a highly doped p++–p–i–n–n++ configuration and is used for the efficient injection of charge carriers, b) with the configuration p++–i–n++ under forward bias, electrons and holes are injected into the intrinsic region, enabling modulation of the optical signal.

Optical modulators based on this architecture offer high modulation efficiency due to the significant overlap between the intrinsic region and the optical mode of the waveguide, allowing effective modulation with relatively low voltages, approximately 1.5V [140]. These devices have an inherent limitation in their modulation bandwidth, generally on the order of MHz units. This disadvantage is caused by the slow diffusion of free electrons in the doping zone, which can take several nanoseconds to diffuse over short distances (in the order of micrometers) [141, 142], the lifetime of the minority carriers [115, 139], and the temporal delay associated with resistive and capacitive effects of the structure (RC delay) [143]. As a result, the maximum speed recorded in these devices to date is a few Gbit/s [139].

To mitigate this limitation in response speed, techniques such as signal pre-emphasis in the driver circuits have been implemented [138]. By applying the pre-emphasis pulse technique to this same structure, in [43] with pin junction, where the modulation speed reaches of 1.5 Gbit/s to 12.5 Gbit/s [144]. However, the use of pre-emphasis techniques makes the modulator driver design complex and expensive [136]. One of the practical solutions is to incorporate a high-pass filter in the electronic drive circuit. Using this technique in [140], the modulator's response was improved to a first cut-off frequency of less than 1 GHz at 5 GHz.

Furthermore, the use of electrical signaling schemes with pre-emphasis, where a fraction of the electrical controller signal has a voltage significantly higher than $\gg V_\pi$ of the modulator, improves the limited speeds of carrier injection modulators, although with the drawback of higher energy consumption. In recent years, passive equalization techniques have been developed to enhance the high-speed operation of carrier injection modulators. Studies have shown that the factors limiting the speed of carrier injection-based modulation are (a) the recombination time of the injected electron-hole pairs and (b) the sum of the output resistance of the electric exciter and the overall resistance of the p- and n-doped regions [125].

2.5.2.2 Silicon Modulators Based on Carrier Depletion Phenomenon (CDP)

Optical modulators based on the carrier depletion mechanism are typically implemented by a reverse-biased p–n junction as shown in Figure 2.22. Under this condition, a spatial charge region (depletion region) is generated that removes free carriers from the waveguide, thus modifying the refractive index through the plasma dispersion effect [136]. The expansion of the depletion zone introduces a change in the refractive index and then, a phase variation of the guided mode. This effect is intrinsically high-speed because it is a unipolar effect, meaning it has only one carrier [145]. The manufacturing process of the depletion-type modulator is also advantageous in terms of ease of fabrication, low optical loss [145] and high-speed performance [146], the latter being based on the dynamics of majority carriers induced by the electric field. This approach allows remarkably high modulation speeds (up to 90 Gbit/s) because it avoids the limitation imposed by the half-life of minority carriers [139].

Although it has been established that depletion devices can achieve modulation rates higher than 30 GHz in practical applications [118], they have lower modulation efficiency compared to carrier injection and accumulation techniques [139], which requires the phase shifter length to be greater than 1 mm (typically $V_\pi \cdot L_\pi = 1.5 - 2.5\ \mathrm{V \cdot cm}$ and higher power consumption [147, 139]. The low overlap between the depletion region and the guided optical mode, as well as a limited capacitance (0.2–0.8 pF/mm), restricts the total efficiency of the device [125]. One of the techniques used to increase modulation efficiency is to increase capacitance. This can be achieved by reducing the size of the main mode, which is determined by the geometry of the waveguide, or by reducing the width of the depletion region (higher transition capacitance) [125].

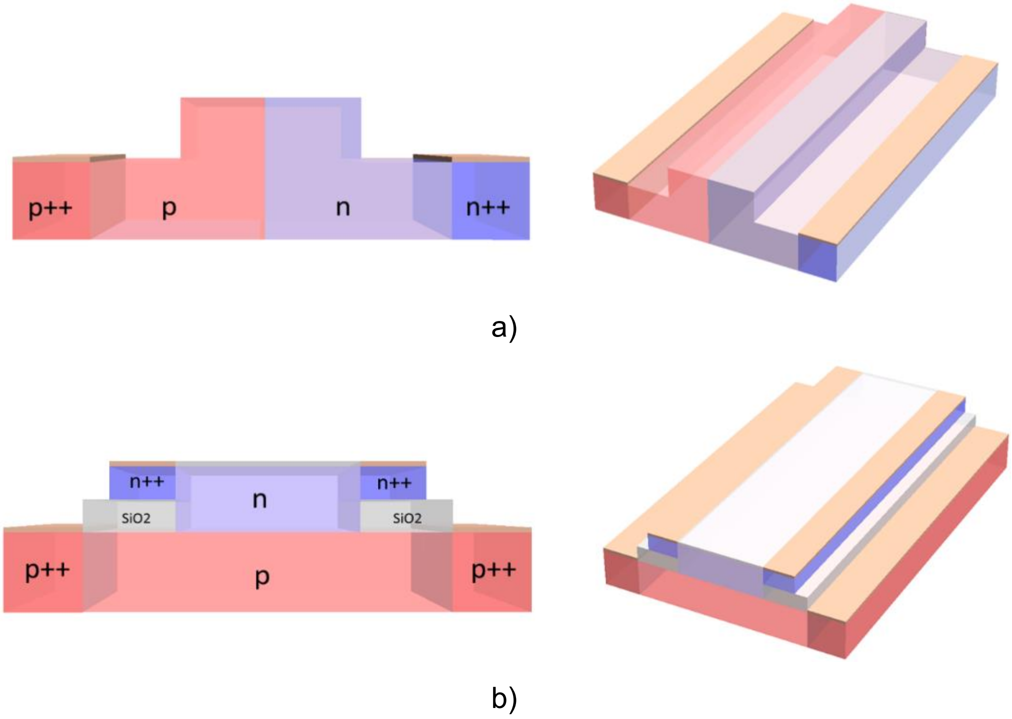

Figure 2.22 – Carrier depletion-based Si modulators, a) typical design with lateral p–n junction in a silicon waveguide, b) variant with vertical junction p-n, which maximizes the overlap between the depletion region and the optical mode.

A lot of efforts are directed to improve its modulation efficiency, such as increasing free-carrier densities of the p-n junction, it results in high optical loss due to free carrier absorption [115], utilizations of ring resonators [118], or enhancing the overlap between the optical mode and the depletion region by interleaved p-n junctions perpendicular to the light propagation direction [148].

Although this type of modulator has its advantages, it is still not enough for future technological projections that demand more and more processing capacity, current research is focused on optimizing active mode-region superposition and increasing effective capacitance without compromising optical performance, through solutions such as the use of resonators, more advanced geometries, or interdigitated structures [125, 145], to maintain a balance between efficiency, speed, and optical losses.

2.5.2.3 Silicon Modulators Based on Carrier Accumulation Phenomenon (CAP)

Optical modulators based on the carrier accumulation mechanism exhibit an operating principle analogous to the MOS capacitor, illustrated in Figure 2.18 c). And their charge is defined by equation 2.62, where the accumulation capacity manifests itself predominantly in the region of the thin oxide layer on the substrate, defined by [139],

$$C_{d_{ox}} = \frac{\varepsilon_{ox} \cdot h_{ox} \cdot L}{t_{ox}} \ , \qquad 2.66$$

where ε_{ox} is the oxide permittivity (SiO_2), L is the height of the active area, represents the length of the modulating zone and t_{ox} is the insulating layer thickness in [139, 149], made recommendations to the design by defining t_{ox} between 6 – 10 nm in order to optimize the efficiency and speed of the modulator, since increasing t_{ox} increases the efficiency, this increase needs to be analyzed since it has drawbacks such as increasing the capacitance and its time constant RC, limiting the bandwidth of the device.

As shown in Figure 2.23 the basic structures of carrier-accumulation optical modulators can be seen. These modulators present a better efficiency compared to modulators based on carrier depletion, reporting values of $V_{\pi} \cdot L_{\pi} \sim 0.16 - 0.2 \ \mathrm{V \cdot cm}$ [125] , reaching modulation speeds up to 40 Gbit/s [150]. This scheme has less free carriers absorption, resulting in devices with low insertion loss (< 1 dB) when compared to the purely Si and Poly-Si traditional capacitive modulator, which has IL in the order of 8 dB [136]. Phase modulation presents a response that linearly approximates the applied voltage, widely used in high-precision analog applications. On the other hand, although purely capacitive modulation designs with similar structures exist, they have significantly lower bandwidths (0.1-4 GHz), or require impractical voltages (> 40 V) to achieve speeds above 25 Gbit/s, which limits their applicability in high-speed optical links [136].

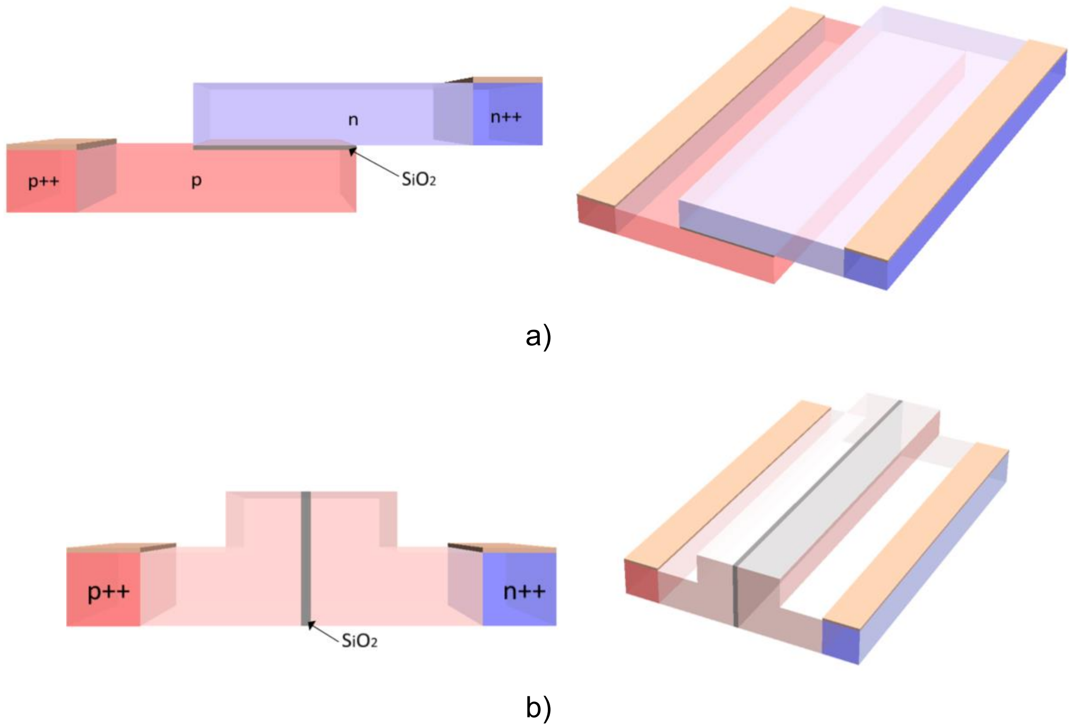

Figure 2.23 – Carrier accumulation-based Si modulators, a) lateral MOS-capacitor design with horizontal oxide interface enabling carrier accumulation along the waveguide, b) vertical slot-based structure with ultra-thin oxide, enhancing field confinement and modulation efficiency.

3 Passive Building Blocks in Integrated Photonics and Simulation Tools.

As mentioned above, PICs are composed of active and passive components. Among the passive components, in this chapter, we will analyze waveguides, which are the medium through which light propagates, and directional couplers, which are elements that, using control techniques (optoelectronic effects), can control the output. With these two elements, it is possible to create simple designs ranging from a 2X2 matrix to more complex ones like dense meshes. Therefore, in this chapter, in addition to analyzing these elements, we will briefly discuss the simulation tools used and some of the methods they employ.

3.1 Waveguides Structure

Waveguides are based on the confinement of light in a medium by extremely compact structures, which is achieved using two media with different refractive indexes. The physical principle that allows this confinement is related to a well-known law of classical optics, Snell's Law, which is the total internal reflection phenomenon that describes this behavior. A waveguide in photonics is basically formed by a core of a high refractive index n_{core}, covered by a cladding of a lower index $n_{clad.}$ Snell's law is explained and analyzed from a ray perspective; in waveguides, it is analyzed and modeled from a wavefield perspective, referring to an electromagnetic wave propagating through the core.

The essential building block of every photonic circuit is a waveguide. Waveguides can be classified by the number of dimensions in which the light is confined. As shown in Figure 3.1 a), a planar waveguide confines the light in one dimension and therefore is a 1D waveguide, since light is not confined laterally, it can escape to the sides. Consequently, it is unsuitable for directing light in defined paths such as curves or loops. As shown in Figure 3.1 b), Channel waveguides (or 2D waveguides) confine the light in two dimensions in this structure, the light is well enclosed, allowing the creation of curves, bifurcations, rings, and other more complex designs, which is the basis of photonic integrated circuits and lasers. It can be used in passive and active devices such as waveguide couplers and modulators. There also exist structures (photonic crystals) that confine light in three dimensions [151].

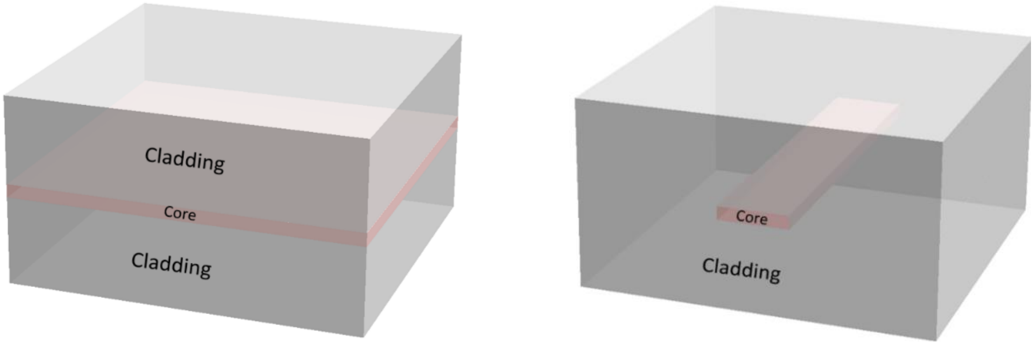

a) b)

Figure 3.1 – Basic structures of waveguides: a) planar waveguides guide light only in the vertical direction, b) channel waveguides guide the light in two dimensions.

In the field of integrated optics, the waveguides most commonly used for design are non-planar with channel geometry to create the optical paths, as shown in Figure 3.2, in this sense, the index profile $n(\mathrm{x}, y)$ manifests itself as a function of the transverse coordinates x and y, thus forming a confinement of a two-dimensional nature. This confinement shows a two-dimensional refractive index profile, allowing tight mode confinement and directional control of light propagation. There are four fundamental groups of non-planar waveguides. These have various parameters for classification, as shown in Figure 3.2.

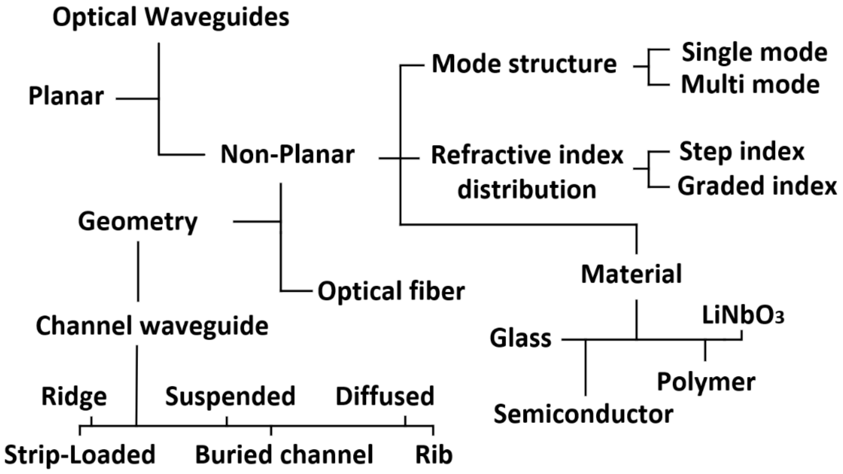

Figure 3.2 – Optical waveguides and their classification. (Adapted from [109]).

This work will only mention channel waveguides in terms of their design. For more details on this topic, please search in [152].

These have various structures, such as underground channels, channels with looped charges, and channels with ridges [117], channels with edging and diffuse channels, as shown in Figure 3.3. Each structure differs in how the index contrast and geometry are engineered, changing mode confinement, fabrication complexity, and coupling efficiency.

In Figure 3.3, we have different channel waveguide configurations, which are also defined in Figure 3.2. As shown in Figure 3.3.a), buried channel waveguide consists of total confinement of the core with a high refractive index covered by a medium with a lower index. This configuration provides excellent optical confinement for $n(\mathrm{x}, \mathrm{y})$ and is characterized by low propagation losses. The core can be designed with any cross-sectional geometry, although for practical purposes it is usually created in a rectangular shape. This configuration is widely used in current photonic circuits and in applications such as interferometers and couplers.

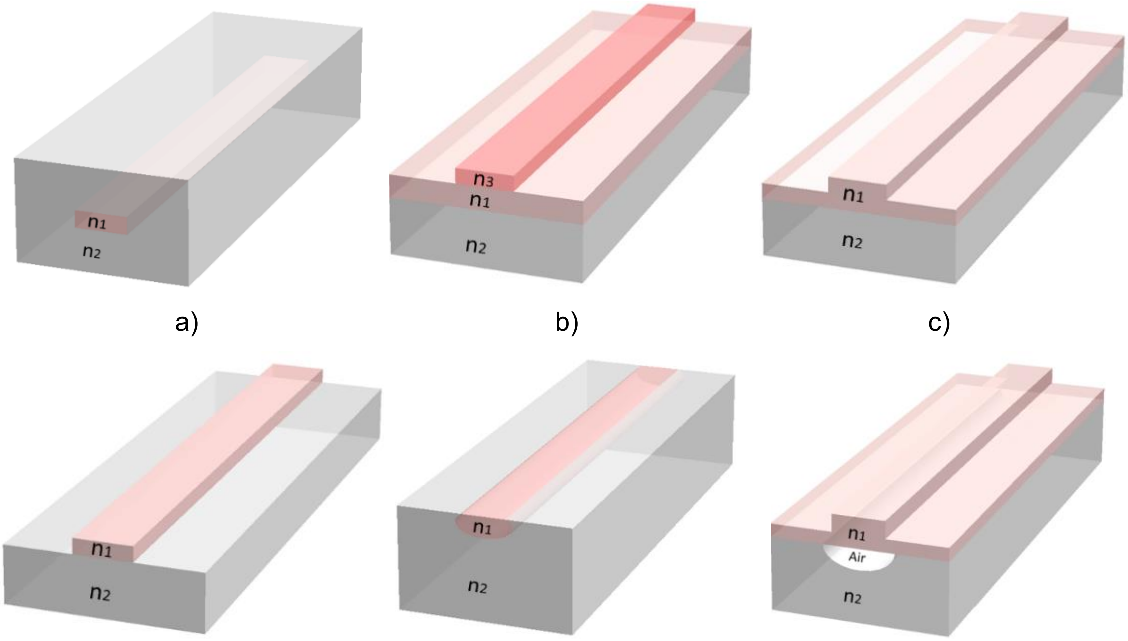

a) b) c)

d) e) f)

Figure 3.3 – Various structures of channel waveguides: a) buried channel waveguide, b) strip-loaded waveguide, c) rib waveguide, d) ridge waveguide, e) diffused waveguide, f) suspended waveguide.

In Figure 3.3 b) the strip-loaded waveguide is formed by loading a planar waveguide with a dielectric or metallic strip, which improves optical confinement in the lateral y direction

[153]. This causes the light to concentrate under the strip, which acts as a lateral guide, since light propagates better through the region with lower loss. The core of this configuration is found by the n_1 region, where $n_1 > n_3 > n_2$. This structure allows for simple manufacturing and is compatible with mass production techniques.

In Figure 3.3 c) rib waveguide consists of an elevated region called a rib made of a layer with a high refractive index layer n_1, leaving a thinner part on its sides called a slab. Lateral confinement occurs because the rib area is thicker than the slab, generating better effective confinement in the main region. However, some of the modes can extend towards the lateral slabs. It has been shown that large-ribbed waveguides can be designed to be single-modal [117], although their design supports hybrid modes (quasi-TE or TM), it is one of the most widely used structures in plasma effect modulators, as previously discussed.

In Figure 3.3 d) ridge waveguide configuration shows a marked similarity to the strip waveguide. In this structure, the ridge is composed of a material with a high refractive index n_1 layer found above the substrate layer. One of the significant advantages of the RIB structure is that the core is more defined. The present study addresses the implementation of a design that ensures improved optical confinement for $n(\mathrm{x}, \mathrm{y})$. This design allows the creation of slight radius curves without significant loss, resulting in reduced coupling with other unwanted modes. These characteristics make it an ideal choice for applications involving the implementation of curves or compact structures, such as MRRs [14], S-bends, and sensor guides.

In Figure 3.3 e), the formation of a diffused waveguide is achieved by creating a high-index region in a substrate through the diffusion of dopants, such as $LiNbO_3$, Zn, Ti, or an ion exchange process, for instance ($Na^+ \leftrightarrow Ag^+$). The diffusion process results in the core boundaries of the substrate becoming indistinct, thereby causing a gradual alteration in the refractive index (i.e., a change from a Gaussian to an exponential profile). A diffused waveguide is characterized by two defining parameters: the thickness, denoted by d, which is decided by the diffusion depth of the dopant in the x direction, and the width, which is defined by the distribution of the dopant in the y direction. This design profile has been shown to reduce modal dispersion, a property which is helpful in the context of optical communications. It has been proven that this profile minimizes losses due to scattering due to the absence of sudden changes in the material.

And finally, in Figure 3.3 f) the suspended waveguide part of the substrate located above or below the center of the waveguide is removed, and the optical core is isolated from the air, which reduces losses due to interaction with the substrate and is especially useful in applications that require interaction with the environment or mechanical handling. The emergence of suspended waveguides has enabled the creation of new types of integrated optical devices, which find applications in fields such as opto-mechanics, nonlinear optics, and electro-optics. The elimination of the substrate layer allows the extension of low-loss SOI operations up to 8 µm [154]. This is highly relevant, as its application in spectroscopy, chemical detection, and sensors is widely exploited [155].

3.2 Effective refractive index

In the analysis and design of integrated photonic circuits, it is essential to know or accurately calculate the effective refractive index (N_{eff}) of waveguides, knowing that the index of the material varies depending on the geometry, which alters the propagation medium for the main modes. Marcatili and Kumar's analytical methods approximate the practical value in rectangular waveguides. These methods are not implemented in more complex algorithms, but they are still an effective way to find the indices quickly and analytically with good approximation. In this paper, we will analyze the Marcatili method for rectangular waveguides.

The Marcatili method is an approximate analytical technique that provides a closed-form solution for rectangular waveguides with a homogeneous core. It decomposes the field into orthogonal transverse regions, solving the wave equations under certain simplifications. It is beneficial because it is a practical implementation that provides approximate values with an acceptable margin of error for a first analysis. However, its accuracy decreases in geometries with high indices or more complex configurations, such as ridge waveguides or asymmetric structures.

In the Marcatili method, the electromagnetic fields and boundary conditions in the highlighted area of Figure 3.4 are not strictly satisfied. In other words, the hybrid modes in rectangular waveguides are analyzed by separating them into two independent waveguides. Kumar et al. proposed an improvement in the accuracy of the Marcatili method by considering the approximation of the contributions of the refractive index in the underlined areas to $\sqrt{2n_0^2 - n_1^2} \approx n_0$ [156].

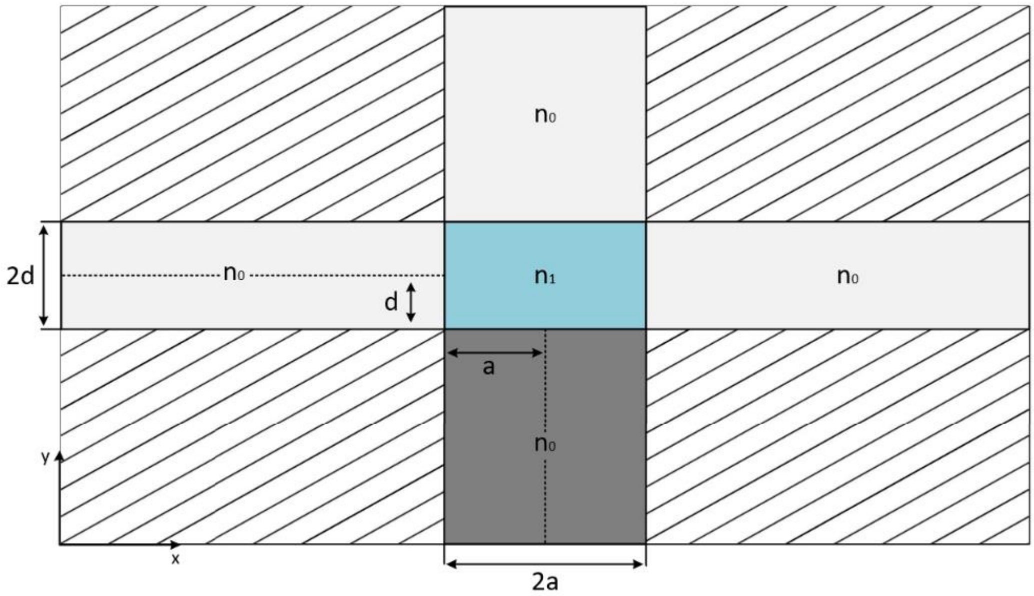

Figure 3.4 – Geometric pattern of Marcatili analysis.

These analytical methods allow us to obtain an approximation of the result. Thanks to today's computing power, more advanced methods are used, such as the Finite Difference Time Domain (FDTD) or the Finite Element Method (FEM), which are used in advanced software such as RSoft Photonic, COMSOL, or Luceda Photonics.

A Python script has been created based on the formulas and analysis described in [156], which aims to approximate the effective refractive index for rectangular waveguides, depending on their dimensions and the desired wavelength. This script allows you to obtain an approximation of the N_{eff} for two materials, Si and a-Si:H. Although it is possible to load more data into the library for more materials, the values for these materials were obtained from the database named Refractive.info, which compiles values from works published in reliable sources, available at [157]. This script allows you to calculate the N_{eff} approximation and the propagation constant and TE/TM guided modes, both fundamental and higher modes. The script is available in the GitHub repository, named "*Marcatili"*, which is available for viewing and downloading at [158]. These values will be helpful for the following analysis, which will deal with the principles of directional couplers.

3.3 Directional coupler

The directional coupler is one of the most essential basic structures in integrated photonics and is the basis of programmable PICs. It is extensively used in all sorts of optical passive/active components, like optical power splitters, optical modulators, wavelength division multiplexers, add-drop multiplexers, micro-ring resonators, and

Mach-Zehnder interferometers. A straight-type directional coupler consists of two adjacent parallel straight waveguides with a slight separation between them [85]. Coupled Mode Theory (CMT) defines how electromagnetic modes propagate and exchange along the longitudinal z-axis due to the fields' superposition by the guide's physical properties and design parameters, such as length, width, height, and angle. Several relevant papers have been published, highlighting the work of Hardy and Streifer in [22], where a generalized formulation of the CMT is proposed, extending the classical orthogonal theory collected by Huang in [159], to the concept of non-orthogonal superposition, introducing terms of "self-coupling" and "cross-power", in addition, the model quantifies the effect of phase mismatch $\Delta\beta$, dispersion, losses, or irregular geometries, are relevant in the performance of modulators and optical switches. These new contributions were collected and analyzed by Chang, Huang, and Wang in [160], where a structured comparison of the main CMT formulations is made, highlighting that each applies to a specific range of conditions, and that the orthogonal formulation is more suitable for identical guides (typically rectangular) and with weak coupling.

The formulation proposed by Hardy and Streifer is more applicable in waveguides with different structures or a substantial overlap of the modal fields. This study determined a better approach for choosing models depending on the coupler design. One of the significant challenges of the earlier models was the precise determination of the coupling coefficient κ, in [161] Kuznetsov determined an analytical expression in rectangular waveguides by analyzing Maxwell's equations. This expression allows for calculation of κ without the need for super-mode simulations.

Several modern books have implemented a more general approach regarding two identical waveguides with rectangular geometry, which has been used in several recent papers. [162, 163] and formally defined and analyzed in [164]. This model expresses the coupling equations for two waveguides with propagation constants β_0 and β_1, with couplings κ_{01} and κ_{10}, considering the losses α, the total electric field of a guided mode in a waveguide is determined by,

$$\vec{E}\ (x,y,z) = A(z)\vec{\mathcal{E}}(x,y)\ , \qquad 3.1$$

where $A(z)$ is a complex amplitude that includes the propagation phase $e^{-i\beta z}$, $\vec{\mathcal{E}}(x,y)$ is the transverse mode profile, normalized to carry unit power. The optical power in each guide is given by,

$$P_0(z) = |A_0(z)|^2 \,, \; P_1(z) = |A_1(z)|^2 \;. \qquad 3.2$$

In the general case, the coupling between modes, the amplitudes evolve according to,

$$\frac{\partial A_0(z)}{\partial z} = -i\beta_0 A_0(z) + \kappa_{01} A_1(z) \;, \qquad 3.3$$

$$\frac{\partial A_1(z)}{\partial z} = -i\beta_1 A_1(z) + \kappa_{10} A_0(z) \;, \qquad 3.4$$

Assuming identical waveguides with loss α, we set,

$$\beta = \beta_r - i\frac{\alpha}{2} \;, \qquad \kappa_{01} = \kappa_{10} = -i\kappa \qquad 3.5$$

where κ is the coupling coefficient, β are the propagation constant and β_r its real part, assume no phase mismatch $\delta = 0$, under these conditions, we express the coupling equations between modes as follows,

$$\frac{\partial A_0(z)}{\partial z} = -i\beta A_0(z) - i\kappa A_1(z) \;, \qquad 3.6$$

$$\frac{\partial A_1(z)}{\partial z} = -i\beta A_1(z) - i\kappa A_0(z) \;, \qquad 3.7$$

the solution to this system can be modeled as a transfer matrix given by,

$$\begin{bmatrix} A_0(z) \\ A_1(z) \end{bmatrix} = \begin{bmatrix} \cos(\kappa z) & -i\sin(\kappa z) \\ -i\sin(\kappa z) & \cos(\kappa z) \end{bmatrix} \begin{bmatrix} A_0(z) \\ A_1(z) \end{bmatrix} \qquad 3.8$$

For condition $A_0(z) = 1$ and $A_1(z) = 0$, the power flow in the guides is given by,

$$P_0(z) = |A_0(z)|^2 = \cos^2(\kappa z)\, e^{-\alpha z} \;, \qquad 3.9$$

$$P_1(z) = |A_1(z)|^2 = \sin^2(\kappa z)\, e^{-\alpha z} \;. \qquad 3.10$$

Describing a sinusoidal power exchange modulated by exponential attenuation due to propagation loss α. The length Lc needed for complete power transfer from one guide to another is given by,

$$L_c = \frac{\pi}{2\kappa} + \frac{m\pi}{\kappa} \ , \tag{3.11}$$

where $m = 0,1,2,. . . .$, in a real guide, with absorption and scattering losses, β is complex. At z=L_c, assuming that the input optical power is P_{in} and that it is initially found in a waveguide $A_0(z) = 1$, the power in each waveguide evolves as follows,

$$P_{0(Through)}(z) = P_{in} \cos^2(\kappa z)\, e^{-\alpha z} \ , \tag{3.12}$$

$$P_{1(Cross)}(z) = P_{in} \sin^2(\kappa z)\, e^{-\alpha z} \ , \tag{3.13}$$

where the coupling coefficient is given by,

$$\kappa = \frac{2h^2 q e^{-qs}}{\beta W(q^2 + h^2)} \ , \tag{3.14}$$

where W is the channel width, s is the separation, in the propagation on the y-axis, we have h and q, as propagation constants and the extinction coefficient, respectively; on the z-axis, we have β as the propagation constants [164].

In photonic modeling and measurement, it is common to define the following power transfer coefficients at the end of the coupler of length L as,

$$t^2 = \frac{P_{(Through)}}{P_{in}} = \cos^2(\kappa L) \ , \tag{3.15}$$

$$c^2 = \frac{P_{(Cross)}}{P_{in}} = \sin^2(\kappa L) \ . \tag{3.16}$$

These equations simplify calculations. For example, by setting a standard parameter such as L, s can vary depending on the desired coupling. A representation of parallel waveguides and various coupling levels for a variation of s is shown in Figure 3.5.

As we have done in earlier analyses, for this analysis, we have created a Python script based on the equations analyzed above, found in a GitHub repository named *CMT_Coupler*, available at [165]. This script has two analysis options: 1) to analyze and graph the coupling parameters for a separation between guides s and a preset length L as shown in Figure 3.6, 2) to perform a sweep with respect to s and show the final power variations for each point of s, L as shown in Figure 3.7.

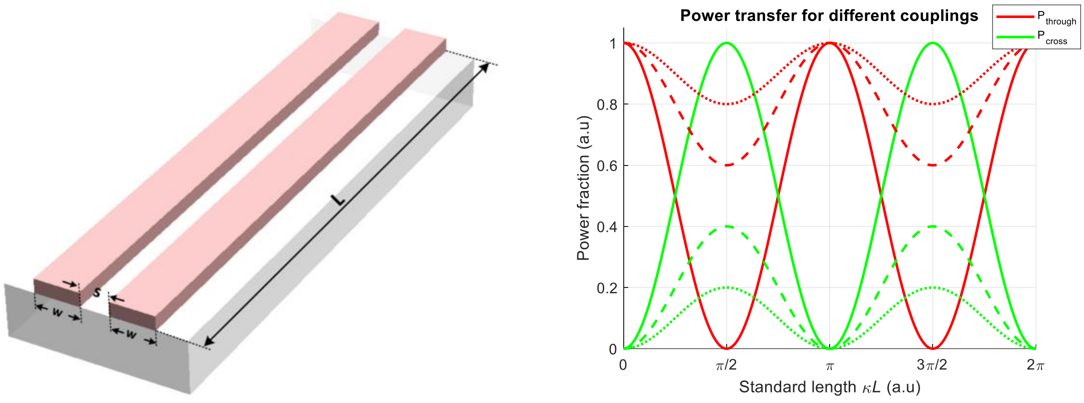

a) b)

Figure 3.5 – Directional coupler: a) two parallel rectangular optical guides with effective length L and separated by a distance s, b) Evolution of the propagation along the z-axis of the transmitted optical power for different values of s.

These two options will allow us to perform an analysis and, in a certain way, improve our design based on s or L. It is important to note that to use this script and, in a certain way, have a more complete tool, we can rely on the Marcatili script to find the effective index and propagation constant requested in this one. In this way, with the two scripts, we have an approximation for our analysis in couplers.

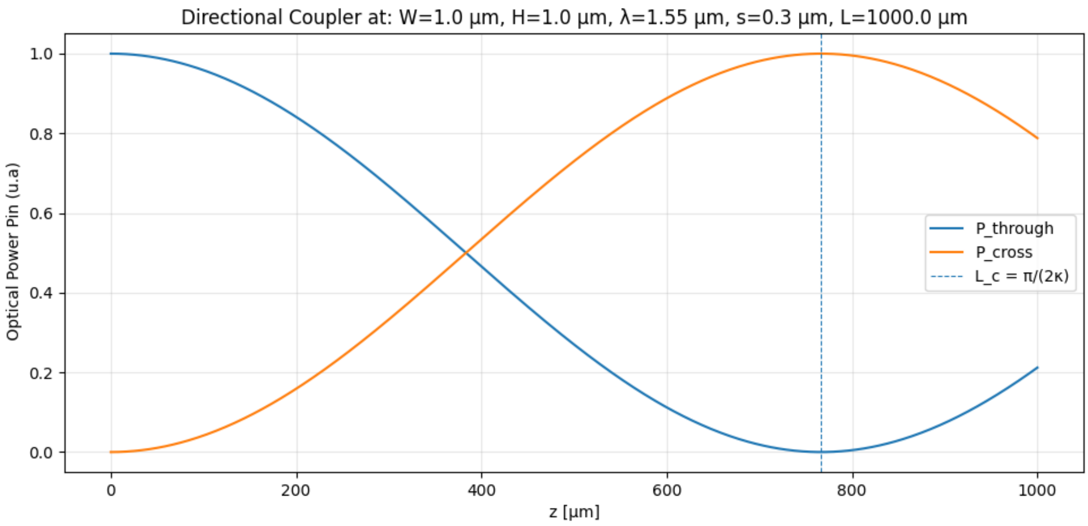

Figure 3.6 – Optical power propagation in a directional coupler for fixed s, L.

As can be seen in Figure 3.7, for a distance $s \geq 0.6\ \mu m$ there is no coupling, confirming what we mentioned earlier in Chapter 1.

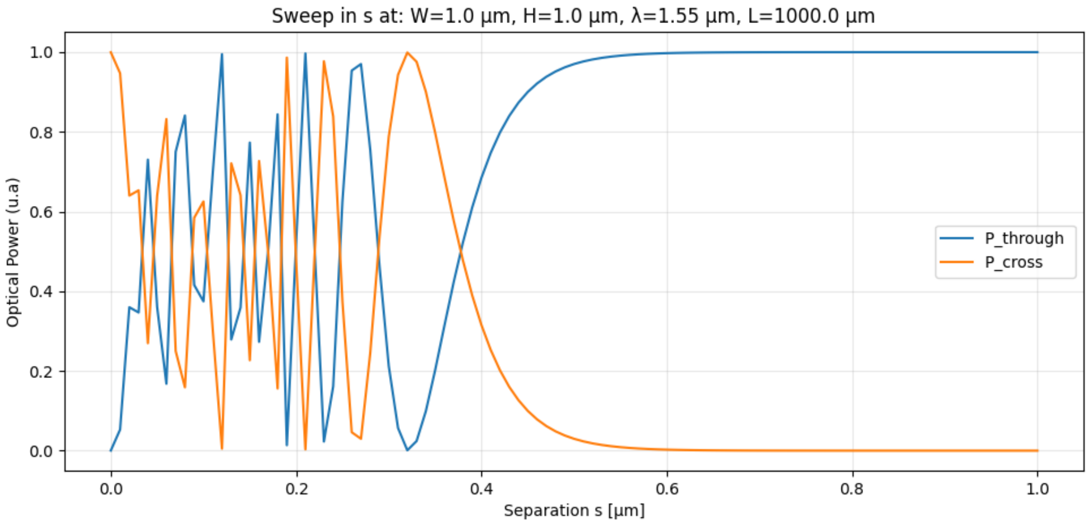

Figure 3.7 – Analysis of coupling levels for a variable distance for $s[0,1]$ μm.

Simulating the above parameters for two parallel a-Si:H guides on an SOI platform with air as an insulator (upper cladding), as shown in Figure 3.8, a) its representation and dimensions, when performing the simulation, the result obtained was the propagation in the z-axis for all TM/TE spectral components, as shown in b). This simulation is far more exact than the earlier one analyzed analytically, given that its algorithm is more specialized and considers more parameters. We will describe this algorithm later.

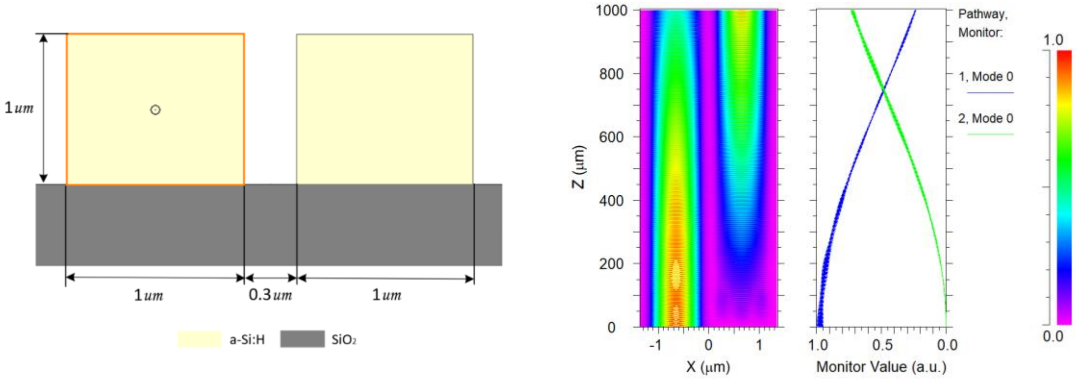

a) b)

Figure 3.8 – Simulation of coupling between parallel guides: a) front view and dimensions, b) power propagation along the z-axis in both guides.

An analysis of the coupling outputs concerning the s variation was also performed for a fixed length, as seen in Figure 3.9. The parameter s is found by the position of the guides with respect to 0, in the form $s = 2xx - width$, with both guides positioned centered at $-xx$ and xx. This analysis figures out that for $s \geq 0.72\ \mu m$ there is no coupling between the guides.

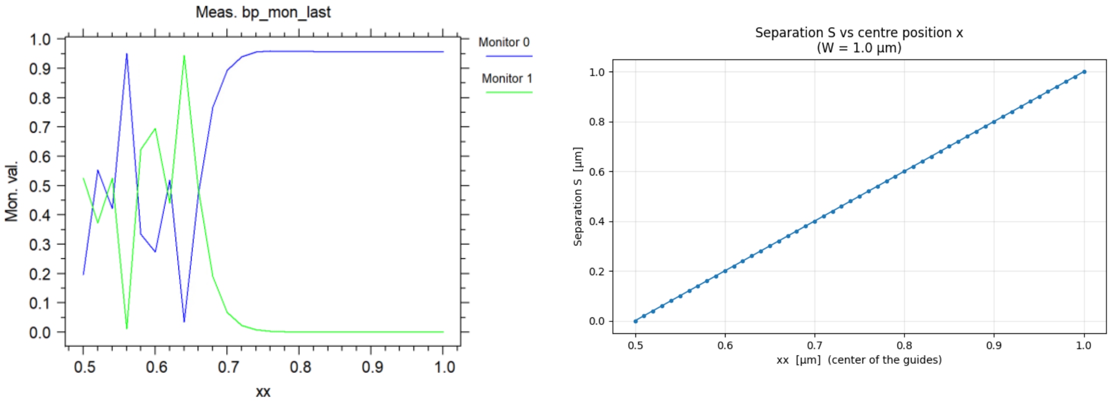

a) b)

Figure 3.9 – Simulation of coupling between parallel guides: a) analysis of coupling levels for a variable distance $s[0,1]$ (μm), b) distance s depending on position xx (μm) on both guides.

3.4 Simulation Tools

Throughout this document, we have conducted several analytical developments based on the theory presented in each chapter. Simulation and analysis tools were used to (i) confirm models, (ii) explore design spaces through parametric sweeps, and (iii) generate post-processing scripts and, on several occasions, create graphs to obtain a visual representation of them. MATLAB and Python were used as the main tools for calculation and analysis between physical models and experimental data collected from literature. This model of theory-physical models-results is fundamental when studying the principles of PICs, which later form the basis for working in professional software with more advanced models.

3.4.1 MATLAB

MATLAB is considered one of the leading engineering platforms, given its usefulness in various applications such as object-oriented programming, signal processing, robotics, communications systems, artificial intelligence, and control systems (for more information, consult [166]). For this work, the free online version, available at [166], was used, as shown in Figure 3.10. MathWorks markets this platform and offers a program allowing students to access MATLAB and Simulink through a license obtained by universities with agreements with the company.

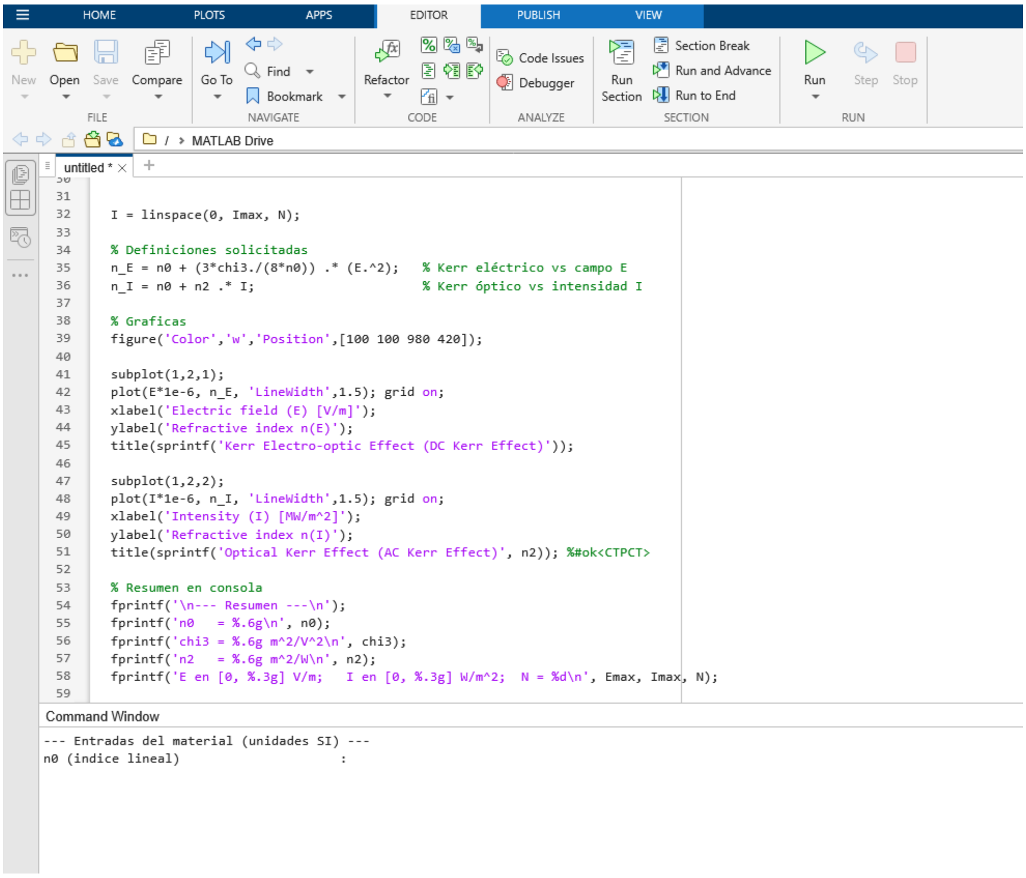

```

I = linspace(0, Imax, N);

% Definiciones solicitadas
n_E = n0 + (3*chi3./(8*n0)) .* (E.^2);   % Kerr eléctrico vs campo E
n_I = n0 + n2 .* I;                       % Kerr óptico vs intensidad I

% Graficas
figure('Color','w','Position',[100 100 980 420]);

subplot(1,2,1);
plot(E*1e-6, n_E, 'LineWidth',1.5); grid on;
xlabel('Electric field (E) [V/m]');
ylabel('Refractive index n(E)');
title(sprintf('Kerr Electro-optic Effect (DC Kerr Effect)'));

subplot(1,2,2);
plot(I*1e-6, n_I, 'LineWidth',1.5); grid on;
xlabel('Intensity (I) [MW/m^2]');
ylabel('Refractive index n(I)');
title(sprintf('Optical Kerr Effect (AC Kerr Effect)', n2)); %#ok<CTPCT>

% Resumen en consola
fprintf('\n--- Resumen ---\n');
fprintf('n0   = %.6g\n', n0);
fprintf('chi3 = %.6g m^2/V^2\n', chi3);
fprintf('n2   = %.6g m^2/W\n', n2);
fprintf('E en [0, %.3g] V/m;   I en [0, %.3g] W/m^2;  N = %d\n', Emax, Imax, N);

```

```
--- Entradas del material (unidades SI) ---
n0 (indice lineal)                    :
```

Figure 3.10 – MATLAB online workspace environment.

3.4.2 Python

Python has become popular in the academic and scientific community over the last decade. It is a multi-paradigm language (imperative, object-oriented, and lightweight functional). It stands out for the simplicity of its code and its multi-platform compatibility, as well as being open-source software, which eases collaboration, access to thousands of libraries, and rapid evolution of the tool. It is used for everything and is popular for its results in automation and scripting, data analysis, science/engineering, web applications, rapid prototyping, machine learning, AI, and command line tools. There is a large community of Python developers, and a wealth of documentation on its official website, where you can find more information and download the latest versions in [167]. In this work, Python version 3.12.4 for Windows has been used, as shown in Figure 3.11, in a free source code editor environment, Visual Studio Code (VS Code).

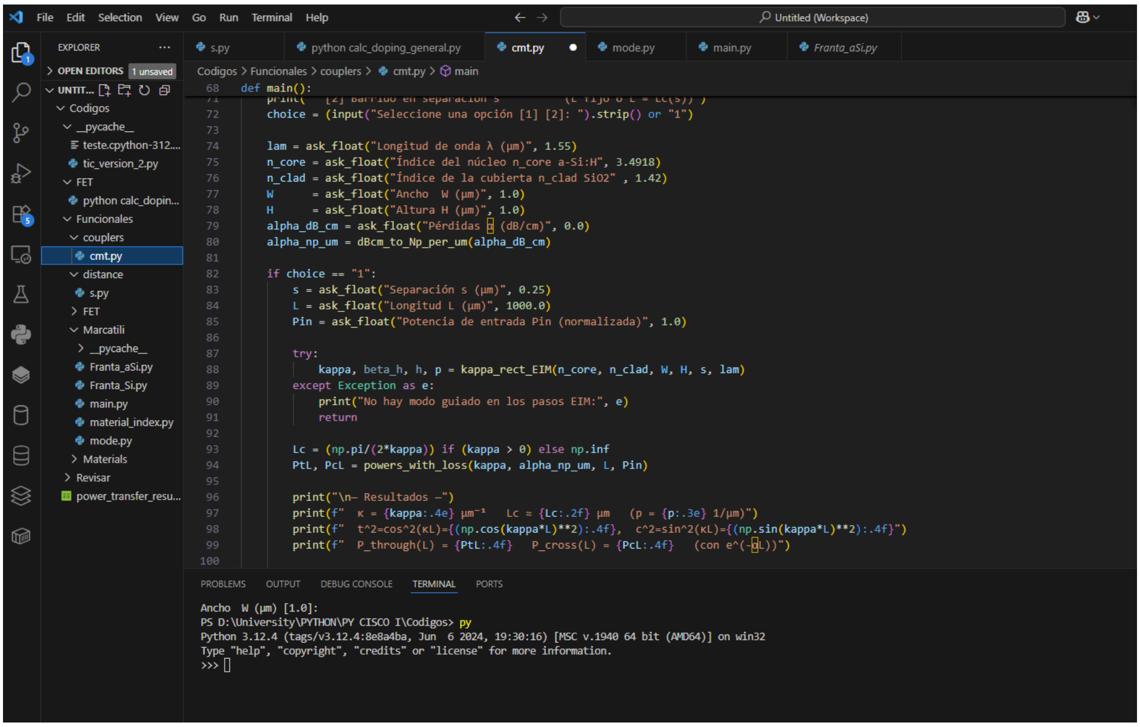

```python
def main():
    choice = (input("Seleccione una opción [1] [2]: ").strip() or "1")

    lam = ask_float("Longitud de onda λ (µm)", 1.55)
    n_core = ask_float("Índice del núcleo n_core a-Si:H", 3.4918)
    n_clad = ask_float("Índice de la cubierta n_clad SiO2" , 1.42)
    W      = ask_float("Ancho  W (µm)", 1.0)
    H      = ask_float("Altura H (µm)", 1.0)
    alpha_dB_cm = ask_float("Pérdidas α (dB/cm)", 0.0)
    alpha_np_um = dBcm_to_Np_per_um(alpha_dB_cm)

    if choice == "1":
        s = ask_float("Separación s (µm)", 0.25)
        L = ask_float("Longitud L (µm)", 1000.0)
        Pin = ask_float("Potencia de entrada Pin (normalizada)", 1.0)

        try:
            kappa, beta_h, h, p = kappa_rect_EIM(n_core, n_clad, W, H, s, lam)
        except Exception as e:
            print("No hay modo guiado en los pasos EIM:", e)
            return

        Lc = (np.pi/(2*kappa)) if (kappa > 0) else np.inf
        PtL, PcL = powers_with_loss(kappa, alpha_np_um, L, Pin)

        print("\n— Resultados —")
        print(f"  κ = {kappa:.4e} µm⁻¹   Lc ≈ {Lc:.2f} µm   (p = {p:.3e} 1/µm)")
        print(f"  t^2=cos^2(κL)={(np.cos(kappa*L)**2):.4f},  c^2=sin^2(κL)={(np.sin(kappa*L)**2):.4f}")
        print(f"  P_through(L) = {PtL:.4f}   P_cross(L) = {PcL:.4f}   (con e^(-αL))")
```

```
Ancho  W (µm) [1.0]:
PS D:\University\PYTHON\PY CISCO I\Codigos> py
Python 3.12.4 (tags/v3.12.4:8e8a4ba, Jun  6 2024, 19:30:16) [MSC v.1940 64 bit (AMD64)] on win32
Type "help", "copyright", "credits" or "license" for more information.
>>> 
```

Figure 3.11 – Python Workspace environment.

3.4.3 Rsoft CAD-Layout

Synopsys' RSoft Photonic Device Tools is a suite of simulators and optimizers for the design of active and passive photonic devices, which integrates easily with other Synopsys solutions such as CODE V (for imaging optics) and Sentaurus TCAD (for complete electro-optical simulation). Thanks to the implementation of advanced algorithms, it is possible to design virtual photonic prototypes with great precision, thus reducing the trial-and-error stages in the design of conventional physical prototypes, which are costly. These solutions accelerate the design cycle to market production, from simple devices to more challenging projects. In our work, we will use the Rsoft CAD-Layout version 2024.09, a design platform that integrates several tools, as shown in Figure 3.12.

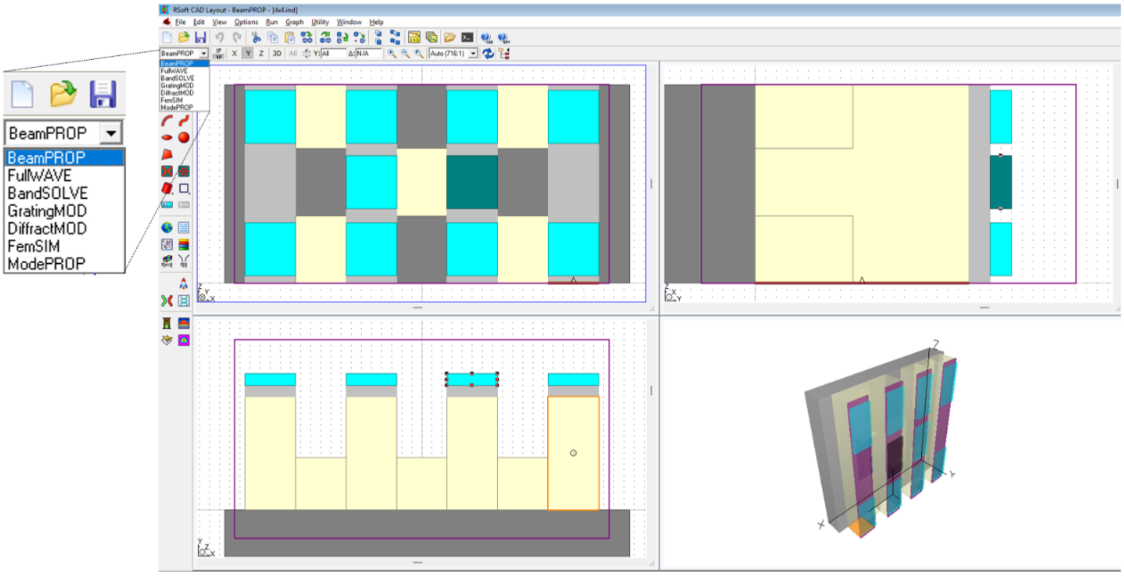

Figure 3.12 – Rsoft CAD-Layout environment.

The main tools or methods of analysis used in this work are,

3.4.3.1 Finite Difference Time Domain (FDTD)

The finite difference time domain (FDTD) method is a powerful and efficient tool for modeling approximations with extremely high precision in nanoscale photonic devices. This method can solve complicated problems, but it is computationally expensive. Depending on the complexity and the algorithm used, solutions may require greater memory capacity in the system, resulting in longer calculation times. The FDTD method falls under the category of "resonance region" techniques, which are characterized by the fact that the characteristic dimensions of the domain of interest are approximately the size of a wavelength [168], this method employs finite differences as approximations to both the spatial and temporal derivatives that appear in Maxwell's equations. FDTD solves Maxwell's equations on a mesh and computes $\vec{E}$ and $\vec{H}$ at grid points spaced Δx, Δy, and Δz apart, with $\vec{E}$ and $\vec{H}$ interlaced in all three spatial dimensions. FDTD is a powerful tool that includes within its parameters the effects of absorption, dispersion, transmission, and reflection, among other relevant Electromagnetic Phenomena (EMP). Although it is a time-domain solution, it is possible to perform frequency analysis using techniques such as the Fast Fourier Transform (FFT) and the Discrete Fourier Transform (DFT) [169].

The technological domains that benefit from the FDTD method are among the most significant, including Biomedicine: bioimaging, bio-photonics, bioelectronics, and biosensors. Geophysics: space weather hazards, remote sensing, communications, and geolocation. Metamaterials: continuously scanning leaky-wave antennas, subwavelength focusing lenses, electromagnetic cloaks, and Optics: diffractive optical elements, photonic bandgap structures, photonic crystal waveguides, and ring-resonator devices. Plasmonic: plasmonic waveguides and antennas; and Quantum applications: quantum devices and quantum radar [170].

3.4.3.2 Beam Propagation Method (BPM).

The beam propagation method (BPM) is a conceptually simple algorithm that offers a fast response. It propagates a coherent light beam in dielectric waveguides or structures whose geometry and index vary smoothly along the propagation direction. The method involves propagating the input beam a short distance through homogeneous space, then correcting for the variations in the refractive index experienced by the beam during propagation. The light beam propagates through the guide or the designed medium (using classical diffraction formulas), a short distance Δz along the z-axis before being sent through a phase/amplitude mask. The properties of the mask are derived from the cross-sectional profile of the waveguide (or other structure) in which the beam exists. The algorithm alternates free-space diffraction with mask transmission, repeating the cycle until the beam reaches the output plane or the excited guided modes settle to a steady state [171].

In the Synopsys solution, this method is a tool known as BeamPROP, which has applications in a wide range of integrated and fiber-optic devices including, but not limited to: WDM devices such as Arrayed Waveguide Grating (AWG) routers, Switches, e.g. directional coupler-based or digital-y type, Modulators, e.g. Mach-Zehnder type, Multimode interference devices (MMI), Passive 1 x N or N x N splitters, Laser structure transverse mode analysis, Standard and specialty fiber design, Gratings and Sensor structures [169].

3.4.3.3 Finite Element Method (FEM)

The Finite Element Method (FEM) is a numerical method for solving diverse types of differential equations, transforming infinitesimal functions into finite functions. These functions are then converted into ordinary vectors in a vector space that can be solved numerically, to segment the domain into small elements known as triangles and squares, thus seeking a polynomial approximation of the dependent variables (unknown functions) in each component. After applying the finite element method, these functions are converted into ordinary vectors. This approach combines discrete approximations to obtain a global solution.

This method is part of RSoft Photonic Device Tools, which is implemented in the FemSIM tool. This tool can be characterized as a generalized mode solver capable of calculating guided, filtering, and cavity modes, both in waveguides and cavities, in 1D or 2D cross sections, as well as in any arbitrary structure (2D/3D, Cartesian, and cylindrical), including structures that comprise non-uniform meshes, as shown in Figure 3.13. It supports complex indices (lossy materials/metal), high index contrast structures, metal-dielectric plasmons, and photonic bandgap-based waveguides [169].

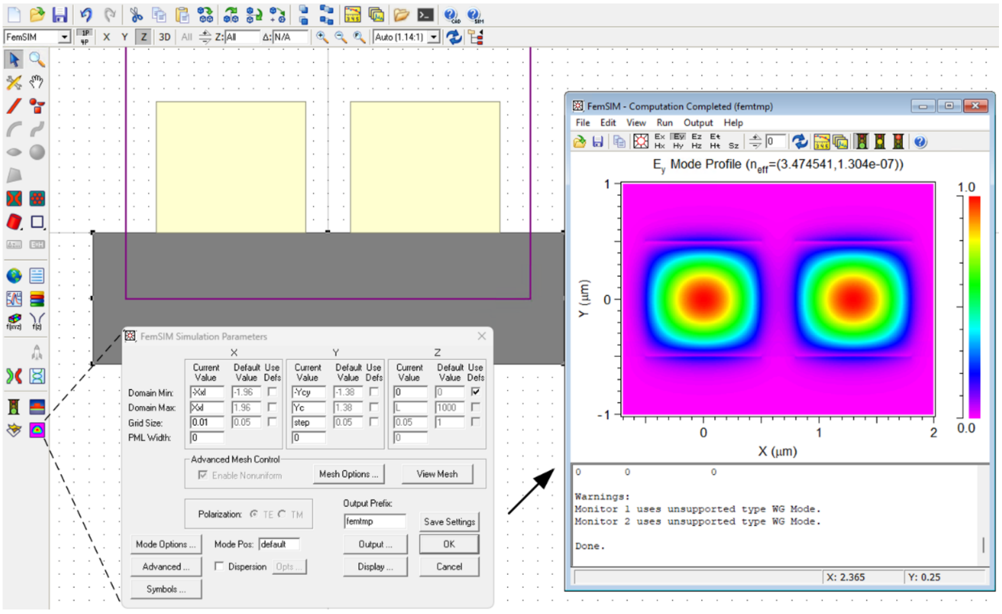

	X Current Value	X Default Value	X Use Defs	Y Current Value	Y Default Value	Y Use Defs	Z Current Value	Z Default Value	Z Use Defs
Domain Min:	-Xxl	-1.96	☐	-Ycy	-1.38	☐	0	0	☑
Domain Max:	Xxl	1.96	☐	Yc	1.38	☐	L	1000	☐
Grid Size:	0.01	0.05	☐	step	0.05	☐	0.05	1	☐
PML Width:	0			0			0		

☑ Enable Nonuniform

Polarization: ● TE ○ TM

Output Prefix: femtmp

Mode Pos: default

☐ Dispersion

```
0       0             0

Warnings:
Monitor 1 uses unsupported type WG Mode.
Monitor 2 uses unsupported type WG Mode.

Done.
```

X: 2.365 Y: 0.25

Figure 3.13 – Rsoft CAD-Layout FemSIM tool.

4 Programmable photonic circuits

In the previous chapters, we analyzed the basic principles and analytical formulations of the optical and optoelectronic properties to be considered when selecting the most suitable materials for designing and manufacturing waveguides and other integrated photonic applications. A brief analysis was made of the most used architectures for applications such as modulators and programmable photonic circuits, together with the optoelectronic effects used as control techniques, such as the thermo-optic effect, electro-optic effect, plasma dispersion, and free carrier modulation. Likewise, the essential passive components were described, from waveguide engineering to directional couplers. This topic introduces and analyzes a new 4X4 matrix device capable of switching optical signals as an RASPIC solution based on the use of directional couplers with a Horn-Slab Directional Coupler (HSDC) configuration. This structure will be examined for control using the thermo-optic effect and carrier depletion phenomena. The proposed architecture, design criteria, simulation results, and performance comparison between control mechanisms will be detailed, proving their potential for densely integrated photonic networks.

4.1 Thermo-Optic Directional Coupler

Based on what we have previously analyzed for passive directional couplers, we will use the thermo-optic effect as a control element based on the analysis of parallel waveguides, as shown in Figure 3.5 a). However, these directional couplers use S-bends as transition structures to bring the parallel waveguides closer together or separate them in the coupling region, as seen in Figure 1.3 a), we will focus on the coupling region.

Figure 4.1 shows the configuration of the thermo-optic directional coupler, its dimensions, and materials. For this analysis, the coupler length was kept at L=1000 μm, and the exact dimensions of the 1 μm x 1 μm guides were used, as in the earlier analyses, to obtain a total optical power transfer between guides (PCross) at ΔT=0K.

The distance between guides was simulated for $s = 0.2\ \mu m$, which is within the actual values of the distance between guides, as mentioned above.

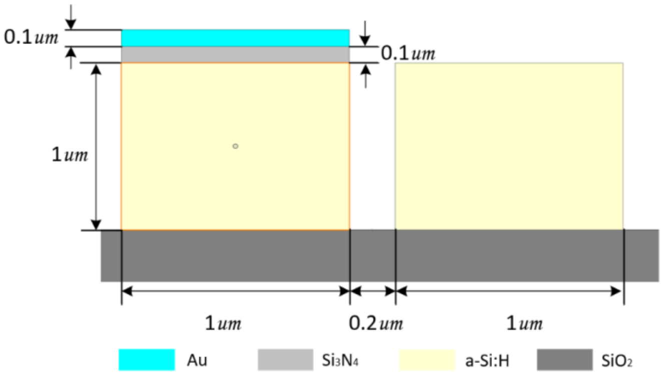

Figure 4.1– Thermo-Optic Directional Coupler, dimensions and materials used.

Figure 4.2 shows the PCross and PThrough functionality obtained for ΔT=0K and ΔT=35K, respectively.

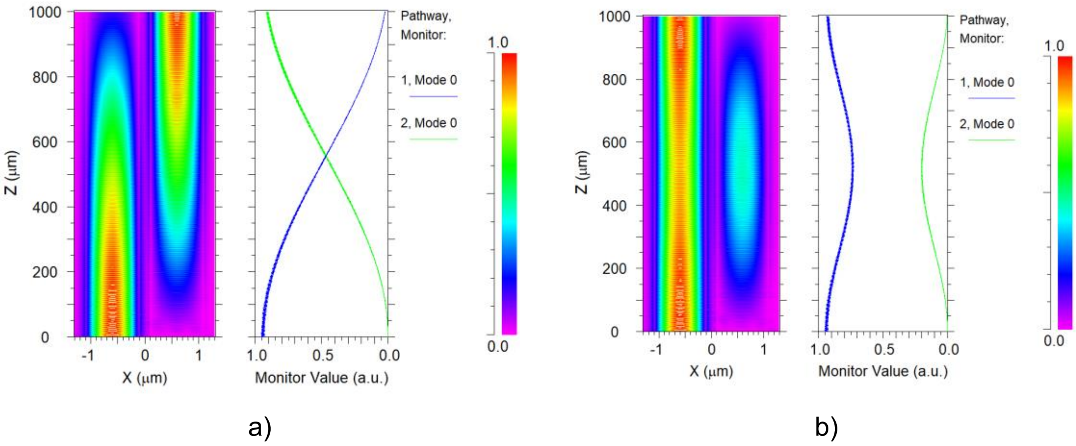

Figure 4.2 – Evolution of the fundamental TE mode on the z-axis in, a) ΔT=0K, b) ΔT=35K.

A temperature variation of ΔT=35K was necessary to confine the light in the first guide, given that the guides are so close together that thermal crosstalk occurs, which causes the refractive index of the parallel guide also to increase. For this reason, a higher temperature is needed to break the modal profile induced in the second guide and confine the light in the first guide by further increasing its index. This can be seen in the thermal profile shown in Figure 4.3.

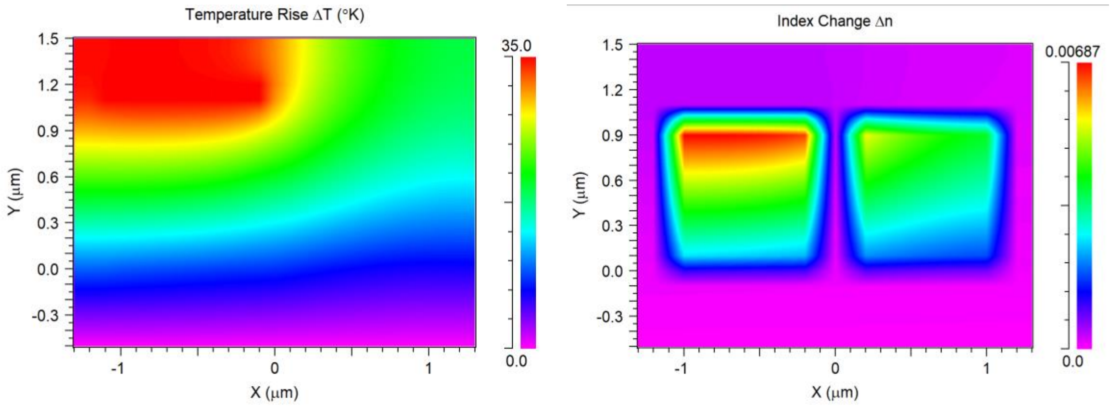

a) b)

Figure 4.3 – Thermo-Optic Directional Coupler, a) thermal profile for ΔT=35K, b) variation of the refractive index with temperature.

4.2 Horn-Slab Directional Coupler

The analysis performed on the directional couplers in Figure 3.8 b) shows the propagation along the z-axis, which corresponds to the propagation of the light beam as the total field of the quasi-TE and quasi-TM modes (hybrid modes in 3D). Although mode propagation was not addressed in this work due to the scope of the analysis, this information can be studied and analyzed in [156, 172]. However, in communications and photonic waveguides, propagation in the fundamental TE mode is of interest. This can be seen in Figure 4.1, where simulations were performed with the same parameters as seen before in Figure 3.8 for a) TE modes, b) TM modes; the mode that propagates best is the TM, where the result coincides with Figure 3.8 b).

In our simulations, we have used Air as the upper cladding, where $n_{Air} = 1$, for the gap between guides (s). In terms of mode propagations, the gap figures out the rate at which the evanescent tails of the excited modes “flap” from one guide to another, determining the coupling transfer between guides. If the evanescent tail penetrates further into the gap, the modal separation increases and the coupling is reinforced; if it fades faster, the opposite occurs.

The medium also contributes to scattering and absorption depending on the material used as the gap, which is why Air is widely used. In practice, raising the effective index of the medium in the gap reduces the contrast with the core, expands the mode outside the guide, and increases the coupling (shorter coupling length), as observed in simulations performed for an SiO_2 gap in Figure 4.4.

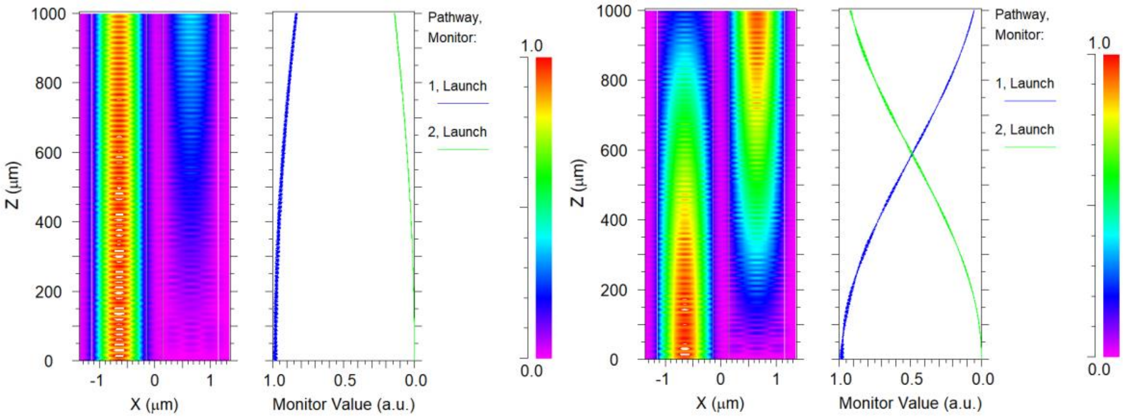

a) b)

Figure 4.4 – Evolution of optical propagation along the z-axis with an SiO_2 gap for: a) fundamental TE mode, b) fundamental TM mode.

SiO_2 has an $n_{SiO_2} = 1.42$, a value greater than Air but less than n in the guides. If, instead of SiO_2 as the gap, we used the same material as the guides, the gap between the guides would become the same continuous core, and there would no longer be two separate parallel guides. There would be a single guide with a higher W, meaning we would be in the MMI regime, as shown in Figure 4.5.

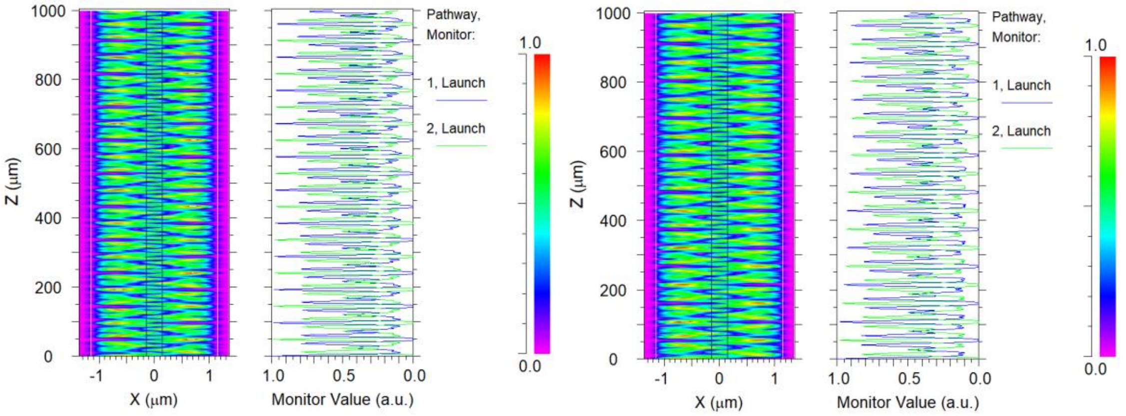

a) b)

Figure 4.5 – Evolution of optical propagation along the z-axis with an a-Si:H gap for: a) fundamental TE mode, b) fundamental TM mode.

As we saw earlier, using another material as the gap reduces the coupling length and, consequently, makes it possible to increase the distance s. Following this idea to achieve a separation between the guides of $s \geq 1um$, due to its horn shape, the following configuration was obtained: the Horn-Slab Directional Coupler, shown in Figure 4.6.

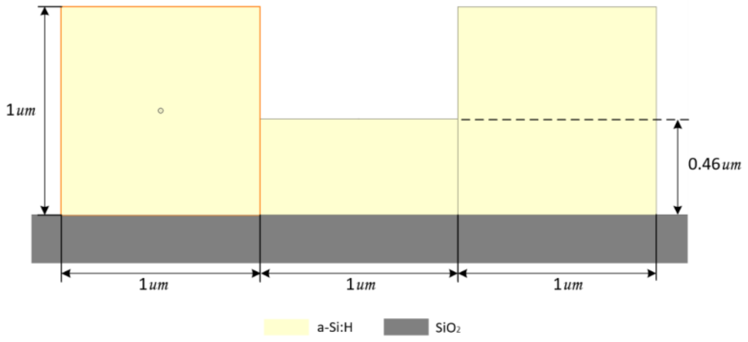

Figure 4.6 – Horn-Slab Directional Coupler.

When simulating for $\mathrm{L} = 950\ \mu\mathrm{m}$, Figure 4.7 shows total coupling (PCross) for the fundamental TE mode. In this configuration, the TM mode does not propagate. This device has an insertion loss of $\mathrm{IL} = 0.46\ \mathrm{dB}$ and a propagation loss of $\mathrm{PL} = 0.15\ \mathrm{dB}$ due to internal guide attenuation and loss between mode transfer by the slab.

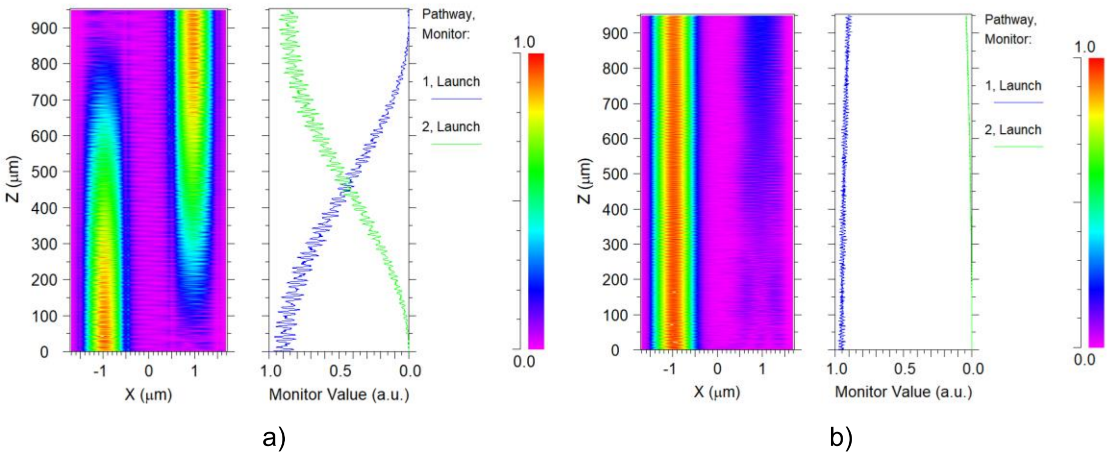

a) b)

Figure 4.7 – Evolution of optical propagation along the z-axis: a) fundamental TE mode, b) fundamental TM mode.

4.2.1 Thermo-Optic Horn-Slab Directional Coupler

To analyze the thermo-optic effect, we will implement the configuration in our Horn-Slab Directional Coupler as shown in Figure 4.8.

In this default PCross configuration at T=300K, when applying temperature to one of the guides, we want the light to be confined to the heated guide, thus obtaining control with the temperature of the states, PCross, PThrough.

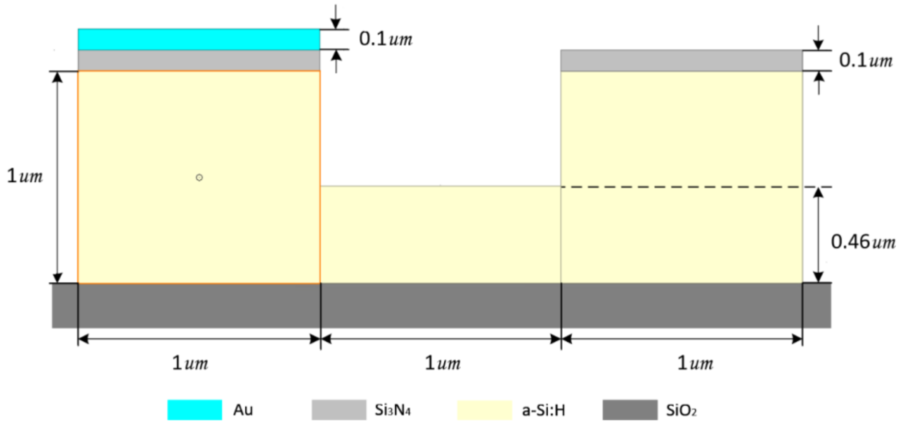

Figure 4.8 – Thermo-Optic Horn-Slab Directional Coupler, dimensions and materials used.

For a heater length of L=750 μm, centered, in Figure 4.9, we can see the thermal profile at ΔT=15K. The air gap between the guides and the upper Si_3N_4 cladding limits thermal diffusion, so the core of the second guide experiences greater thermal insulation in this design, as can be seen in b). This avoids spurious resonances and mitigates the thermal crosstalk, thereby keeping the phase of the unheated guide stable.

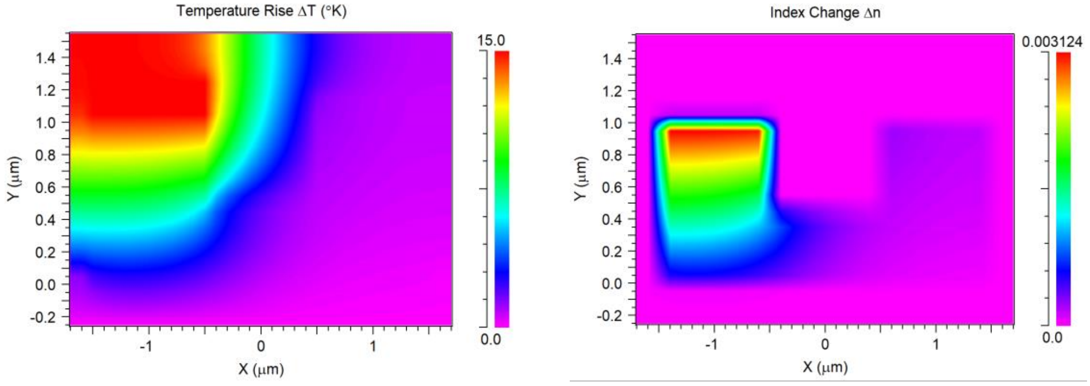

a) b)

Figure 4.9 – Thermo-Optic Horn-Slab Directional Coupler: a) thermal profile generated by the heater at ΔT=15K, b) variation in the refractive index in the guide excited by temperature.

In Figure 4.10, we have in a) the transverse profile of the indices of the materials used and b) the propagation in the z-axis for the fundamental TE mode when the heater is activated at ΔT=15K. At this temperature, confinement occurs in the main guide, thus achieving a transition from the default PCross state at ΔT=0K to PThrough. In this way, we control the direction of the light beam between the two outputs of the coupler.

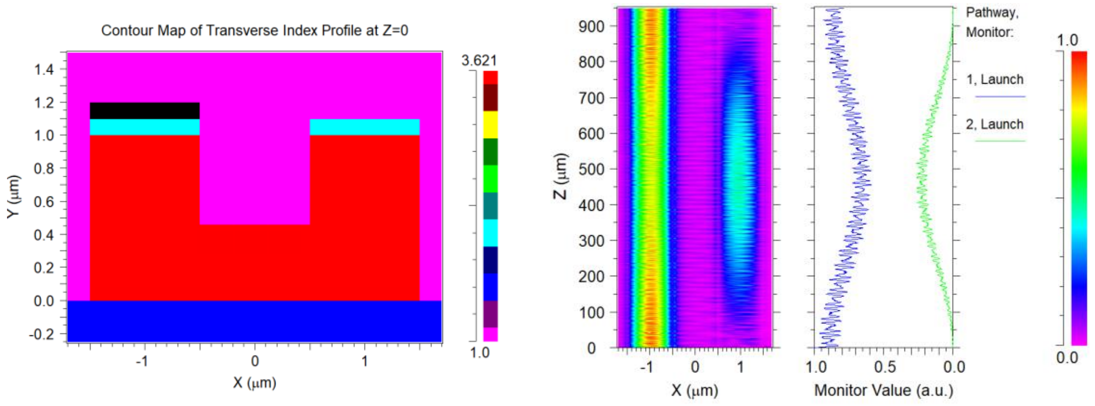

a) b)

Figure 4.10 – Thermo-Optic Horn-Slab Directional Coupler: a) refractive index profile , b) evolution of optical propagation along the z-axis for fundamental TE mode at ΔT=15K.

4.3 4×4 Programmable PIC Matrix Based on Amorphous Silicon Using the Thermo-Optic Effect.

The proposed structure can be seen in Figure 4.11, which shows different views of the 4X4 Programmable PIC Matrix design based on Amorphous Silicon Controlled by the Thermo-Optic Effect. Composed of a structure based on a Horn-Slab directional coupler, this compact structure is designed to reduce the number of active elements (heaters) for controlling the outputs depending on an input. This structure has dimensions of 2800 µm x 7 µm, as shown in b), and is composed of three segments with lengths L1=L2=950 µm and L3=900 µm, as shown in d).

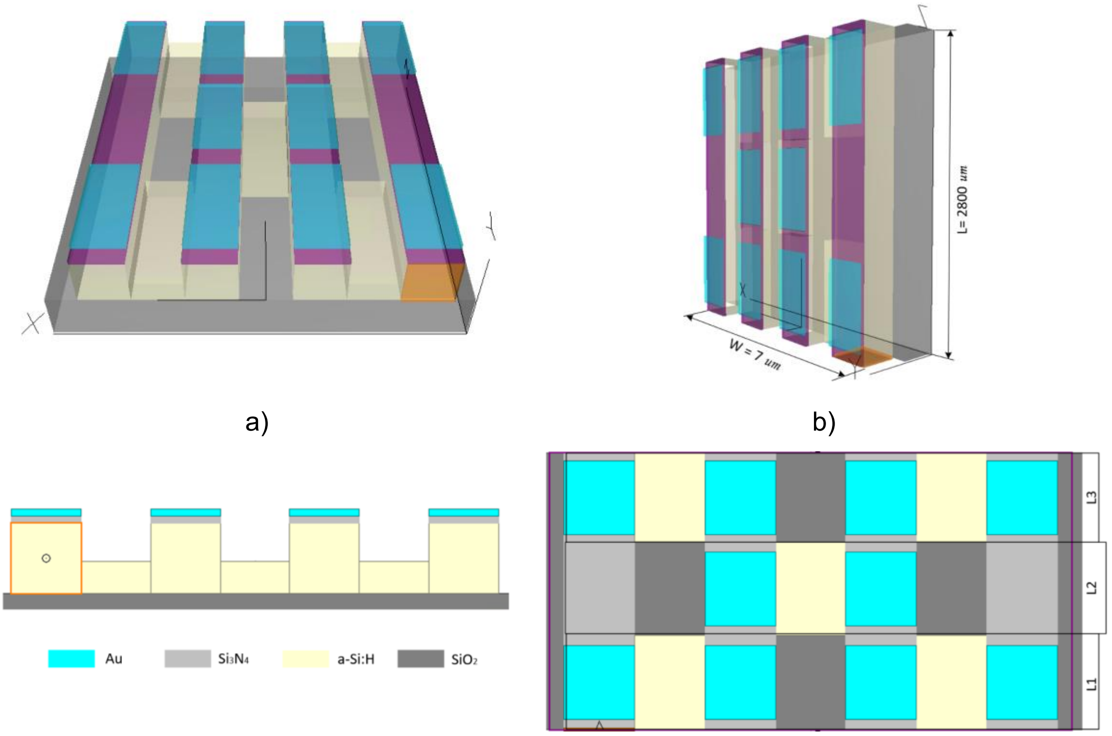

a) b)

c) d)

Figure 4.11 – Representation of the programmable 4X4 matrix views, a) 3D front isometric view, b) 3D lateral isometric view, c) 2D front view, and d) 2D top view.

The blocks were designed with a PCross configuration, as seen in Figure 4.8. When no control element is activated in a 2X2 directional coupler, the light injected into one guide is transferred entirely to the unexcited parallel guide, so the default output corresponds to the cross port. The state map shown in Figure 4.12 was drawn up for each input port and its optimized combinations.

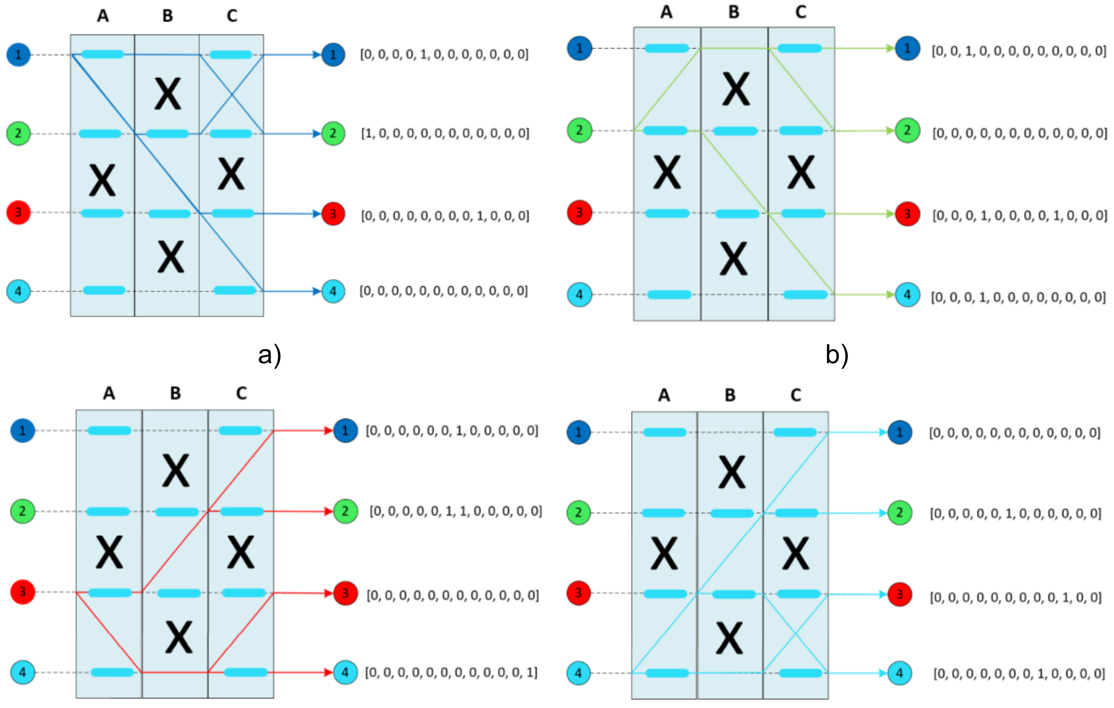

a) b) c) d)

Figure 4.12 – State map used in the 4 × 4 programmable PIC matrix (TOE), a) 1x4 configuration, 2x4 configuration, c) 3x4 configuration, d) 4x4 configuration.

Figure 4.12 illustrates four switching states of the 4X4 programmable matrices, where the inputs are numbered from 1 to 4, and the columns [A, B, C] are identified above the matrix. Next to each output is a binary vector, where **1** indicates the heater is activated and **0** indicates the heater is deactivated. These bits correspond to the thermo-optical electrodes analyzed in previous chapters. Using the first image at the top left as an example, we have the output [0, 0, 0, 0, 1, 0, 0, 0, 0, 0, 0, 0], which can be read as follows in Table 4.1,

Table 4.1 – Values to activate an electrode in the 1x1 configuration.

Optical Input	A	B	C
1	0	0	0
2	0	1	0
3	0	0	0
4	0	0	0

As can be seen in Table 4.1, for the 1x1 configuration (input 1 / output 1), the optical signal is at the first input, and we want to redirect it to the first output. Only a DC pulse is needed at position 2B; this has the light in segment 2B, and then when it passes to segment 2C, it performs a total transfer of the optical power to the guide in 1C, given that by default, in the absence of temperature, the circuit has a PCross configuration. For example, when applying optical power in the first guide, the default output is 4. This configuration is 1x4, and it can be seen in Figure 4.10 a), that, as can be seen, the electrode (heater) is not activated for this configuration.

After this analysis, the following question arises:
Is it better to confine the light along the guide, that is, by activating electrodes 1A-1C?

If possible, the problem with this solution is the system's thermal efficiency, as it is necessary to activate two heaters instead of one, and the system consumes more energy. in addition to compromising speed given the times between hot/cold states (recovery), although the outputs are relatively the same for both cases, as can be seen in Figure 4.13, where a) shows the trajectory activating the heater (dark cyan) in 2B and b) shows the trajectory activating the heaters in 1A and 1C.

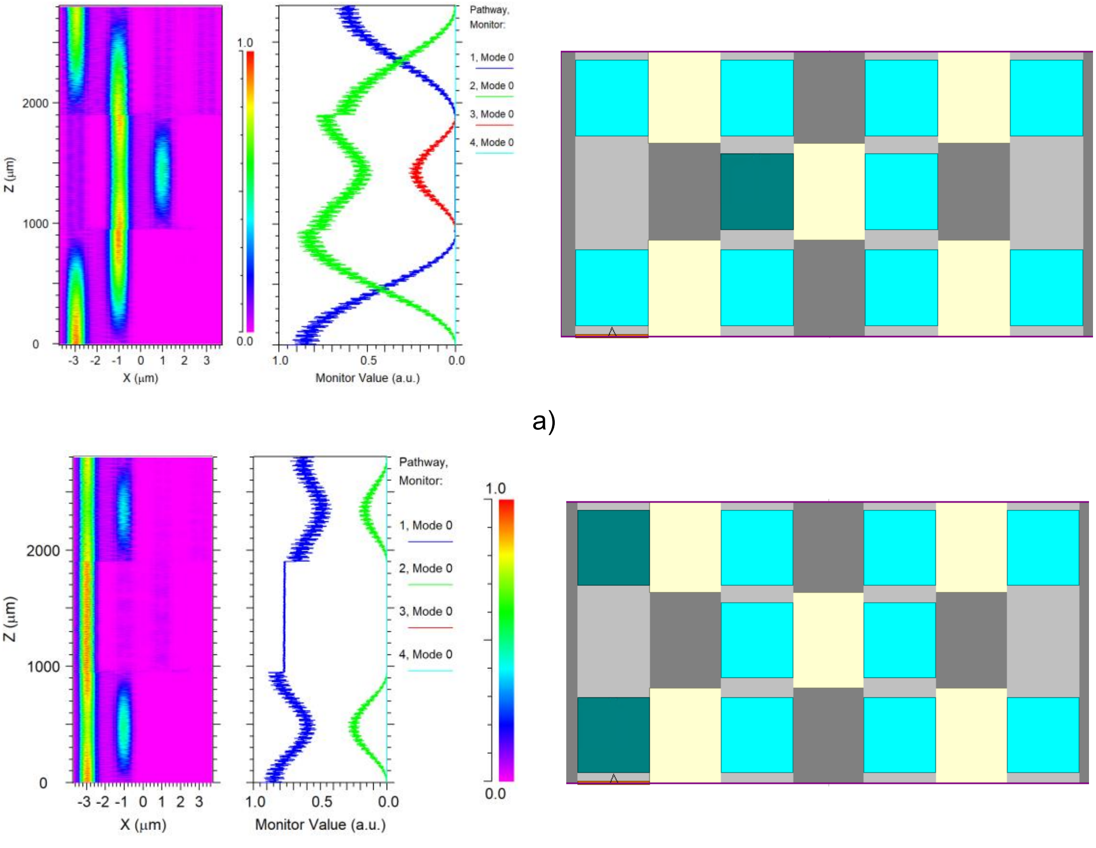

a)

b)

Figure 4.13 – Simulation results in the 4 × 4 programmable PIC matrix: a) evolution of the fundamental TE mode on the z-axis in: a) 1x1 configuration using one heater (2B), b) evolution of the fundamental TE mode on the z-axis in a 1x1 configuration using two heaters (1A-1C).

If we look again at Figure 4.12, we can see that there is a gap between the guides, this refers to areas with no coupling, typical of Horn-Slab directional couplers. These are identified with the symbol “X,” marking the positions without optical coupling. This solution avoids the need for typical “S” curves, reducing length, mask complexity, and bending losses. By using only straight sections and controlled directional couplers, the device is more compact and easier to manufacture and more robust against lithography and alignment errors present in conventional curved interconnections.

We will analyze the results obtained through simulations in the BeamPROP tool. To do this, we will use the configurations shown in Figure 4.12 to activate the heaters for each combination. We will analyze the optical power level at the output for each combination to analyze the proposed device's performance.

Figure 4.14 shows the evolution of the fundamental TE mode on the z-axis for each of the combinations from input one and their combinations at the output for the first configuration referred to in Figure 4.12 a).

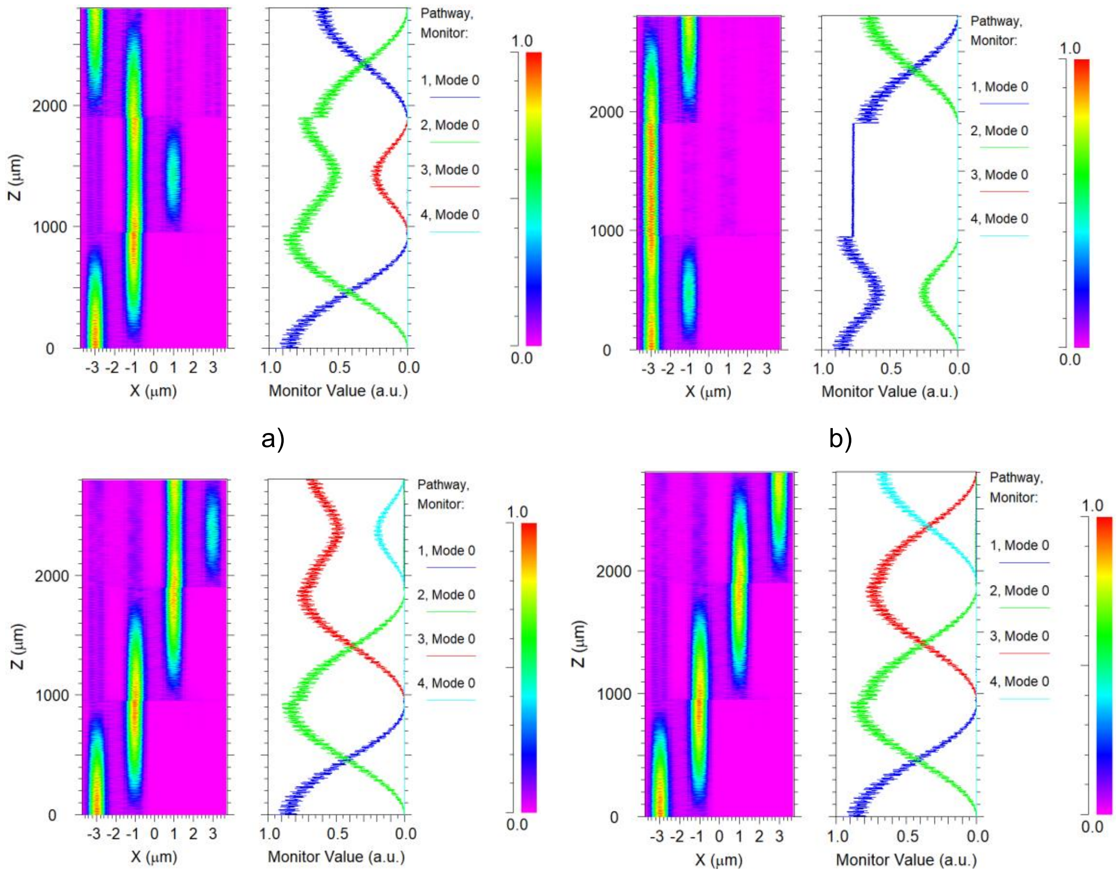

a)

b)

c)

d)

Figure 4.14 – Evolution of the fundamental TE mode on the z-axis in: a) 1x1 configuration, b) 1x2 configuration , c) 1x3 configuration, d) 1x4 configuration.

Figure 4.15 shows the evolution of the fundamental TE mode on the z-axis for each of the combinations from input two and their combinations at the output for the first configuration referred to in Figure 4.12 b).

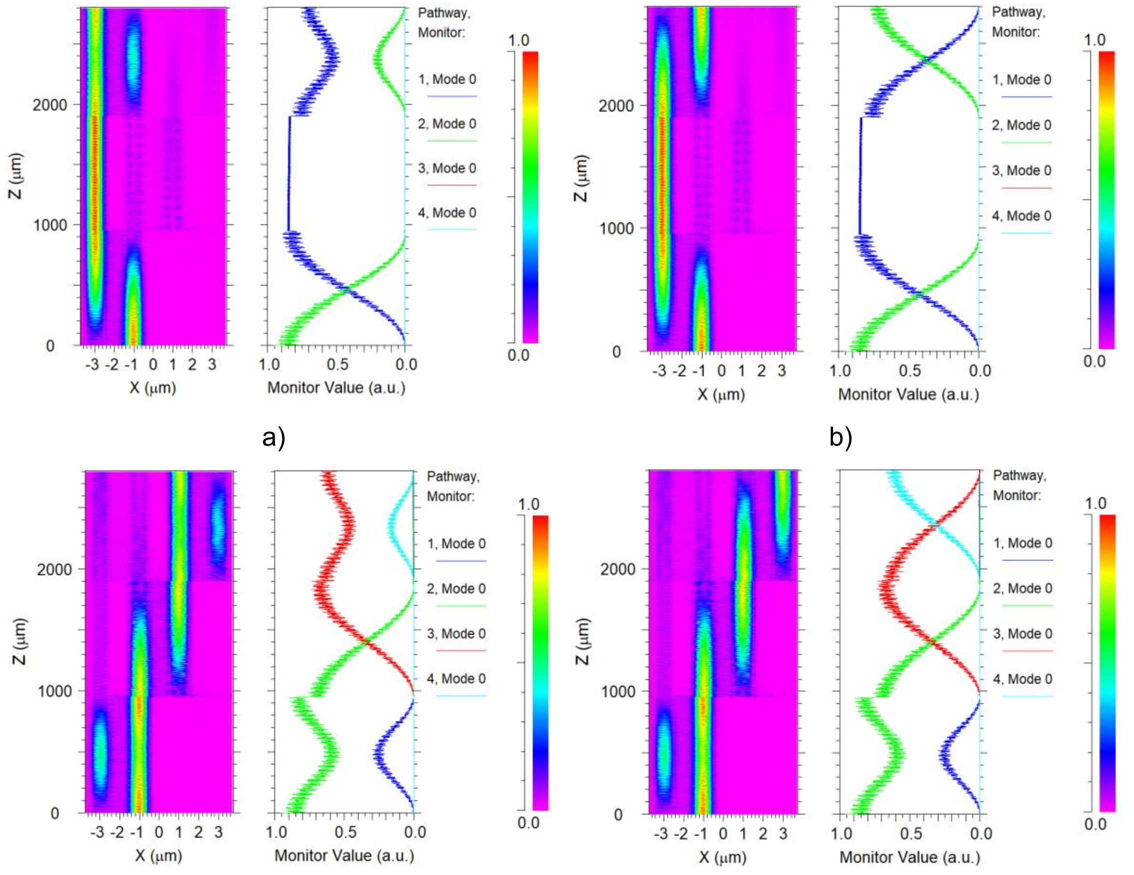

a)

b)

c)

d)

Figure 4.15 – Evolution of the fundamental TE mode on the z-axis in: a) 2x1 configuration, b) 2x2 configuration, c) 2x3 configuration, d) 2x4 configuration.

Figure 4.16 shows the evolution of the fundamental TE mode on the z-axis for each of the combinations of input three and their combinations at the output for the first configuration referred to in Figure 4.12 c).

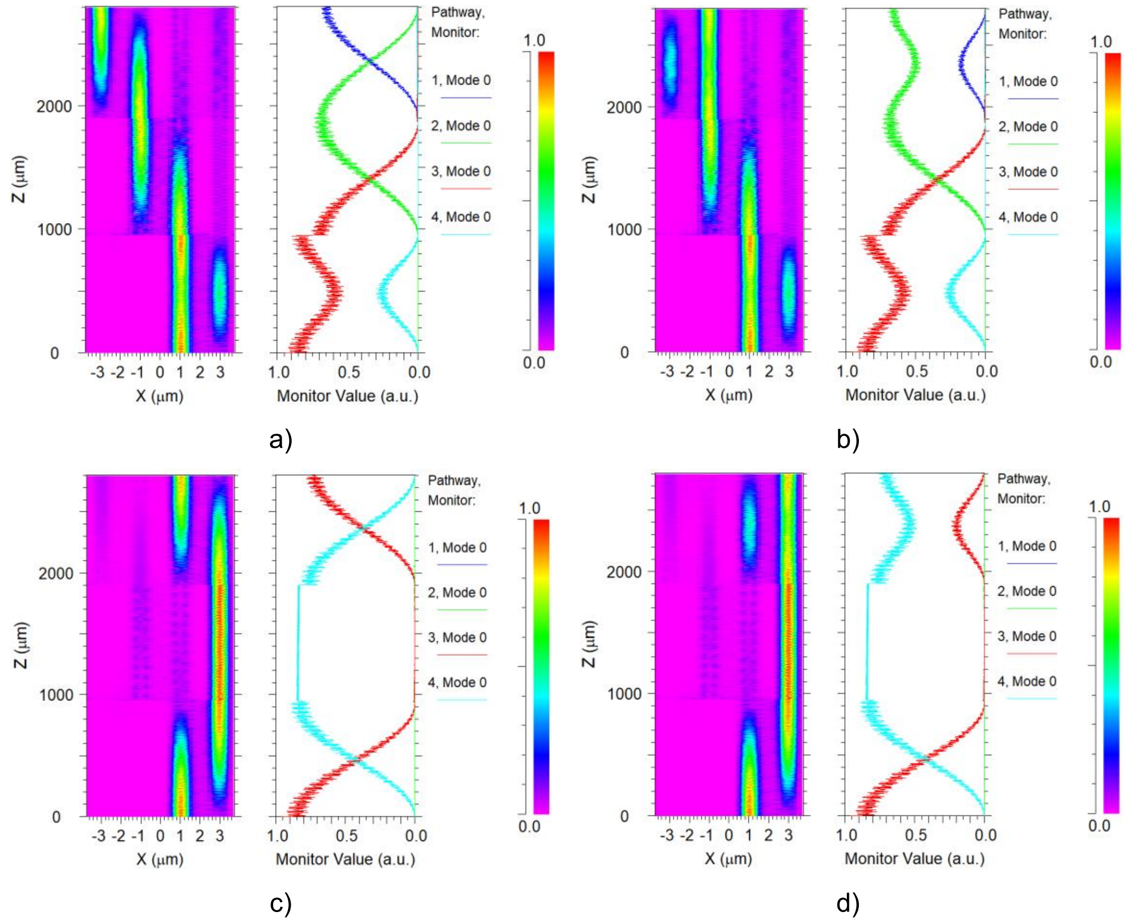

Figure 4.16 – Evolution of the fundamental TE mode on the z-axis in: a) 3x1 configuration, b) 3x2 configuration, c) 3x3 configuration, d) 3x4 configuration.

Figure 4.17 shows the evolution of the fundamental TE mode on the z-axis for each of the combinations from input four and their combinations at the output for the first configuration referred to in Figure 4.12 d).

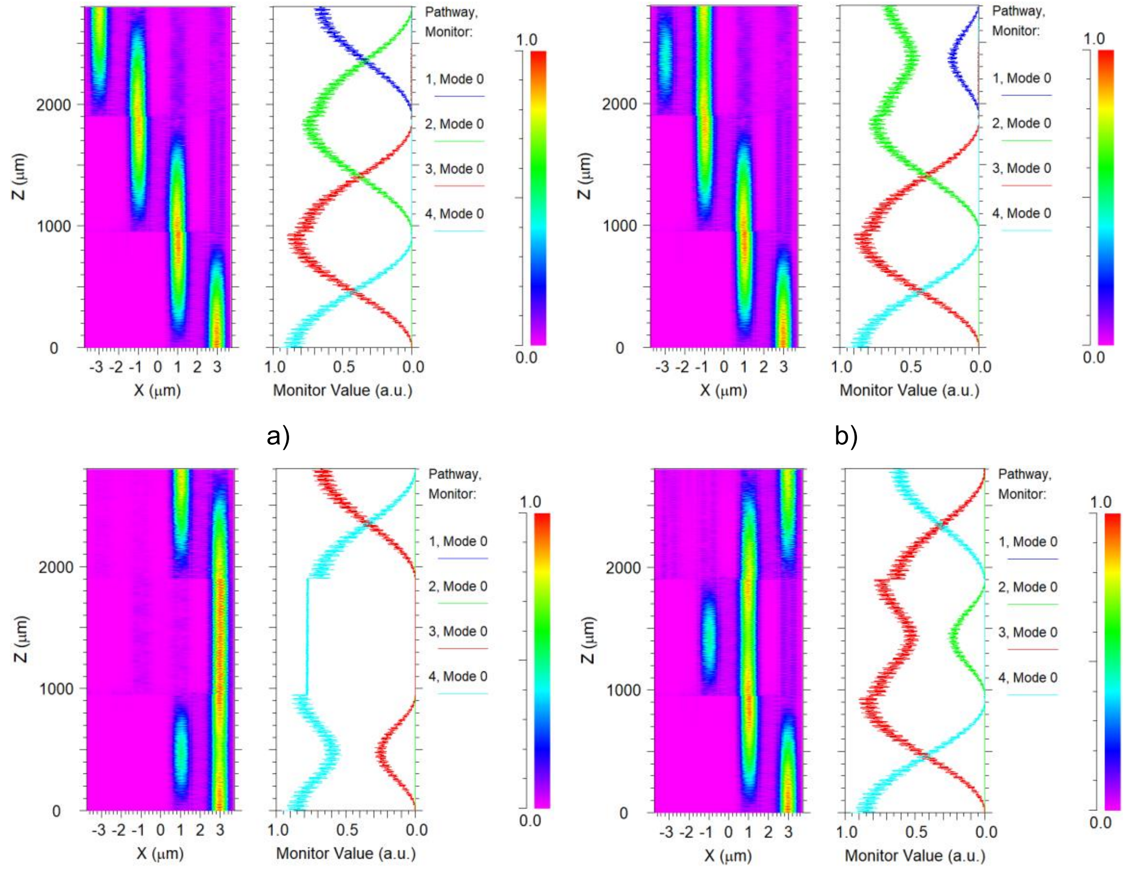

a)

b)

c)

d)

Figure 4.17 – Evolution of the fundamental TE mode on the z-axis in: a) 4x1 configuration, b) 4x2 configuration, c) 4x3 configuration, d) 4x4 configuration.

In the simulations performed, the optical power of the laser, normalized to 1 (u.a) once coupled to our device, drops to 0.85 (u.a). This reduction in power is due to an insertion loss (IL) of $IL \simeq 0.7\ dB$, which originates in the coupling stage with the source. This can be caused by a modal mismatch when the laser profile does not exactly match the fundamental TE mode of the 1 μm guide. One way to mitigate this is to introduce an adiabatic taper or spot-size converter that gradually widens the core to 3-4 μm before the functional section. In this way, the optical field is still confined in the fundamental mode, and its transverse profile widens smoothly, gradually matching its shape and numerical aperture to those of the fiber or external source. The result is greater modal overlap, which in theory should reduce insertion loss to < 0.2 dB [173, 174].

Another probable problem is due to reflection, given that the Air interface $n_{Air} = 1$ and in the a-Si:H waveguide, n = 3.48, the normal reflection deduced from equation 2.10 is R=0.306, which means that the a-Si:H waveguide may reflect approximately 30.6% of the incident power.

An effortless way to mitigate these losses that are compatible with CMOS processes is to deposit a thin Anti-Reflective (AR) thin film with an intermediate index on the facet or on the grating coupler itself. Standard materials are Si_3N_4 ($n \approx 2.0$) or SiO_xN_Y ($n \approx 1.9$). If the thickness of the film is adjusted to $\lambda/4$ at the operating wavelength of 1.55 µm, destructive interference is obtained for the reflected wave, reducing the reflectance to values below 0.5% (<0.05 dB). This improves the power budget of the link and prevents optical feedback to the source [146, 147]. In our design, this solution was implemented with a Si_3N_4 layer with L=0.2 µm, and the result was almost imperceptible. The increase up to L=0.5 µm was analyzed, and the result for higher values was a higher IL.

Another problem detected in the design relates to losses caused by transient thermodynamic mismatch, which varies between 0.30 dB and 0.7 dB per interface, in segments L1 and L2. The temperature-induced index gradient Δn expands the mode slightly and shifts its optical center; when the beam propagates again in a cold zone, this profile no longer coincides with the undisturbed fundamental mode since, although small, the index propagates from a higher index to a lower one. The result is that part of the power is coupled to radiated or higher modes, and another part is reflected, causing additional insertion loss as shown in Figure 4.18 for $\Delta x_1 \approx 0.066$ and $\Delta x_2 \approx 0.108$.

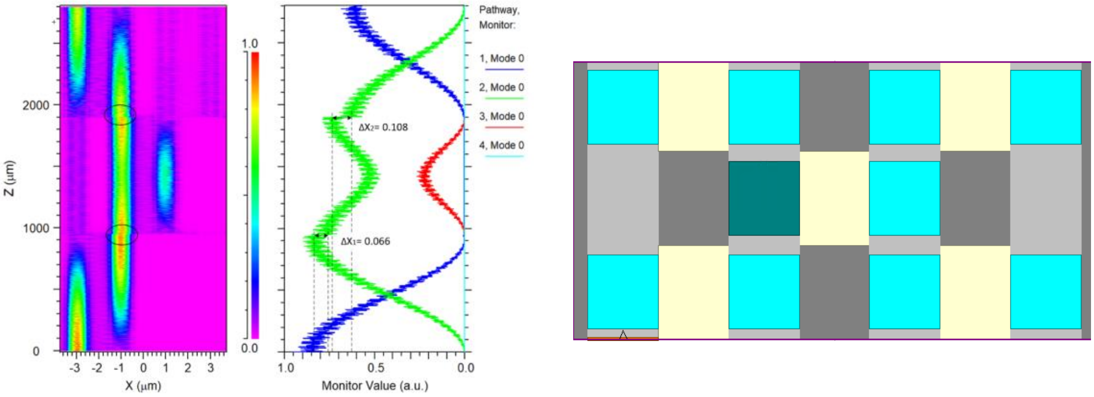

Figure 4.18 – Evolution of the fundamental TE mode on the z-axis in a 1x1 configuration and the top view with the heater active (dark cyan).

In terms of optical power, the values obtained in the simulations for each input port/output port combination of the 4X4 matrix are shown in Table 4.2. The values shown in the table depend on the configuration used, as well as the losses mentioned above, with insertion losses having a particularly significant impact.

Table 4.2 – Optical power levels for each input/output combination.

Input port	Output port 1	2	3	4
1	0.65	0.65	0.70	0.70
2	0.70	0.72	0.65	0.65
3	0.65	0.72	0.73	0.70
4	0.65	0.65	0.67	0.65

4.4 4×4 Programmable PIC Matrix Based on Amorphous Silicon Using the Carrier Depletion Phenomenon

In earlier sections, we analyzed how the plasma effect changes the optical parameters when the material is doped with impurities (n-type or p-type). In MOS-type configurations, including their applications, we highlight the advantages of carrier accumulation modulators, which stand out for their efficiency, speed, and low losses. However, once the principles of these techniques have been analyzed in the case of carrier accumulation, it is not practical as a control technique in low-loss routers, since an oxide barrier increases attenuation in the guide with length. On the other hand, when using the accumulation technique to dope the material with p-type carriers, the majority carriers (holes +) have greater absorption, and their reduced mobility penalizes both optical loss and speed. When a negative potential is applied to the MOS electrode for accumulation, the effective index decreases. This same technique is applied, as we saw earlier, in Pockels-type modulators.

On the other side, continuing with the same technique when doping the material with n-type carriers, when applying a positive potential V>0 in MOS configuration, the majority carriers (electrons -) accumulate at the oxide-semiconductor interface. This increase in electrons introduces a negative dispersive perturbation, causing N_{eff} to decrease, while at the same time increasing absorption to lower values compared to p-type, but still considerable at high voltages. In both cases, the value of N_{eff} decreases when a positive voltage is applied to the electrode, which, when doping the material, decreases in comparison with the intrinsic value due to the plasma effect analyzed in equations 2.51 and 2.52.

In our proposed design for a 4X4 Programmable PIC Matrix Based on Amorphous Silicon Controlled by Carrier Depletion Phenomenon, a similar structure will be used, guided by a doped a-Si:H core. Due to the advantages in terms of mobility and losses, we selected n-type doping and, as the mode of operation within the Free-Carrier Plasma Dispersion Effect (FCPDE) techniques, the depletion mode.

In general, the mode of operation is that when a negative potential V< 0 is applied to the electrode, a depletion region is generated that expels the majority carriers (electrons -) from the guide-oxide region, thus raising the effective index to a value close to the intrinsic value. When the potential is no longer applied to the electrode, the electric field disappears, for V = 0, and the electrons rearrange themselves from the volume to the interface; this refilling, limited by their mobility and the structure of the semiconductor lattice, gradually restores the initial carrier concentration, thus restoring the N_{eff} value to its lowest value. This method also includes more losses due to absorption, but to a lesser extent than in the accumulation mode. By replicating this principle in the different segments of the matrix to control the variation of N_{eff} as well as the phase distribution, it is possible to dynamically control the trajectory of light within the programmable photonic network. This control strategy simultaneously improves the phase/absorption ratio, reduces switching power, and keeps compatibility with standard CMOS processes, making it workable for our proposal.

Figure 4.19 shows the 2D front view and segments of guides 1 and 2, the materials used, and their dimensions.

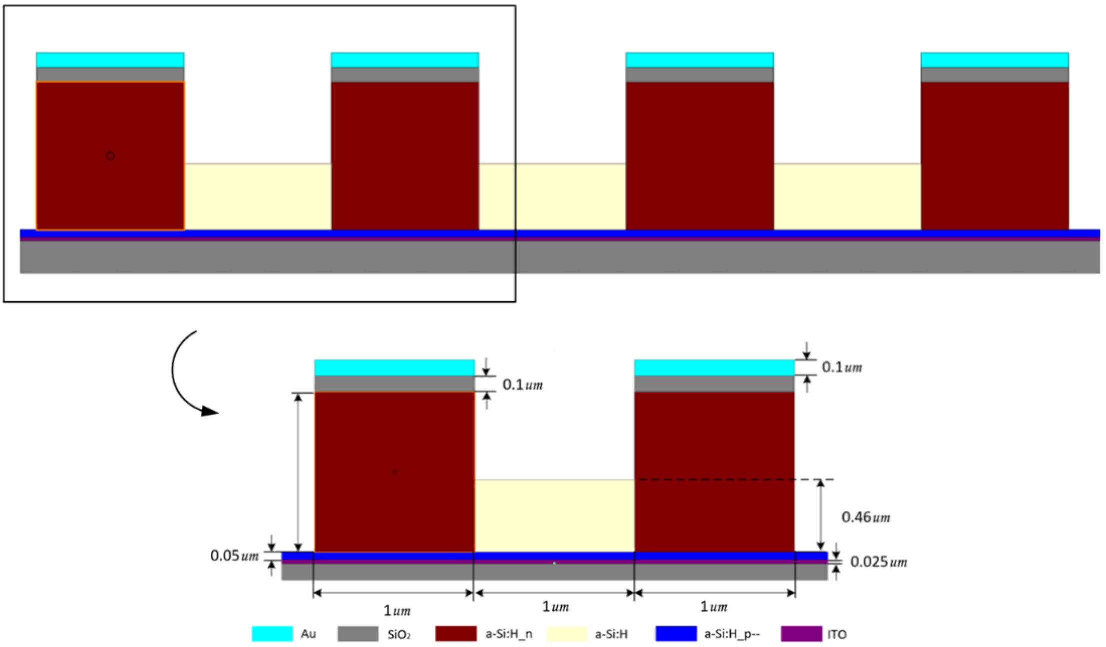

Figure 4.19– 4X4 Programmable PIC Matrix Based on Amorphous Silicon Controlled by Carrier Depletion Phenomenon, front view, dimensions and materials

As we can see in Figure 4.20, this is a top view of the proposed matrix and its dimensions. It is worth noting that the design of the slab between guides consists of an intrinsic a-

Si:H guide. This is because when the N_{eff} level is lowered, the original state in the doped guides does not transfer optical power.

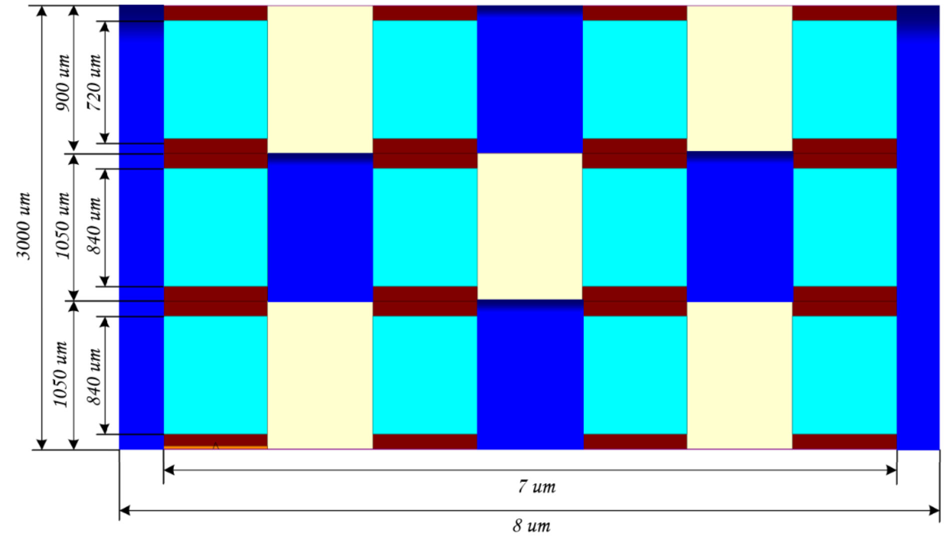

Figure 4.20 – Top view of the matrix and its longitudinal segments.

In the case of the TOE, applying the temperature variation in the heaters to $\Delta T = 15K$ caused a variation of $\Delta n_{eff} = 0.00138$, sufficient to break the modal equilibrium in the heated guide, thus confining the light within it. With this analysis, we aim to decrease the effective index N_{eff} of the guide due to the plasma effect, causing a variation of $-\Delta n_{eff} = 0.00138$. And by applying V < 0 with an n-type doped core, due to depletion, increase the value of N_{eff} to the intrinsic value, thus controlling the switching between the Horn-Slab Directional Coupler type couplers. For this purpose, a repository in Python named "*Calculation_doping_concentration*" was created on GitHub to estimate the doping level referring to the desired refractive index variation. This script is based on equations 2.50 and 2.51 and is available in [175].

To estimate the level of doping, it is necessary to know the value of N_{eff} and the value of the desired reduction in N_{eff}, as well as the confinement factor in the guide. By default, we assume Γ = 1. This can be done analytically using the previous scripts, in this case already knowing the desired reduction variation $\Delta n_{eff} = 0.00138$. and by calculating modes with the FEMSim tool, we obtained an intrinsic value of $n_{eff} = 3.492873$ for TE_{00}. When calculating using the Calculation_doping_concentration script, the following electron concentration was obtained for the doping of the material with a value of $\Delta \mathrm{N_e} = 1.163\mathrm{e}18$. Once the doping was calculated, the N_{eff} value was analyzed again using the FEMSim tool, resulting in this doping level for $n_{eff} = 3.491321$ for a variation of $\Delta n_{eff} = 0.001552$, which is a good prediction. However, by adjusting the carrier values, we obtained a closer approximation for a concentration at $\Delta \mathrm{N_e} = 1\mathrm{e}18$, with a value of $n_{eff} =$

3.491471 and a variation of $\Delta n_{eff} = 0{,}001402$, this doping level and their electron density can be seen in Figure 4.21.

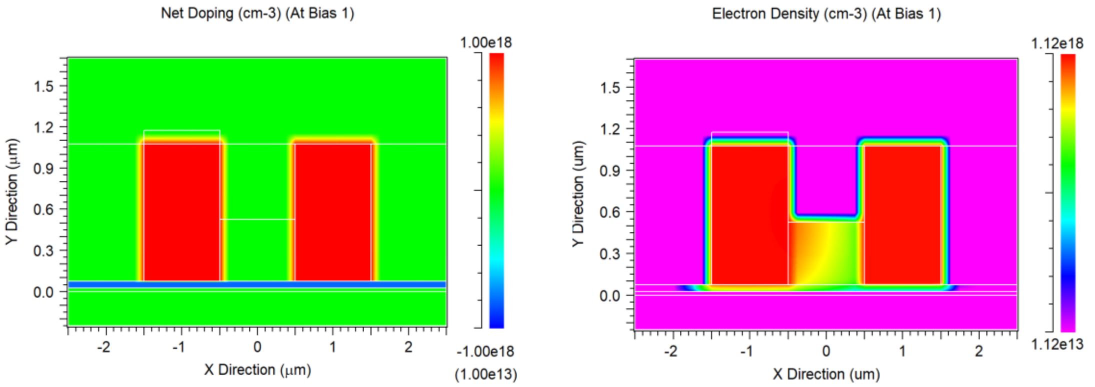

a) b)

Figure 4.21 – Analysis of the n-type doping level: a) doping level in the main guide, b) electron density.

Once the necessary doping level has been obtained, we analyze which potential value causes an increase in N_{eff}, in the same proportion as the doping level decreases it. In this way, by applying potential to the electrode, we obtain a value remarkably close to the intrinsic level. For this scenario, various simulations were performed, with the best result being a value of -1.13V, as shown in Figure 4.2.

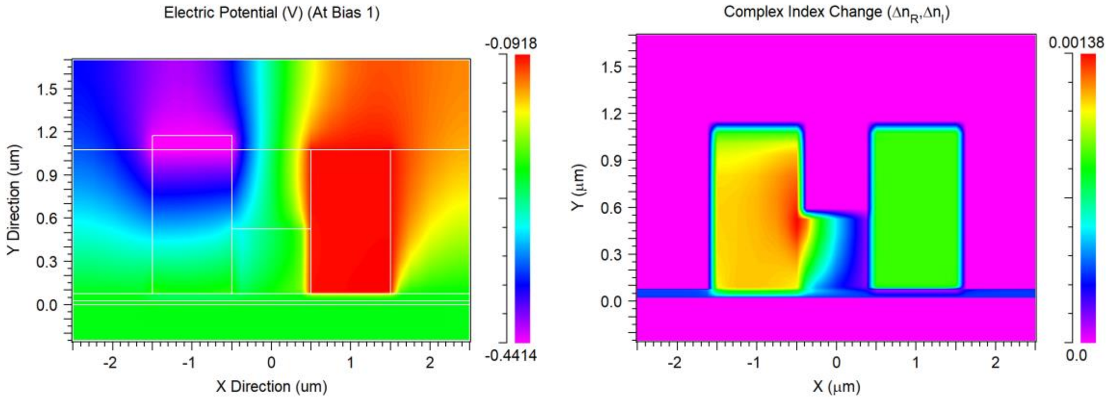

a) b)

Figure 4.22 – Analysis of depletion mode with n-type carriers: a) electric potential applied, b) variation of the refractive index due to the applied potential.

Values between -1.1V and -1.2V can also be considered, given that the variation obtained is $\Delta n_{eff} = 0.0013$ and $\Delta n_{eff} = 0.00156$ respectively, which are values close to the intrinsic N_{eff}.

When analyzing the electrical profile in Figure 4.23, we can see in a) the current vs. voltage graphs where, in the section close to -0.7 to 0 V, the current is practically zero, and at -1.13 V it is conducting, as confirmed in b) where the resistance is almost 0, this is because, when the bias is made more negative, where $|I|$ grows rapidly, in accordance with Shockley's equation [32], where in reverse the current saturates and in forward it grows almost exponentially.

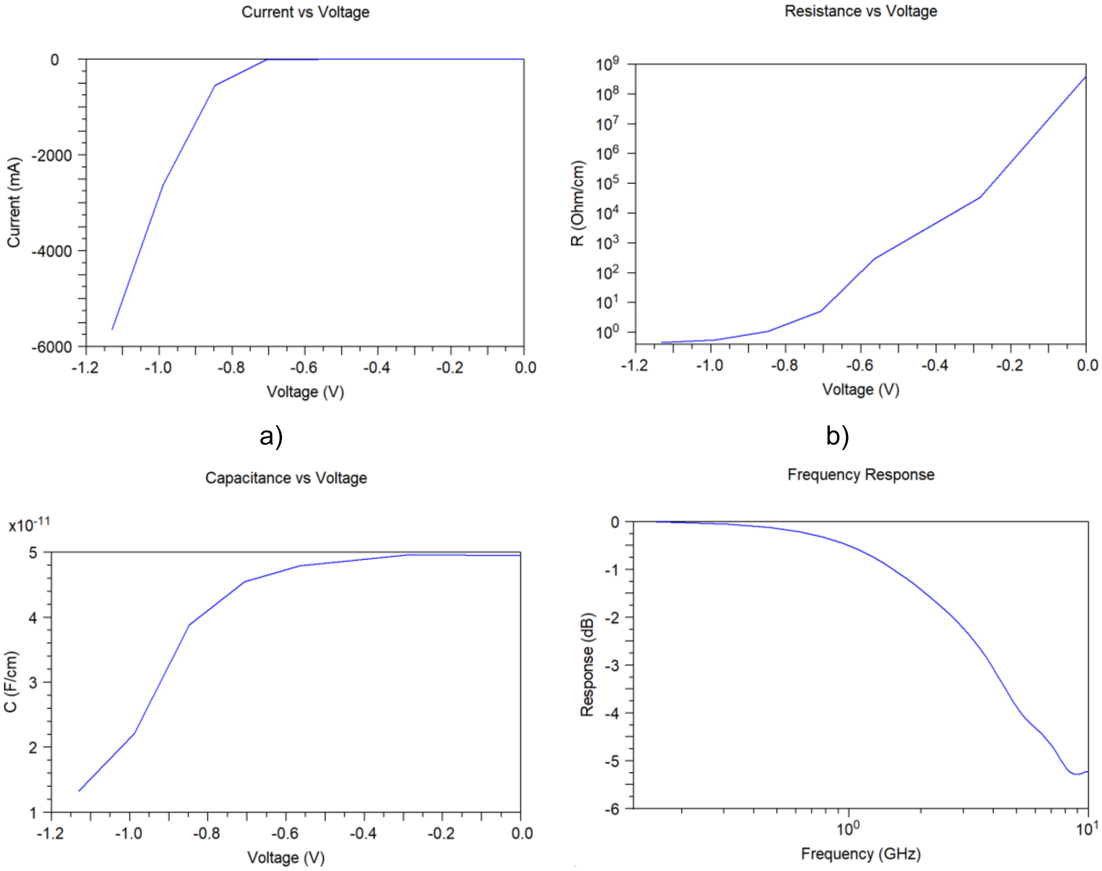

a) b)

c) d)

Figure 4.23 – Electrical characterization: a) current vs voltage, b) resistance vs voltage, c) capacitance vs voltage, and d) frequency response.

In the case of capacitance in Figure 4.23.c), the capacitance decreases from 0 V to −1.13 V, as expected in a reverse junction in $f_{3dB} \sim 3\text{Ghz}$, typical of an RC limit, the slight ripple towards 10 GHz points to parasites generated by internal currents and the RC system at high frequency response.

As mentioned above, when increasing the doping level in a-Si:H guides with n-type doping, with electrons as the majority carriers, the refractive index at this level will decrease slightly, caused by the doping of free carriers (electrons) which introduce a negative dispersive contribution accompanied by an increase in attenuation, as analyzed analytically in the Drude model equations. It is worth noting that the doping profile distribution we adopted for this carrier analysis is homogeneous throughout the entire section of the a-Si:H guide, which simplifies the optical-electrical modeling of the matrix and allows us to isolate the effect of free carriers on N_{eff}. However, there are strategies focused on studying the behavior of carrier mobility and its advantages, mainly used in modulators and phase shifters, as well as combined doping techniques for the same waveguide, as seen in the images of the modulators for the different methods of Free-Carrier Plasma Dispersion Effect (FCPDE) in topic 2.5.2. It remains to be analyzed other doping distributions as well as other doping configurations.

In general, the sections of our matrix function when a DC electric field is applied to the electrodes in the selected segments in the guide (MOS configuration), which allows the N_{eff} to increase to its intrinsic value through depletion, enabling the signal to be transferred directly. Light will only propagate efficiently when the electrodes are active, since if we send a signal through an unstimulated guide in its normal (doped) state, the absorption levels are higher, so part of the power would be lost, as seen in Figure 4.24 a). To obtain power transfer between guides (PCross), it is necessary for both guides to be excited, as can be seen in b), emulating the same behavior they had in the case of the thermo-optic effect, only in this case, to contain it, it is only necessary to activate the electrode through which the light will propagate. In other words, electrodes control the optical path.

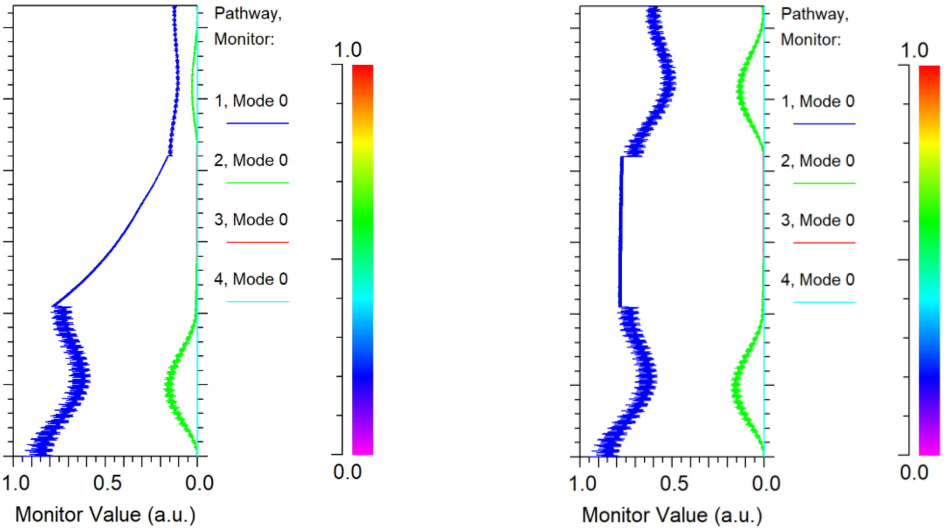

a) b)

Figure 4.24 – Evolution of the fundamental TE mode on the z-axis in a 1x1 configuration, a) using as 1A active electrode, b) using 1A-1B-1C as active electrodes.

Always improving the route that requires the fewest electrodes to be activated, like the matrix designed for the TOE effect, a state map is presented for the different route options for a given input and a desired output, as shown in Figure 4.25.

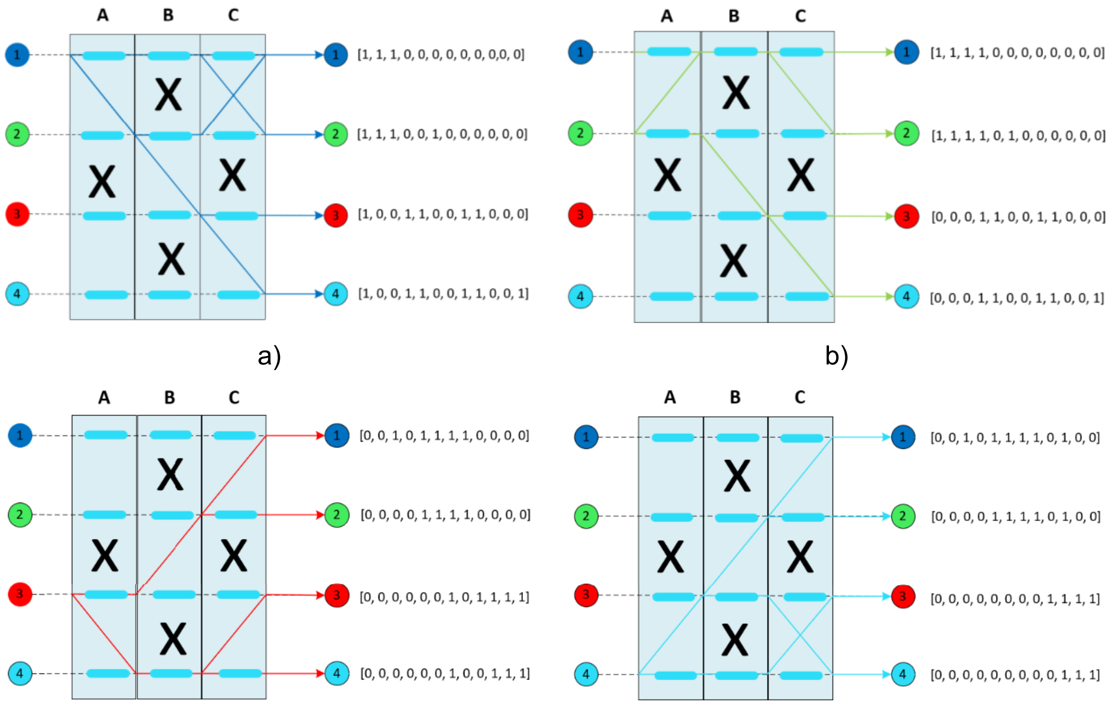

a) b) c) d)

Figure 4.25 – State map used in the 4X4 programmable PIC matrix, a) 1x4 configuration, 2x4 configuration, c) 3x4 configuration, d) 4x4 configuration.

Based on the earlier route configurations, Figure 4.26 shows the results of the propagation evolution on the z-axis for each of the 1X4 configurations given in Figure 4.25 a).

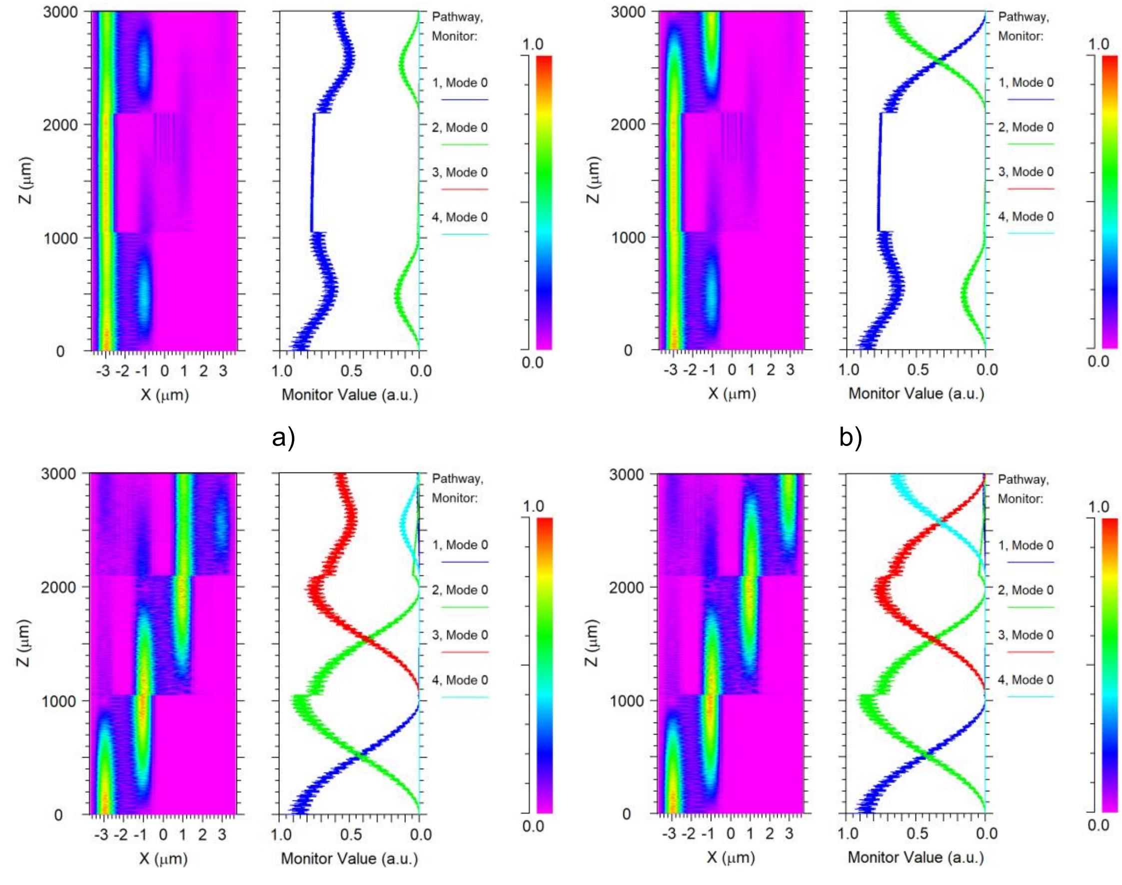

a)

b)

c)

d)

Figure 4.26 – Evolution of the fundamental TE mode on the z-axis in: a) 1x1 configuration, b) 1x2 configuration, c) 1x3 configuration, d) 1x4 configuration.

Figure 4.27 shows the evolution of the fundamental TE mode on the z-axis for each of the combinations from input two and their combinations at the output for the first configuration referred to in Figure 4.25 b).

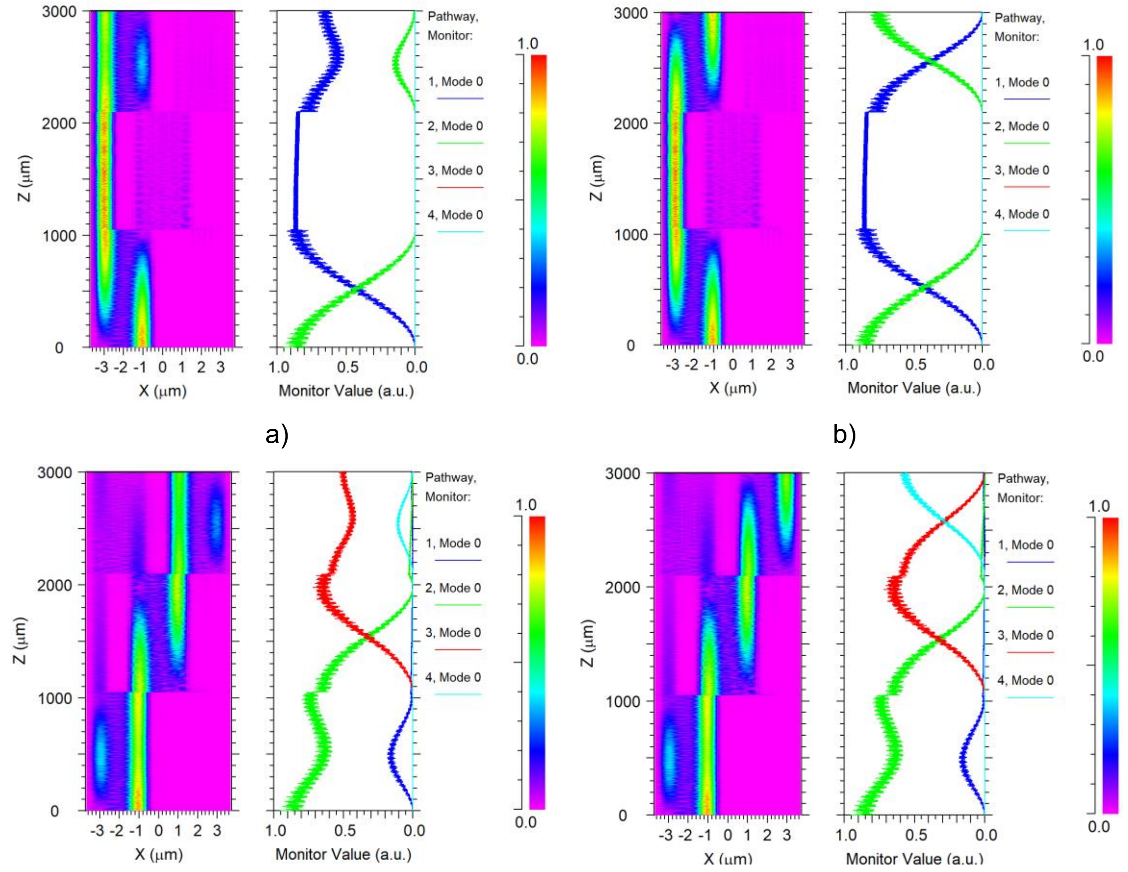

a) b) c) d)

Figure 4.27 – Evolution of the fundamental TE mode on the z-axis in: a) 2x1 configuration, b) 2x2 configuration, c) 2x3 configuration, d) 2x4 configuration.

Figure 4.28 shows the evolution of the fundamental TE mode on the z-axis for each of the combinations of the input three and their combinations at the output for the first configuration referred to in Figure 4.25 c).

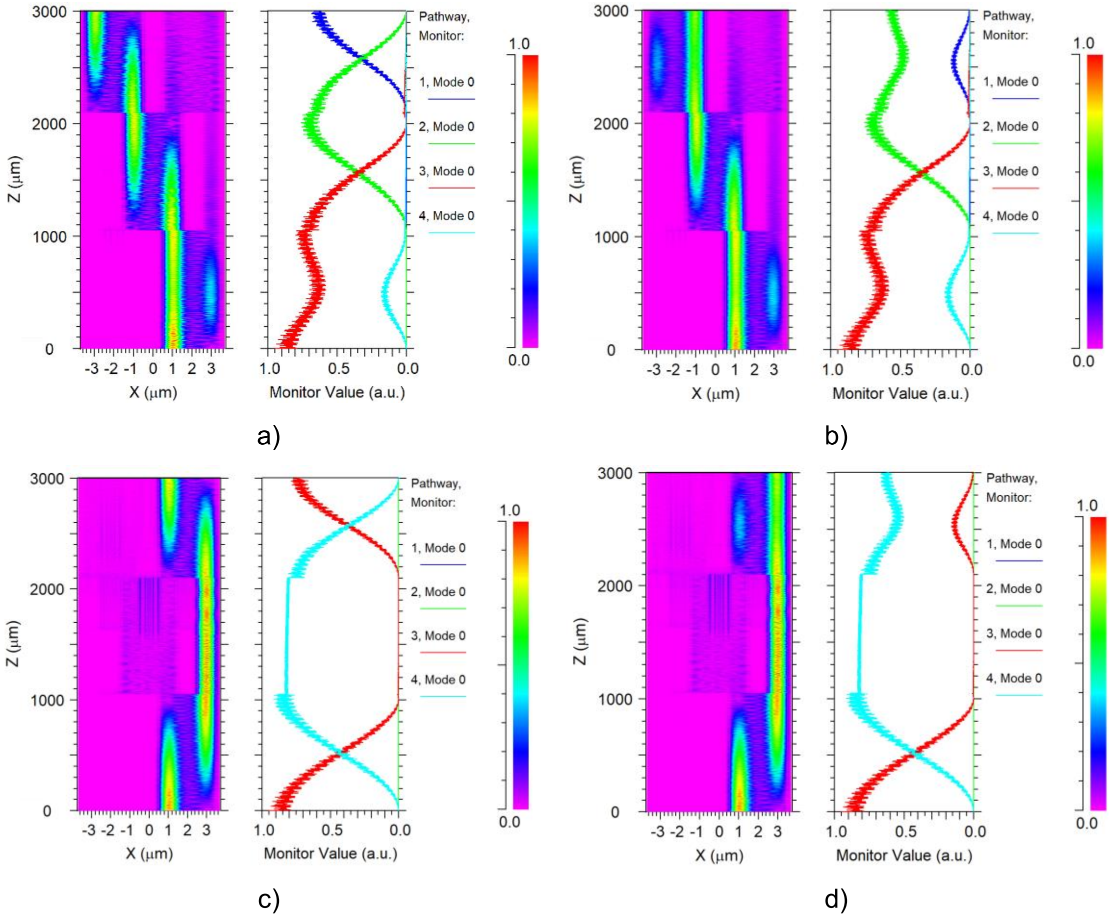

a) b) c) d)

Figure 4.28 – Evolution of the fundamental TE mode on the z-axis in: a) 3x1 configuration, b) 3x2 configuration, c) 3x3 configuration, d) 3x4 configuration.

Figure 4.29 shows the evolution of the fundamental TE mode on the z-axis for each of the combinations from input one and their combinations at the output for the first configuration referred to in Figure 4.25 d).

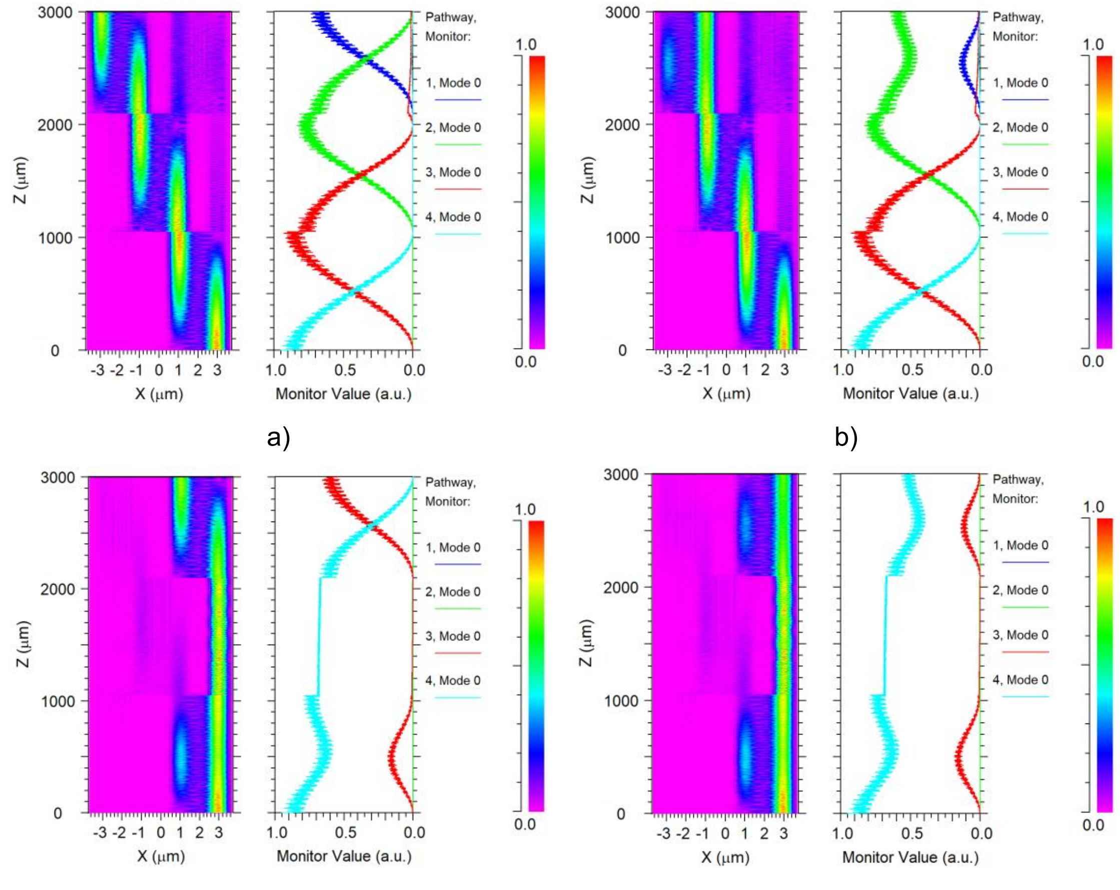

a) b)

c) d)

Figure 4.29 – Evolution of the fundamental TE mode on the z-axis in, a) 4x1 configuration, b) 4x2 configuration, c) 4x3 configuration, d) 4x4 configuration.

Table 4.3 shows the optical power values obtained in the simulations for each input port/output port combination of the 4X4 matrix. The values depend on the configuration used and the losses mentioned above, including the absorption and insertion losses.

Table 4.3 – Calculated power and voltage parameters for the gold resistive heater.

	Output port			
Input port	1	2	3	4
1	0.58	0.68	0.55	0.63
2	0.65	0.75	0.52	0.57
3	0.65	0.56	0.72	0.63
4	0.65	0.60	0.60	0.52

4.4.1 Applications

The device presented above consists of a 4X4 matrix based on a 2X2 silicon horn switch block structure, based on coupled mode theory, with the particularity that the solution offered is valid for values of separation between guides greater than 0. In our case, it was designed at 1 μm, using these directional couplers and electrodes as control elements, which, using the thermo-optic and carrier accumulation effects, make it possible to program the desired 1XN outputs in each case. These characteristics allow our device to be classified as a programmable optical switch for light manipulation, which can be used to implement optical signal routing and switching. Adding a modulation stage to the device output makes it possible to obtain a multi-position modulation circuit in optical transceivers. The switch can function as a dynamic routing element for modulated optical signals in transceivers [176]. By incorporating modulation elements such as advanced MZI modulators into the outputs of the prototype interfaces, integration with advanced schemes such as QPSK or 16-QAM is possible. In communications applications, especially in systems with DWDM technology for large data centers, our device behaves like an optical router, since it can dynamically select one or more wavelengths from an input, routing each channel to different outputs without electro-optical conversion, enabling real-time routing. These devices are highly scalable, reaching a high radix 128X128 silicon photonic single chip switch fabric with a tolerable power penalty [177, 178, 179]. In Artificial Neural Networks (ANNs) applications, reconfigurable photonic networks can implement linear matrix operations, the computational core of neural networks. Our device is scalable and can be used to perform matrix-vector multiplication (dot product) between optically encoded weights and modulated inputs, as well as having practical use in the implementation of linear (or convolutional) layers in deep networks [180, 18]. The ability to program a 4x4 mesh enables on-the-fly reconfiguration of optical networks, changing logical topologies such as mesh, ring, or star without physical hardware changes. This is essential in optical Network-On-Chip (NoC) applications [18]. When used as a distributed and selective optical sensor, our prototype integrated with Fiber Bragg Grating (FBG) networks or ring resonators is used for selective sensor interrogation, minimizing crosstalk and improving spatial resolution in distributed detection platforms [181].

5 Conclusions and future work

In this chapter, we will answer the main questions raised in section 1.2 of chapter 1, after having developed the work and presented several solutions.

Regarding the optimization of the coupler in the proposed structure for a horn-slab directional coupler, we first demonstrated that it is possible to couple two parallel waveguides for a distance of $s = 1\ \mu m$. In the analysis performed for a slab height of 0.46 μm, we were able to simulate that this structure allows coupling up to $s \leq 1.3\ \mu m$. As demonstrated in the analysis in Figure 3.7 and Figure 3.9, the coupling depends on both s and L, although the s factor is the determining factor.

At this distance, the guides couple through the evanescent field that propagates through the slab, with the slab itself being the medium. Therefore, in solutions such as those we saw for the thermo-optic effect and the carrier depletion phenomenon, it is sufficient to remove the slab, and the guides will not propagate. This results in a system that does not depend on S-bends to bring the guides closer together for coupling, significantly improving lithography's efficiency and error margin. This makes the manufacturing process more straightforward, efficient, and compact since this strategy significantly minimizes the design dimensions.

In response to the problem of thermal crosstalk, having a greater separation and the slab being below the center of the guide, it was verified that the thermal transfer between guides is significantly reduced, as can be seen in Figure 4.9, which is much lower than in conventional couplers analyzed in Figure 4.3. It should also be mentioned that in the proposed solution for the horn-slab directional coupler, much less temperature was required to confine the light in the guide, only a variation for ΔT=15K compared to the ΔT=35K used to obtain the same result in the conventional coupler. These results can be seen in Figures 4.10 and 4.2, respectively.

One of the main advantages of a-Si:H is its ease of production. As mentioned above, it is deposited at low temperatures (≈100–400 °C) by PECVD or other previously discussed techniques, allowing guides to be added after the CMOS front-end or in 3D stacks (MOS). During the analysis conducted in this work, it was proven that it is possible to create scalable and compact solutions using it as the primary material. As we discussed in Chapter 2, amorphous silicon has low losses and a refractive index greater than silicon at λ=1.55 μm, making it an excellent choice for applications that require good light confinement, such as waveguides.
In addition, a-Si:H waveguides are thermally stable, making them a satisfactory solution when implemented in thermo-optical control designs.

When used as the main element in Free-Carrier Plasma Dispersion Effect (FCPDE) solutions, the crystalline structure of a-Si:H, being random and using hydrogen as a stabilizing element, creates a kind of trap in the added carriers (doping), resulting in lower mobility than crystalline silicon. This lower mobility increases RC values and carrier losses, so IL rises and bandwidth or frequency response decreases.

Future work is proposed to keep a-Si:H as a passive guide or TOE solutions and perform a pn junction in c-Si (SOI windows) to maximize speed and minimize absorption.

When analyzing both solutions from an energy efficiency standpoint, we will first examine the amount or level of potential used in each case. In the case of TOE, to reach ΔT=15K in each heater, 0.05V is needed, while for CDP, -1.13V is needed. Regarding energy dissipation, TOE is based on temperature, while CDP is based on carrier movement. Therefore, the latter does not generate temperature between state changes, making CDP more efficient in thermal dissipation. In terms of active elements, TOE uses fewer elements than CAD, using a maximum of two elements per route. At the same time, CAD practically performs the routing by activating the electrodes, requiring a maximum of six elements in a route. The IL and PL values are shown in Table 5.1, as an analysis of the parameters analyzed in both solutions.

Table 5.1 – Comparison between 4X4 matrix solutions

Technique	Potential [V]	Temperature	Active Elements	IL (dB)	PL (dB)
TOE	0.05	Low	2	0.7	0.661-1.165
CDP	-1.13	-	6	0.7	0.544 - 2.134

Given the limitations of theory and simulation analysis, to obtain better characterization, it is first necessary to construct both solutions and then perform tests to get better results.

Therefore, as future work, we propose the construction of these devices and, under laboratory testing, the analysis of key performance parameters such as speed/BW, extinction ratio (ER), stability, and those we have presented above.

Future work also proposes developing a control interface that automates the activation of the electrodes in the 4×4 matrix in both the thermo-optic (TOE) and carrier depletion (CDP) versions. This strategy can be implemented using a machine learning layer capable of activating these electrodes using given input and output values as a desired function. For a more complete solution, this interface would implement a system of optical sensors at the outputs to adjust the power of the heaters (TOE) or the voltage of the pn junctions (CDP), this being an active feedback stage capable of self-calibrating to correct manufacturing variations. In the case of TOE, the use of a bus for frequent paths due to the on/off time between heaters. This machine learning-assisted optimization will reduce consumption (mW/FSR in TOE, switching energy in CDP), thus keeping low losses and greater isolation between ports.

Bibliography

[1] W. Shockley, "The path to the conception of the junction transistor," *IEEE Transactions on Electron Devices,* vol. 31, nº 11, 1984.

[2] A. Ahmad, A. B. S. S, A. Al-Maashri, M. Awadalla e S. Hussain, "FPGAs–Chronological developments and challenges. International Journal of Electrical Engineering & Technology," *International Journal of Electrical Engineering & Technology,,* vol. 12, nº 11, pp. 60-72, 2021.

[3] W. Tian, Y. Wang e Dang, "Photonic Integrated Circuits: Research Advances and Challenges in Interconnection and Packaging Technologies," *Photonics,* vol. 12, nº 8, p. 821, 2025.

[4] D. Y.-H. Chang, "idtechex," 7 02 2025. [Online]. Available: https://www.idtechex.com/en/research-report/silicon-photonics-and-photonic-integrated-circuits-2025-2035-technologies-market-forecasts/1067. [Acedido em 24 08 2025].

[5] A. Shivarkar, "Precedence Research," 11 06 2025. [Online]. Available: https://www.precedenceresearch.com/photonic-integrated-circuit-market. [Acedido em 24 08 2025].

[6] J. Capmany e D. Pérez, Programmable Integrated Photonics, Oxford University Press, 2020.

[7] B. E. Saleh e a. M. C. Teich, Fundamentals of Photonics, Hoboken, New Jersey: John Wiley & Sons Inc, 2019.

[8] A. Totovic1, G. Giamougiannis, A. Tsakyridis, D. Lazovsky e N. Pleros, "Programmable photonic neural networks combining WDM with coherent linear optics," *Nature,* vol. 12, nº 5605, 2022.

[9] G. N. N. a. V. Sadasivan, "Broadband tunable basic units for nonvolatile field programmable photonic gate array," *Journal of the Optical Society of America B,* vol. 40, nº 5, pp. 1054-1062, 2023.

[10] J. Hertz, "allaboutcircuits.com," PCBWay, 03 08 2022. [Online]. Available: https://www.allaboutcircuits.com/news/ipronics-launches-era-of-programmable-photonic-processors/. [Acedido em 25 08 2025].

[11] M. AbuGhanem, "Information processing at the speed of light," *Frontiers of Optoelectronics,* vol. 17, nº 33, 2024.

[12] M. Blahut e D. Kasprzak, "Multimode interference structures-properties and applications," *Optica Applicata,* vol. 34, nº 4, pp. 573-587, 2004.

[13] P. P. Sahu, "Multimode interference coupler based on general interference for integrated optical and quantum optic devices: a review," *Physica Scripta,* vol. 99, nº 8, pp. 85-106, 2024.

[14] Y. R. Bawankar e A. Singh, "Microring Resonators Based Applications in Silicon Photonics - A Review," em *5th Conference on Information and Communication Technology (CICT)*, 2021.

[15] X. e. a. Liu, "A compact on-chip computational spectrometer using reconfigurable silicon micro-ring optical filtering network.," *Optics Communications,* p. 132227, 2025.

[16] L. e. a. ZHUANG, "Programmable Photonic Signal Processor Chip for Radiofrequency," *Optica,* vol. 2, nº 10, pp. 854-859, 2015.

[17] D. Perez, I. Gasulla, J. Capmany e R. A. Soref, "Reconfigurable lattice mesh designs for programmable photonic processors.," *Optics express,* vol. 24, nº 11, pp. 12093-12106, 2016.

[18] W. Bogaerts, D. Pérez, J. Capmany, D. A. B. Miller, J. Poon, D. Englund e F. M. &. A. Melloni, "Programmable photonic circuits," *Nature,* nº 586, pp. 207-216, 2020.

[19] B. D. a. D. S. Guenther, Encyclopedia of modern optics, Second Edition ed., vol. 1, Academic Press, 2018.

[20] W. Bogaerts, "Programmable photonics." Optics and Photonics News," *Optics and Photonics News,* vol. 35, nº 3, pp. 34-41, 2024.

[21] S. Liu, J. Feng, Y. Tian, H. Zhao, L. Jin, B. Ouyang, J. Zhu e J. Guo, "Frontiers of Optoelectronics," *Thermo-optic phase shifters based on silicon-on-insulator platform: state-of-the-art and a review,* 12 04 2022.

[22] A. Hardy e a. W. Streifer, "Coupled Mode Theory of Parallel Waveguides," *Journal of lightwave technology,* vol. 3, nº 5, pp. 1135-1146, 1985.

[23] K. Jonathan, Z. Hongwei, S. Bowen, L. Yuan, I. Brandon, P. Sergio, S. Fengqiao e C. Larry, "Indium Phosphide Photonic Integrated Circuits: Technology and Applications," em *IEEE BiCMOS and Compound Semiconductor Integrated Circuits and Technology Symposium (BCICTS)*, San Diego, CA, USA, 2018.

[24] P. R. A. Binetti, M. Lu, E. J. Norberg, R. S. Guzzon, J. S. Parker, A. Sivananthan, A. Bhardwaj, L. A. Johansson, M. J. Rodwell e L. A. Coldren, "Indium Phosphide Photonic Integrated Circuits for Coherent Optical Links," *IEEE Journal of Quantum Electronics,* vol. 48, nº 2, pp. 279-291, 2012.

[25] S. Mookherjea, V. Mere e F. Valdez, "Thin-film lithium niobate electro-optic modulators: To etch or not to etch," *Applied Physics Letters ,* vol. 122, nº 12, p. 120501, 2023.

[26] G. Chen, J. D. N. Nanxi Li, H.-L. Lin, Y. Zhou, Y. H. Fu, L. Y. T. Lee, Y. Yu, A.-Q. Liu e A. J. Danner, "Advances in lithium niobate photonics: development status and perspectives," *Advances Photonics,* vol. 4, nº 3, 2022.

[27] A. Boes, L. Chang e C. Langrock, "Lithium niobate photonics: Unlocking the electromagnetic spectrum," *Science,* vol. 379, nº 6627, 2023.

[28] V. P. A, W. Lei, F. Joseph, S. Fengqiao, R. Victoria, N. Michael, Y. Guangning, S. Mark, C. Larry e K. Jonathan, "Gallium Arsenide Photonic Integrated Circuit Platform for Tunable Laser Applications," *IEEE Journal of Selected Topics in Quantum Electronics,* vol. 28, nº 1, pp. 1-9, 2022.

[29] J. Koester, O. Brox, H. Wenzel, J. Fricke, P. Casa, A. Maaßdorf e A. Knigg, "Toward complex GaAs PIC-based laser sources," em *Conference on Lasers and Electro-Optics/Europe (CLEO/Europe 2023) and European Quantum Electronics Conference (EQEC 2023)*, Munich, DE - Germany, 2023.

[30] P. C. Safa Kasap, Handbook ok Electronic and Photonic Material 2nd Edition, Saskatoon, Canada: Springer, 2017.

[31] J. M. Siqueiros, L. E. Regalado e a. R. Machorro, "Determination of (n,k) for absorbing thin films using reflectance measurements," *Applied Optics,* vol. 27, nº 20, pp. 4260-4264, 1988.

[32] S. J. Ling, J. Sanny e W. Moebs, Física Universitaria, Houston, Texas: OpenStax, 2021.

[33] C. Hu, K. Guo, Y. L, Z. G. J. Quan e S. Z. a. W. Zheng, "Optical coatings of durability based on transition metal nitrides," *Thin Solid Films,* vol. 688, nº 137339, 31 10 2019.

[34] S. Adachi, Optical properties of crystalline and amorphous semiconductors: Materials and fundamental principles, Maebash, Japan: Springer Science & Bussines Media , 2012.

[35] J. Steinlechner, I. W. Martin, A. S. Bell, J. Hough, M. Fletcher, P. G. Murray e R. ... & Schnabel, "Silicon-based optical mirror coatings for ultrahigh precision metrology and sensing," *Physical Review Letters,* vol. 120, nº 26, p. 263602, 2018.

[36] S. Fang, Z. Lu, X. Ji, H. Jiao, X. Cheng, Z. Wang e J. Zhang, "High-performance hydrogenated amorphous silicon deposited by ion-beam sputtering for gravitational-wave detectors," *Physical Review D,* vol. 108, nº 6, p. 062002, 2023.

[37] S. Z. Oo, A. Tarazona, A. Z. Khokhar, R. Petra, Y. Franz, G. Z. Mashanovich, G. T. Reed, A. C. Peacock e H. M. H. Chong, "Hot-wire chemical vapor deposition low-loss hydrogenated amorphous silicon waveguides for silicon photonic devices," *Photonics Research,* vol. 7, nº 2, pp. 193-200, 2019.

[38] M. H. Francombe, "Methods of Deposition of Hydrogenated Amorphous Silicon for Device Applications," *ResearchGate,* vol. 30, pp. 1-215, 2002.

[39] P. Roca i Cabarrocas, "Amorphous Films, Plasma Enhanced Chemical Vapor Deposition," em *Encyclopedia of Materials: Science and Technology*, 2001, pp. 157-160.

[40] D. Tsai, H. S., Z. L, W. C. Chang e S. Chao, "Amorphous silicon nitride deposited by an NH3-free plasma enhanced chemical vapor deposition method for the coatings of the next generation laser interferometer gravitational waves detector," *Classical and Quantum Gravity,* vol. 39, nº 15, p. 15LT01, 2022.

[41] J. Gope, S. Kumar, A. Parashar, P. Dixit, C. Rauthan, O. Panwar e D. P. a. S. Agarwal, "Amorphous and nanocrystalline silicon made by varying deposition pressure in PECVD process," *Journal of Non-Crystalline Solids,* Vols. %1 de %245-47, nº 355, pp. 2228-2232, 2009.

[42] K. Lau, H. P. Lewis, S. Limb, M. Kwan e K. Gleason, "Hot-wire chemical vapor deposition (HWCVD) of fluorocarbon and organosilicon thin films," *Thin Solid Films,* vol. 395, nº 1-2, pp. 288-291, 2001.

[43] E. Hemsley, D. Bonneau, J. Pelc, R. Beausoleil e J. L. O'Brien, "Photon pair generation in hydrogenated amorphous silicon microring resonators," *Nature,* vol. 6, nº 38908, 2016.

[44] M. J. Madou, Fundamentals of microfabrication and nanotechnology, three-volume, CRC Press, 2018.

[45] A. M. Agarwal e J. Michel, "Amorphous Silicon in Microphotonics," em *Springer Handbook of Glass*, Springer Handbooks, 2019, pp. 1483-1493.

[46] M. Polyanskiy, "refractiveindex.info database of optical constants.," 2024. [Online]. Available: https://refractiveindex.info/?shelf=main&book=Si&page=Franta. [Acedido em 05 08 2025].

[47] D. Franta, D. Nečas, L. Zajíčková, I. Ohlídal e a. J. Stuchlík, "Advanced modeling for optical characterization of amorphous hydrogenated silicon films," *Thin Solid Films,* vol. 541, nº 31, pp. 12-16, 2013.

[48] E. Velazquez, "Github," Github, 15 07 2025. [Online]. Available: https://github.com/evelazq3z/Materials_Propieties_c-Si_a-Si-H.

[49] G. Cocorullo, F. D. Corte, I. Rendina e P. Sarro, "Thermo-optic effect exploitation in silicon microstructures," *Sensors and Actuators A: Physical,* vol. 71, nº 1-2, pp. 19-26, 1998.

[50] C. H. Forsberg, Heat Transfer Principles and Applications, C. H. Forsberg, Ed., Elsevier, 2020.

[51] M. A. Tauseef, R. A. Sabet e O. Tokel, "Laser Lithography of Monolithically-Integrated Multi-Level Microchannels in Silicon," *Advanced Materials Technologies,* vol. 9, nº 9, 2024.

[52] X. Wang, "Lithography simulation for the fabrication of silicon photonic devices with deep-ultraviolet lithography," em *San Diego, CA, USA*, The 9th International Conference on Group IV Photonics (GFP).

[53] P. M. Mendes, S. Jacke, K. Critchley, J. Plaza, Y. Chen, K. Nikitin, R. E. Palmer, J. A. Preece, S. D. Evans e D. Fitzmaurice, "Gold Nanoparticle Patterning of Silicon Wafers Using Chemical e-Beam Lithography," *American Chemical Society,* vol. 20, nº 9, pp. 3766-3768, 2004.

[54] J. Parra, J. N. Arenas e P. Sanchis., "Silicon thermo-optic phase shifters: a review of configurations and optimization strategies," *Advanced Photonics Nexus,* vol. 3, nº 4, 24 05 2024.

[55] A. Masood, M. Pantouvaki, G. Lepage, P. Verheyen, J. V. Campenhout e P. Absil, "Comparison of heater architectures for thermal control of silicon photonic circuits," em *10th International Conference on Group IV Photonics,*, Seoul, Korea (South), 2013, pp. 83-84.

[56] M. H. Seungjae Moon, M. Lee e C. P. Grigoropoulos, "Thermal conductivity of amorphous silicon thin films," *International Journal of Heat and Mass Transfer,* vol. 45, nº 12, pp. 2439-2447, 2002.

[57] G. W. Xingli Zhang, "Effect of Strain on Thermal Conductivity of Si Thin Films," *Journal of Nanomaterials,* vol. 2016, nº 1, 2016.

[58] K. Alaili, J. O. Miranda e Y. Ezzahri, "Effective interface thermal resistance and thermal conductivity of dielectric nanolayers," *International Journal of Thermal Sciences,* vol. Volume 131, pp. 40-47, 2018.

[59] J. M. Lugo, A. Oliva, H. Riveros e O. Ceh, "Heat capacity determination of metallic thin films using temperature profiles at room conditions: Theory,," em *2010 7th International Conference on Electrical Engineering Computing Science and Automatic Control,*, Tuxtla Gutierrez, Mexico, , 2010, pp. 504-509.

[60] M. Jacques, A. Samani, E. E. Fiky, D. Patel, Z. Xing e D. V. Plant, "Optimization of thermo-optic phase-shifter design and mitigation of thermal crosstalk on the SOI platform," *Optics Express,* vol. 27, nº 8, pp. 10456-10471, 15 04 2019.

[61] S. Liu, J. Feng, Y. Tian, H. Zhao, L. Jin, B. Ouyang, J. Zhu e J. Guo, "Thermo-optic phase shifters based on silicon-on-insulator platform: state-of-the-art and a review," *Frontiers of Optoelectronics,* vol. 15, nº 9, 2022.

[62] G. Cocorullo, F. D. C. *, L. Moretti, I. Rendina e A. Rubino, "Measurement of the thermo-optic coefficient of a-Si:H at the wavelength of 1500 nm from room temperature to 200 °C," *Journal of Non-Crystalline Solids ,* vol. 299, nº 302, pp. 310-313, 2002.

[63] E. Velazquez, "GitHub.com," GitHub, 10 08 2025. [Online]. Available: https://github.com/evelazq3z/TOE-TOPS_Resisitive_analysis/blob/main/thermal_phase_modulation.m.

[64] T. Intruments, "Materials Thermal Properties Database," Thermtest Intruments, [Online]. Available: https://thermtest.com/thermal-resources/materials-database. [Acedido em 09 06 2025].

[65] G. Elert e JennelleBaptiste, "The Physics Factbook: An encyclopedia of scientific essays," [Online]. Available: https://hypertextbook.com/facts/#foreheadless. [Acedido em 09 06 2025].

[66] S. M. R. Safaee, K. R. Mojaver, G. Zhang e O. Liboiron-Ladouceur, "Silicon Photonics Mode-Selective Phase Shifter,," *Journal of Lightwave Technology,* vol. 42, nº 7, pp. 2412-2421, 2024.

[67] E. E. Krause e D. Malka, "Optimizations of Double Titanium Nitride Thermo-Optic Phase-Shifter Heaters Using SOI Technology," *Sensors,* vol. 23, nº 20, p. 8587, 2023.

[68] R. Alemany, P. Muñoz, D. Pastor e C. Domínguez, "Thermo-Optic Phase Tuners Analysis and Design for Process Modules on a Silicon Nitride Platform," *Photonics,,* vol. 8, nº 11, p. 496, 2021.

[69] M. Alam, R. Pulavarthy e J. Bielefeld, "Thermal Conductivity Measurement of Low-k Dielectric Films: Effect of Porosity and Density," *J. Electron. Mater,* vol. 43, pp. 746-754, 2014.

[70] Q. Wang, M. Xie, Y. He, R. Xue, J. Guo e W. Fu, "Research Progress and Applications of Benzocyclobutene-Based Functional Polymers," *Macro-Molecular,* vol. 226, nº 1, 2025.

[71] R. Norwood, C. Derose, C. Greenlee e A. Yeniay, "25 - Organic waveguides, ultra-low loss demultiplexers and electro-optic (EO) polymer devices," em *Handbook of Organic Materials for Optical and (Opto)electronic Devices*, O. Ostroverkhova, Ed., Woodhead Publishing Series, 2010, pp. 709-785.

[72] R. W. Boyd, Nonlinear optics, 4rd Edition ed., Rochester, New York: Academic Press, 2020, p. 640.

[73] G. Sinatkas, T. Christopoulos, O. Tsilipakos e E. E. Kriezis, "Electro-optic modulation in integrated photonics," *Journal of Applied Physics,* vol. 130, nº 1, 2021.

[74] T. Lian, S. S. Kaidi Yang, M. Zhu, J. Yue, B. Lin, X. Sun, X. Wang e D. Zhang, "Polarization-independent electro-absorption optical modulator based on trapezoid polymer-graphene waveguide," *Optics & Laser Technology,* vol. 149, p. 107815, 2022.

[75] S. Gören, Y. Şale e M. Y. Seyidov, "The Franz–Keldysh effect in the optical absorption spectrum of a TlGaSe2 layered semiconductor caused by charged native defects," *Semiconductor Science and Technology,* vol. 39, nº 3, 15 02 2024.

[76] Y. T. a. I. Shalish, "Department of Electrical and Computer Engineering, Ben Gurion University of the Negev, Beer Sheva, Israel," *Franz-Keldysh effect in semiconductor built-in fields,* 22 04 2018.

[77] D. Miller, D. Chemla, T. Damen, A. Gossard, W. Wiegmann, T. Wood e C. Burrus, "Band-Edge Electroabsorption in Quantum Well Structures: The Quantum-Confined Stark Effect," *Physical Review Letters,* vol. 53, nº 22, pp. 2173-2176, 1984.

[78] I. P. Kaminow e T. u. E.H, "Linear Electrooptical Material," em *An Introduction to Electrooptic Devices: Selected Reprints and Introductory*, Cambridge, MA, USA, Academic Press, 2013, p. 110–120.

[79] Y. Li, M. Sun, T. Miao e J. Chen, "Towards High-Performance Pockels Effect-Based Modulators:Review and Projections," *Micromachines,* vol. 15, nº 7, 2024.

[80] VanTilburg e E. James, "Piezo-Electric Ringing in Deuterated Potassium Dihydrogen Phosphate Electrooptic Crystals," Partha Banerjee (Advisor), 2022.

[81] P. Ney, A. Maillard, M. D. Fontana e K. Polgár, "Accurate interferometric method for the measurement of electro-optic coefficients: application to a single β-barium borate crystal," *Optica Publishing Group,* vol. 17, nº 7, pp. 1158-1168, 2000.

[82] D. R. Paschotta, "RP Photonics Encyclopedia," Bannhaldenstrasse.

[83] S. Lakshan e S. Mukhopadhyay, "All-optical method for measuring the electrical parameters of passive electronic elements with active use of Pockels cells," *Journal of Optics,* vol. 52, pp. 944-948, 2022.

[84] S. Vujević, "A New Look to the Maxwell's Equations and Wave Equations in Conducting Media," em *International Conference on Software, Telecommunications and Computer Networks (SoftCOM)*, Split, Croatia, 2024.

[85] R. Ramaswami, K. Sivarajan e G. Sasaki, Optical Networks: A Practical Perspective, 3rd Edition ed., Morgan Kaufmann, 2009.

[86] F. Kärtner, Fundamentals of Photonics: Quantum Electronics: Lecture Notes, Cambridge, MA,USA: Massachusetts Institute of Technology (MIT), 2006.

[87] O. (. Ostroverkhova, Handbook of organic materials for optical and (opto) electronic devices: properties and applications., Oregon State University, USA: Elsevier, 2013.

[88] J. Yao e Y. Wang, Nonlinear Optics and Solid-State Lasers, Springer Science & Business Media, 2012.

[89] A. Karvounis, F. Timpu, Viola V. Vogler-Neuling, R. Savo e R. Grange, "Barium titanate nanostructures and thin films for photonics.," *Advanced Optical Materials,* vol. 8, nº 4, 2020.

[90] M. Tao, B. Zhang, T. Zhao, X. Wu, M. Liu, G. Dong e J. Wang, “Towards high quality transferred barium titanate ferroelectric hybrid integrated modulator on silicon,” *Light: Advanced Manufacturing,* vol. 5, nº 4, pp. 479-489, 2025.

[91] J. L. Casson, K. T. Gahagan, D. A. Scrymgeour, R. K. Jain, J. M. Robinson, V. Gopalan e R. K. Sander, “Electro-optic coefficients of lithium tantalate at near-infrared wavelengths,” *Journal of the Optical Society of America B,* vol. 21, nº 11, pp. 1948-1952, 2004.

[92] M. Reynaud, M. Waqar e C. Du, “Enhancement of electro-optic response in BaTiO3 films integrated on Si via heating and cooling rate control,” *Commun Mater,* vol. 6, nº 176, 2025.

[93] B. Tilmann, T. Huq, T. Possmayer, J. Dranczewski, B. Nickel, H. Zhang, L. Krivitsky, A. I. Kuznetsov, L. d. S. Menezes, S. Vezzoli, R. Sapienza e S. A. Maier, “Comparison of Harmonic Generation from Crystalline and Amorphous Gallium Phosphide Nanofilms,” *Advanced Optical Material,* vol. 11, nº 16, 2023.

[94] Y. Avrahami, $BaTiO_3$ based materials for piezoelectric and electro-optic applications (Doctoral dissertation), Massachusetts Institute of Technology: Massachusetts Institute of Technology., 2003.

[95] P. Xie e T. Mishima, “Fast switching of light propagation in a photorefractive crystal via Pockels effect,” *Optics Communications,* vol. 246, nº 3, pp. 29-34, 2005.

[96] E. FREYSZ e J. DEGERT, “Terahertz Kerr effect,” *Nature photonics,* vol. 4, nº 3, pp. 131-132, 2010.

[97] D. R. Paschotta, “Kerr Effect,” RP Photonics Encyclopedia, 2016.

[98] A. Cherouana, A. Bencheikh e I. Bouchama, “Effect of the electric field induced birefringence on the slab waveguide evanescent-wave sensor sensitivity,” *Optical and Quantum Electronics,* vol. 51, nº 331, 2019.

[99] S. J. Ling, J. Sanny e W. Moebs, University Physics, vol. 2, Houston, Texas 77005: OpenStax, 2021.

[100] S. O.Kasap, “Electro-Optic Effect,” em *Optoelectronics and Photonics Principles and Practices*, Pearson, 2013, pp. 478-486.

[101] G. New, Introduction to nonlinear optics, Cambridge: Cambridge University Press., 2011.

[102] C. Li, Nonlinear Optics Principles and Applications, Harbin, China: Springer, 2017.

[103] R. W. Boyd e G. L. Fischer, “NonLinear Optical Materials,” em *Encyclopedia of materials: science and technology*, Elsevier, 2004, pp. 6237-6244.

[104] A. e. a. Maldonado, “Electro-optical Kerr constant measurement of tellurite and chalcogenide,” *Optical Materials,* vol. 143, nº 114504, 2023.

[105] B. Derkowska, F. Firszt e B. Sahraoui and A. Marasek, “Experimental Results of Third Order Nonlinear Optical Susceptibility of Oriented and Annealed ZnSe Crystals,” em *3rd ICTON Mediterranean Winter Conference (ICTON-MW)*, Angers, France, 2009.

[106] M. Yamane e Y. Asahara., Glasses for Photonics, 2nd ed., Cambridge, United Kingdom: Cambridge University Press,, 2004.

[107] E. Velazquez, “GitHub,” 18 08 2025. [Online]. Available: https://github.com/evelazq3z/Kerr-Effect.

[108] G. Agrawal, Nonlinear Fiber Optics, Academic Press, 2013.

[109] J. M. Dziedzic, R. H. Stolen e A. Ashkin., “Optical Kerr effect in long fibers,” em *Applied optics*, 1981, pp. 1403-1406.

[110] A. F. A. Noorden, S. Daud e J. Ali, “AIP Conference Proceedings,” *Implication of Plasma Dispersion Effect for Controlling Refractive Index in Microresonator,* vol. 1824, nº 1, 3 2017.

[111] Y. Zhu, Z. Huang, J. Su e B. Tang, “Actively tunable and switchable terahertz metamaterials with multi-band perfect absorption and polarization conversion,” *Physical Chemistry Chemical Physics,* vol. 26, nº 15, pp. 11649 - 11656, 2024.

[112] M. Eldlio, F. Che e a. M. Cad, “Chapter 4: Drude-Lorentz Model of Semiconductor Optical Plasmons,” em *IAENG Transactions on Engineering Technologies. Lecture Notes in*

Electrical Engineering, Netherlands, Springer Science and Business Media Dordrecht, 2014, pp. 41-49.

[113] Y. Kim, M. Takenaka, T. Osada, M. Hata e S. Takagi, "Nature Scientific Reports," *Strain-induced enhancement of plasma ispersion effect and free-carrier absorption in SiGe optical modulators,* 15 04 2014.

[114] F. C. Ndi, J. Toulouse, T. Hodson e D. W. Prathe, "All-optical switching in silicon photonic crystal waveguides by use of the plasma dispersion effect," *Optics Letters,* vol. 30, nº 17, 2005.

[115] Y. Kim, J.-H. Han, D. Ahn e S. Kim, "Heterogeneously-Integrated Optical Phase Shifters for Next-Generation Modulators and Switches on a Silicon Photonics Platform: A Review," *Micromachines,* vol. 12, nº 625, 2021.

[116] R. A. Soref e B. R. Bennett, "Electrooptical effects in silicon," *IEEE J. Quantum Electron,* vol. 23, nº 1, pp. 123-129, 1987.

[117] G. T. Reed, Silicon Photonics: The State of the Art, Surrey, UK: John Wiley & Sons, 2008.

[118] G. T. Reed, G. Mashanovich, F. Y. Gardes e D. J. Thomson, "Silicon optical modulators," *Nature Photonics,* vol. 4, pp. 518-526, 2010.

[119] D. V. Lucarini, J. J. Saarinen, K.-E. Peiponen e E. M. Vartiainen, Kramers–Kronig Relations in Optical Materials Research, A. T. Rhodes, Ed., Berlin: Springer, 2005, p. 173.

[120] Y. B. Gianchandani, O. Tabata e H. Zappe, Comprehensive Microsystems, vol. 1, Elsevier Science, 2008.

[121] A. AOUICHE, Semiconductor Physics, 2024.

[122] S. M. Sze e M.-K. Lee, Semiconductor Devices Physics and Technology, John Wiley & Sons Singapore Pte. Limited, 2012.

[123] S. M. SZE, Y. LI e K. K. NG, Physics of semiconductor devices, John wiley & sons, 2021.

[124] S. Hlali, N. Hizem e A. Kalboussi, "High-k dielectric materials for the gate oxide of a MIS capacitor: effect of interface states on the C–V characteristics," *Journal of computational electronics,* vol. 15, pp. 1340-1350, 2016.

[125] A. Rahim, A. Hermans, B. Wohlfeil, B. K. Despoina Petousi, D. V. Thourhout e R. G. Baets, "Taking silicon photonics modulators to a higher performance level: state-of-the-art and a review of new technologies," *Advances Photonics,* vol. 3, nº 2, 2021.

[126] B. Z. a. A. X. W. W. -C. Hsu, "MOS Capacitor-Driven Silicon Modulators: A Mini Review and Comparative Analysis of Modulation Efficiency and Optical Loss," *IEEE Journal of Selected Topics in Quantum Electronics,* vol. 28, nº 3, pp. 1-11, 2022.

[127] "High Bandwidth Capacitance Efficient Silicon MOS Modulator," *Journal of Lightwave Technology,* vol. 39, nº 1, pp. 201-207, Weiwei Zhang; Kapil Debnath; Bigeng Chen; Ke Li; Shenghao Liu; Martin Ebert; Jamie Dean Reynolds; Ali Z. Khokhar; Callum Littlejohns; James Byers; Muhammad K. Husain; Frederic Y. Gardes; Shinichi Saito; David J. Thomson.

[128] S. Xu e Hongyi Wang, "A new multitime programmable non-volatile memory cell using high voltage NMOS," *Microelectronics Reliability,* vol. 88, nº 90, pp. 169-172, 2018.

[129] "Design and optimization of multiple-time programmable memory cell by advanced CMOS FinFET technologies," *Japanese Journal of Applied Physics,* vol. 60, nº SB, 2021.

[130] P. P. Fastykovsky, "Influence of air humidity on the low-frequency capacitance of silicon MOS," *Sensors and Actuators B: Chemical,* vol. 304, nº 1, p. 127318, 2020.

[131] W.-J. Ho, J.-J. Liao, Z.-F. Hou, C.-W. Yeh e R.-S. Sue, "High efficiency textured silicon solar cells based on an ITO/TiO2/Si MOS structure and biasing effects,," *Computational Materials Science,* vol. 117, pp. 596-601, 2016.

[132] D. Kumar, A. Rezk, A. Nayfeh e N. El-Atab, "MoS2-Based MOS Capacitor for In-Memory Light Sensing," *ECS Transactions,,* vol. 111, nº 1, 2023.

[133] X. Qiu, Y. L. Xiaoke Ruan e A. F. Zhang, "Multi-layer MOS capacitor based polarization insensitive electro-optic intensity modulator," *Optics Express,* vol. 26, nº 11, pp. 13902-13914, 2018.

[134] M. Levi, A. Chelly e A. Karsenty, "A comprehensive review of nanoscale MOS capacitors applications in photonics," *Reviews in Physics,* vol. 13, nº 1, pp. 100-1006, 2025.

[135] L. Hutin, B. Bertrand, H. Niebojewski, P.-A. Mortemousque, M. Cassé e G. Billiot, "MOS technology for quantum computing: recent progress and perspectives for scaling up," em *Device Research Conference (DRC)*, Santa Barbara, CA, USA, 2021.

[136] D. M. Dourado, G. B. d. F. R. H. Gounella, M. d. L. Rocha e J. Carmo, "Challenges in silicon photonics modulators for data center interconnect applications," *Optics and Laser Technology,* vol. 144, pp. 1073-1076, 2021.

[137] I. Taghavi, M. Moridsadat, A. Tofini, S. Raza e N. A. F. Jaeger., "Polymer modulators in silicon photonics: review and projections," *Nanophotonics,* vol. 11, nº 17, p. 3855–3870, 2022.

[138] S. Akiyama e T. Usuki, "High-speed and efficient silicon modulator based on forward-biased pin diodes," *Frontiers in Physics,* vol. 2, nº 65, 2014.

[139] K. Debnath, D. J. Thomson, W. Zhang, A. Z. Khokhar, C. Littlejohns, J. Byers, L. Mastronardi, M. K. Husain, K. Ibukuro, F. Y. Gardes, G. T. Reed e a. S. Saito, "All-silicon carrier accumulation modulator based on a lateral metal-oxide-semiconductor capacitor," *Photonics Research,* vol. 6, nº 5, pp. 373-379, 2018.

[140] Z.-Y. Li, D.-X. Xu, W. R. McKinnon, S. Janz, J. H. Schmid, P. Cheben e J.-Z. Yu, "Silicon waveguide modulator based on carrier depletion in periodically interleaved PN junctions," *Optics express,* vol. 17, nº 18, pp. 15947-15958, 2019.

[141] M. Lipson, "Compact Electro-Optic Modulators on a Silicon Chip," *IEEE Journal of Selected Topics in Quantum Electronics,* vol. 12, nº 6, pp. 1520-1526, 2006.

[142] S. J. Spector, M. W. Geis, M. E. Grein, R. T. Schulein1, J. U. Yoon, D. M. Lennon, F. Gan, G. Zhou, F. X. Kaertner e T. M. Lyszczarz, "High-speed silicon electro-optical modulator that can be operated in carrier depletion or carrier injection mode," em *Conference on Lasers and Electro-Optics and 2008 Conference on Quantum Electronics and Laser Science,* , San Jose, CA, USA, 2088.

[143] Y. Huang, J. Zheng, B. Pan, L. Song, K.-A. Chen, Z. Yu, H. Ye e D. DaI, "High-bandwidth Si/In2O3 hybrid plasmonic waveguide modulator," *APL Photonics,* vol. 7, nº 5, 2022.

[144] Q. S. Xu e P. S. B., "Micrometre-scale silicon electro-optic modulator," *Nature,* vol. 435, pp. 325-327, 2005.

[145] L. Vivien, C. Baudot, F. Bouf e B. e. a. Szelag, "Building blocks of silicon photonics," *Semiconductors and Semimetals,* vol. 101, nº 1, pp. 1-41, 2019.

[146] G. T. Reed, D. J. Thomson, F. Y. Gardes, Y. Hu, J.-M. Fedeli e G. Z. Mashanovich, "High-speed carrier-depletion silicon Mach-Zehnder optical modulators with lateral PN junctions," *Frontiers in Physics,* vol. 2, 2014.

[147] G. Reed, G. Mashanovich, F. Gardes, M. Nedeljkovic, Y. Hu, D. Thomson, K. Li, P. Wilson, S.-W. Chen e S. Hsu, "Recent breakthroughs in carrier depletion based silicon optical modulators," *Nanophotonics,* vol. 3, pp. 229-245, 2014.

[148] W. B. H. Yu e A. D. Keersgieter, "Optimization of Ion Implantation Condition for Depletion-Type Silicon Optical Modulators," *IEEE Journal of Quantum Electronics,,* vol. 46, nº 12, pp. 1763-1768, 2010.

[149] W. Zhang, M. Ebert, B. Chen, J. D. Reynolds, X. Yan, H. Du, M. Banakar, D. T. Tran, K. Debnath, C. G. Littlejohns, S. Saito e a. D. J. Thomson, "Integration of low loss vertical slot waveguides on SOI photonic platforms for high efficiency carrier accumulation modulators," *Optics Express,* vol. 28, nº 16, pp. 23143-23153, 2020.

[150] M. Webster, P. Gothoskar, V. Patel, D. Piede, S. Anderson, R. Tummidi, D. Adams, C. Appel, P. Metz, S. Sunder, B. Dama e a. K. Shastri, "An Efficient MOS-Capacitor based Silicon

Modulator and CMOS Drivers for Optical Transmitters," em *IEEE 11th International Conference on Group IV Photonics (GFP)*, Paris, France, 27-29 August 2014.

[151] G. T. Reed, Silicon Photonics The State of the Art, Wiley, 2008.

[152] S. Samanta, P. Banerji e a. P. Ganguly., Photonic Waveguide Components on Silicon Substrate: Modeling and Experiments, Springer Nature, 2020.

[153] M. Roussey, L. Ahmadi, S. Pélisset, M. Häyrinen, A. Bera, V. Kontturi, J. Laukkanen, I. Vartiainen, S. Honkanen e a. M. Kuittinen, "Strip-loaded horizontal slot waveguide," *Optics Letters,* vol. 42, nº 2, pp. 211-214, 2017.

[154] K. Y. You, "Review on Optical Waveguides," em *Emerging Waveguide Technology*, Malasia, 2018, p. Chapter 6.

[155] Y. Zou, S. Chakravarty, C. Chung, J. X. X e R. T. Chen, "Mid-infrared silicon photonic waveguides with suspended structures," *Photonics Research,* vol. 6, nº 4, pp. 254-276, 2018.

[156] K. Okamoto, "2.2 RECTANGULAR WAVEGUIDES," em *Fundamentals of optical waveguides*, Japan, Elsevier, 2021, pp. 27-31.

[157] M. Polyanskiy, "https://refractiveindex.info/," 18 01 2024. [Online]. Available: https://refractiveindex.info/. [Acedido em 09 06 2025].

[158] E. Velazquez, "Github," Github, 06 06 2025. [Online]. Available: https://github.com/evelazq3z/Marcatili.

[159] W.-P. Huang, "Coupled-mode theory for optical waveguides: an overview," *Journal of the Optical Society of America,* vol. 11, nº 3, pp. 963-983, 1994.

[160] H. Chang, H. S. Huang e a. Y. Wang., "On the various forms of the coupled-mode theory for optical waveguides," *Microwave and Optical Technology Letters,* vol. 3, nº 8, pp. 296-298, 1990.

[161] M. Kuznetsov, "Expressions for the coupling coefficient of a rectangular-waveguide directional coupler," *Optics letters,* vol. 8, nº 9, pp. 499-501, 1983.

[162] M. Hamidah e a. R. W. Purnamaningsih, "An S-bend based optical directional coupler using GaN semiconductor," em *IEEE International Conference on Innovative Research and Development (ICIRD).*, Jakarta, Indonesia, 2019.

[163] H. Sattari, A. Y. Takabayashi, Y. Zhang, P. Verheyen, W. Bogaerts e N. Quack, "Compact broadband suspended silicon photonic directional coupler," *Optics Letters,* vol. 45, nº 11, pp. 2997-3000, 2020.

[164] R. G. Hunsperger, "Chapter 8: Coupling Between Waveguides," em *Integrated Optics: Theory and Technology*, Verlag New York, Springer, 2009, pp. 153-168.

[165] E. Velazquez, "Github," Github, 15 07 2025. [Online]. Available: https://github.com/evelazq3z/CMT_Coupler.

[166] MathWorks, "MathWorks.com," MathWorks, 20 05 2025. [Online]. Available: https://la.mathworks.com. [Acedido em 27 08 2025].

[167] P. w. site, "Python.org," Python, [Online]. Available: https://www.python.org/. [Acedido em 20 05 2025].

[168] J. B. Schneider, "Introduction to the Finite-Difference Time-Domain Method: FDTD in 1D," em *Understanding the Finite-Difference Time-Domain Method*, Washington, School of electrical engineering and computer science Washington State University , 2025, pp. 29-64.

[169] "www.synopsys.com," Synopsys, 2025. [Online]. Available: https://www.synopsys.com/glossary/what-is-fdtd.html. [Acedido em 04 06 2025].

[170] F. L. Teixeira, C. Sarris, Y. Zhang, J.-P. Berenger, M. Okoniewski, W. C. Chew e J. J. .. Simpson, "Finite-difference time-domain methods," *Nature Reviews Methods Primers,* vol. 75, nº 3, 2024.

[171] M. M., "The beam propagation method," em *Classical Optics and Its Applications*, Cambridge University Press, 2009, pp. 459-475.

[172] N. P. S. o. E. B. N. U. Kurt H. Becker, Ed., "Chapter 3 Dielectric Slab Waveguide," em *Principles of Photonic Integrated Circuits*, Springer, 2021, pp. 31-56.

[173] G. Brunetti, R. Heuvink, E. Schreuder e M. N. A. a. C. Ciminelli, "Silicon Nitride Spot Size Converter With Very Low-Loss Over the C-Band," *IEEE Photonics Technology Letters,* vol. 35, nº 22, pp. 1215-1218, Nov.15, 2023.

[174] Y. Maegami, R. Takei, E. Omoda, T. Amano, M. Okano, M. Mori, T. Kamei e Y. Sakakibara, "Spot-size converter with a SiO2 spacer layer between tapered Si and SiON waveguides for fiber-to-chip coupling," *Optics Express,* vol. 23, nº 16, pp. 21287-21295, 2015.

[175] E. Velazquez, "GitHub," GitHub, 29 07 2025. [Online]. Available: https://github.com/evelazq3z/Calculation_doping_concentration.

[176] P. M. Seiler, K. Voig, A. P. G. Georgieva, S. Lischke, A. Malignaggi e a. L. Zimmermann, "Multiband Silicon Photonic ePIC Coherent Receiver for 64 GBd QPSK," *Journal of Lightwave Technology,* vol. 40, nº 10, pp. 3331-3337, 2022.

[177] D. Nikolova, S. Rumley, D. Calhoun, Q. Li, R. Hendry e a. K. B. Payman Samadi, "Scaling silicon photonic switch fabrics for data center interconnection networks," *Optics express,,* vol. 23, nº 2, pp. 1159-1175, 2015.

[178] X. Shen, B. Chen, Y. Zhu e W. & Shi, "Silicon photonic integrated circuits and its application in data center," em *Seventh Symposium on Novel Photoelectronic Detection Technology and Applications*, 2021.

[179] J. o. O. C. a. Networking, "Optical switching will innovate intra data center networks," *Journal of Optical Communications and Networking,* vol. 16, nº 1, pp. A1-A23, 2024.

[180] J. Feldmann, N. Youngblood, M. Karpov, H. Gehring, X. Li, M. Stappers, M. L. Gallo, X. Fu e A. Lukashchuk, "Parallel convolutional processing using an integrated photonic tensor core," *Nature,* vol. 589, pp. 52-58, 2021.

[181] R. Janeiro, R. Flores e J. Viegas, "Silicon photonics waveguide array sensor for selective detection of VOCs at room temperature," *Scientific Reports,* vol. 9, nº 1, pp. 2045-2322, 2019.